Quantum size effects and carrier dynamics in two-dimensional lead halide perovskite nanostructures

Dissertation

an der Fakultät für Physik der
Ludwig-Maximilians-Universität München

vorgelegt von

Jasmina Angelika Sichert
aus Regensburg

München, 27. Februar 2019

Erstgutachter:	Prof. Dr. Jochen Feldmann
Zweitgutachter:	PD Dr. Bert Nickel

Tag der mündlichen Prüfung: 16. Mai 2019

Kurzfassung

In den letzten Jahren zeigten Bleihalogenid-Perowskite nicht nur vielversprechende Einsatzmöglichkeiten in Solarzellen, sondern ebenso großes Potenzial für lichtemittierende Bauteile und andere optoelektronische Anwendungen. Die meisten der ersten Studien konzentrierten sich auf Perowskit-Volumenkristalle. Jedoch zeigt sich, dass die aufkommenden kolloidalen Perowskit-Nanokristalle überlegene Eigenschaften hinsichtlich Effizienz und Funktionalität aufweisen. Im Bereich der Nanoskalen können größenabhängige Effekte genutzt werden, um die Eigenschaften der Nanokristalle zu beeinflussen. In der vorliegenden Arbeit werden zweidimensionale Perowskit-Nanoplättchen und quasi-zweidimensionale hybride Perowskit-Schichtstrukturen erforscht.

Eine neue, systematische Variation der Ligandenkonzentration während der Nanokristall-Synthese wird vorgestellt. Sie ermöglicht, kolloidale zweidimensionale Methylammonium-Bleibromid-Perowskit-Nanoplättchen unterschiedlicher Dicke bis hin zu nur einer einzigen Einheitszelle herzustellen. Photolumineszenz- und Absorptionsspektren zeigen bei den dünnsten Strukturen klare exzitonische Merkmale und eine Blauverschiebung der Emissionswellenlänge von mehr als 90 nm im Vergleich zu entsprechenden Volumenkristallen. Des Weiteren erhöht sich die Exzitonenbindungsenergie in den dünnsten Strukturen auf mehrere hundert meV aufgrund reduzierter Exzitonenabschirmung. Erstmals wird der Größenquantisierungseffekt in diesen Nanoplättchen mit Hilfe von Modellrechnungen quantitativ beschrieben. Die Entstehung von Minibändern in den Multischichtstrukturen senkt die Emissionsenergie im Vergleich zu isolierten Nanoplättchen.

Es werden dickeabhängige Photolumineszenz-Lebenszeitmessungen ausgeführt. Die gemessenen Lebenszeiten verkürzen sich für dünnere Strukturen aufgrund höherer Exzitonenbindungsenergien. Temperaturabhängige Photolumineszenzmessungen an Cäsium-Bleibromid-Perowskit-Nanoplättchen werden durchgeführt. Ein theoretisches Modell, das die akustischen und optischen Phononen als Hauptursache der Exzitonenstreuung berücksichtigt, zeigt, dass erstere bei Temperaturen unter 90 K dominieren und letztere bei höheren Temperaturen. Interessanterweise zeigen temperaturabhängige zeitaufgelöste Photolumineszenzmessungen, dass unter 60 K leuchtende und dunkle Zustände zu den Zerfallskurven beitragen. Bei höheren Temperaturen wird keine Unterdrückung der Lumineszenz beobachtet, was darauf hindeutet, dass die Liganden in diesen Strukturen mit großem Oberfläche-zu-Volumen-Verhältnis eine wichtige Rolle spielen.

Die Distanz zwischen den Schichten in hybriden Perowskit-Schichtstrukturen wird systematisch variiert, um den Einfluss auf Struktur-Funktions-Beziehungen und Kopplungen zwischen den Perowskitschichten zu untersuchen. Es zeigt sich, dass die optische Bandlücke im Wesentlichen von zwei Effekten bestimmt wird. Erstens ändert sich mit der Länge der organischen Liganden, welche die anorganischen Perowskitschichten voneinander trennen, der Verkippungswinkel der Oktaeder. Die optische Bandlücke wird größer mit größerem Verkippungswinkel. Zweitens beeinflusst die Kopplung zwischen den Lagen der Perowskit-Schichtstrukturen die Bandlücke, wenn auch weniger signifikant als die Änderung der Verkippungswinkel. Wesentlich ist, dass die Kopplung nur für Multilagen mit einem Schichtabstand unter 1.5 nm eintritt.

Die vorliegende Arbeit trägt zu einem grundlegenden Verständnis der optischen Eigenschaften zweidimensionaler Perowskite bei. Der Fokus liegt auf dickeabhängigen Größenquantisierungseffekten, Exziton-Phonon-Wechselwirkungen und Struktur-Funktions-Beziehungen.

Abstract

In recent years, lead halide perovskites have not only proven to be a promising material for solar cell applications, but they have also shown a huge potential for light-emitting devices and other optoelectronic applications. Most of the initial studies focused on bulk perovskite materials. However, emerging colloidal perovskite nanocrystals have been shown to exhibit superior qualities relating to their efficiency and functionality. On the nanoscale, size-dependent effects can be exploited to tune the nanocrystals' properties. In the present work, two-dimensional perovskite nanoplatelets and quasi-two-dimensional layered hybrid perovskites are investigated.

A new and systematic variation of the ligand concentration during the nanocrystal synthesis is presented. This enables the fabrication of colloidal two-dimensional methylammonium lead bromide perovskite nanoplatelets of varying thicknesses down to only a single unit cell. Photoluminescence and absorption spectra show the appearance of clear excitonic features in the thinnest structures and a blue-shift in the emission wavelength of more than 90 nm in comparison to the bulk counterpart. Additionally, in the thinnest structures the exciton binding energy increases up to several hundreds of meV due to a reduced excitonic screening. For the first time the quantum size effect in these nanoplatelets is quantitatively described through model calculations. Miniband formation in the multilayer structures lowers the emission energy with respect to the isolated nanoplatelet.

Thickness-dependent photoluminescence lifetime measurements are performed. The recorded lifetimes decrease with thinner nanoplatelets as the exciton binding energy increases. Temperature-dependent photoluminescence measurements on cesium lead bromide perovskite nanoplatelets are carried out. A theoretical model considering acoustic and optical phonons as the main sources for scattering of excitons, shows that the former dominate at temperatures below 90 K and the latter above this temperature. Interestingly, temperature-dependent time-resolved photoluminescence measurements display contributions of bright and dark excitons to the decay curves below 60 K. At higher temperatures an antiquenching behavior of the luminescence is observed, indicating that ligands play an important role in these structures with a high surface-to-volume ratio.

The interlayer distance in layered hybrid perovskites is systematically varied to investigate its impact on structure-function relationships and electronic coupling between the perovskite layers. It is found that the optical bandgap is determined mainly by two parameters. First, the length of the organic ligands separating the inorganic perovskite sheets influences the tilt angle of the perovskite octahedra. An increase of the optical bandgap with larger tilt angles is observed. Secondly, electronic coupling between the perovskite sheets constituting the multilayer structures is found to have an impact on the bandgap, albeit significantly smaller than the effect induced by the change in tilt angles. Importantly, the electronic coupling only occurs for perovskite multilayers with an interlayer distance below 1.5 nm.

This thesis contributes to a fundamental understanding of optical properties of two-dimensional perovskites. It focuses on thickness-dependent quantum size effects, exciton-phonon interactions, and structure-function relationships.

Publications

Scientific publications of results presented in this work

- J. A. Sichert, Y. Tong, N. Mutz, M. Vollmer, S. Fischer, K. Z. Milowska, R. García Cortadella, B. Nickel, C. Cardenas-Daw, J. K. Stolarczyk, A. S. Urban, J. Feldmann: *Quantum size effect in organometal halide perovskite nanoplatelets*, Nano Lett. **15**, 6521 (2015)
- J. A. Sichert, A. Hemmerling, C. Cardenas-Daw, A. S. Urban, J. Feldmann: *Tuning the optical bandgap in layered hybrid perovskites through variation of alkyl chain length*, APL Mater. **7**, 041116 (2019)

Additional publications

- V. A. Hintermayr, A. F. Richter, F. Ehrat, M. Döblinger, W. Vanderlinden, J. A. Sichert, Y. Tong, L. Polavarapu, J. Feldmann, A. S. Urban: *Tuning the optical properties of perovskite nanoplatelets through composition and thickness by ligand-assisted exfoliation*, Adv. Mater. **28**, 9478 (2016)
- H. Huang, L. Polavarapu, J. A. Sichert, A. S. Susha, A. S. Urban, A. L. Rogach: *Colloidal lead halide perovskite nanocrystals: synthesis, optical properties and applications*, NPG Asia Mater. **8**, 328 (2016)

Contributions to conferences and workshops

- J. A. Sichert, Y. Tong, N. Mutz, F. Ehrat, M. Fu, J. K. Stolarczyk, C. Cardenas-Daw, A. S. Urban, J. Feldmann
  The role of octylamine in determining the physical and optical properties of organo-lead halide perovskite nanocrystals
  4th International Solar Technologies Go Hybrid-Workshop, Kloster Banz, Germany, March 2015
- J. A. Sichert, Y. Tong, N. Mutz, M. Vollmer, S. Fischer, K. Z. Milowska, B. Nickel, J. K. Stolarczyk, C. Cardenas-Daw, A. S. Urban, J. Feldmann
  Tuning the optical properties of organo-metal halide perovskite nanocrystals by varying octylamine ligand ratio
  NIM Summer School, Lenggries, Germany, July 2015

- J. A. Sichert, Y. Tong, N. Mutz, M. Vollmer, S. Fischer, K. Z. Milowska, R. García Cortadella, B. Nickel, C. Cardenas-Daw, J. K. Stolarczyk, A. S. Urban, J. Feldmann
  Quantum size effect in organometal halide perovskite nanoplatelets
  MRS Fall Meeting, Boston, USA, November 2015
- J. A. Sichert, Y. Tong, N. Mutz, M. Vollmer, S. Fischer, K. Z. Milowska, R. García Cortadella, B. Nickel, C. Cardenas-Daw, J. K. Stolarczyk, A. S. Urban, J. Feldmann
  Quantum size effect in organic/inorganic halide perovskite nanoplatelets
  NIM Winter School, Kirchberg, Austria, March 2016
- J. A. Sichert, Y. Tong, N. Mutz, M. Vollmer, S. Fischer, K. Z. Milowska, R. García Cortadella, B. Nickel, C. Cardenas-Daw, J. K. Stolarczyk, A. S. Urban, J. Feldmann
  Quantum size effect in organic-inorganic halide perovskite nanoplatelets
  5th International SolTech Conference, München, Germany, April 2016
- J. A. Sichert
  Temperature-dependent lifetime studies on 2D perovskites
  Workshop on Photonics and Optoelectronics with New Materials, Lenggries, Germany, July 2016
- J. A. Sichert, Y. Tong, N. Mutz, M. Vollmer, S. Fischer, K. Z. Milowska, R. García Cortadella, B. Nickel, C. Cardenas-Daw, J. K. Stolarczyk, A. S. Urban, J. Feldmann
  Quantum size effect in organometal halide perovskite nanoplatelets
  CeNS Workshop: Nanoscale Matter - Novel Concepts and Functions, Venice, Italy, September 2016
- J. A. Sichert, Y. Tong, L. Polavarapu, C. Cardenas-Daw, A. S. Urban, J. Feldmann
  Optical properties of organic/inorganic and all-inorganic lead halide perovskite nanoplatelets
  Workshop on optical spectroscopy of new materials, Siracuse, Italy, March 2017
- J. A. Sichert, Y. Tong, L. Polavarapu, C. Cardenas-Daw, A. S. Urban, J. Feldmann
  Optical properties of organic/inorganic and all-inorganic lead halide perovskite nanoplatelets
  DPG Frühjahrstagung, Dresden, Germany, March 2017

Awards

- Best Poster Award at 4th International Solar Technologies Go Hybrid-Workshop 2015
- Best Poster Award Nominee at MRS Fall Meeting 2015
- CeNS Publication Award 2017, Category: Best junior scientist publication

Contents

Kurzfassung I

Abstract III

1. Introduction 1

2. Background 5

2.1. Fundamentals of 2D semiconductors . . . 6

2.1.1. From solids to 2D heterostructures and nanocrystals . . . 6

2.1.2. Quantum confinement in 2D semiconductors . . . 7

2.1.3. Superlattice and miniband formation . . . 9

2.1.4. Excitons . . . 10

2.1.5. Excitons in the high confinement regime . . . 11

2.2. Fundamentals of 3D perovskites . . . 14

2.2.1. Perovskite crystal structure . . . 14

2.2.2. Electronic band structure and temperature-dependent effects . . . 15

2.2.3. Charge carrier recombination dynamics . . . 22

2.3. Perovskites of lower dimensionality . . . 24

2.3.1. Layered hybrid perovskites . . . 24

2.3.2. Colloidal perovskite nanocrystals . . . 27

3. Methods and materials 31

3.1. Syntheses . . . 32

3.1.1. Colloidal $MAPbBr_3$ nanoplatelets of different thicknesses . . . 32

3.1.2. Synthesis of $CsPbBr_3$ nanoplatelets . . . 33

3.1.3. Layered hybrid perovskites with varying interlayer spacings . . . 33

3.2. Structural characterization . . . 35

3.2.1. X-ray diffraction . . . 35

3.2.2. Electron microscopes . . . 37

3.3. Optical characterization . . . 39

3.3.1. Absorption spectroscopy . . . 39

3.3.2. Photoluminescence spectroscopy . . . 39

3.3.3. Streak camera: time-resolved photoluminescence spectroscopy 40
3.3.4. Setup for temperature-dependent time-correlated single photon counting 41

4. Quantum size effects in perovskite nanoplatelets 43
4.1. Synthesis 44
4.2. The ligands' influence on size and shape of perovskite nanocrystals 45
4.3. Decomposition of nanoplatelets through electron beam exposure 50
4.4. Thickness-dependence of the quantum size effect 52
4.5. Screening effects and enhanced exciton binding energies 54
4.6. Chapter summary 56

5. Carrier recombination dynamics and exciton-phonon interactions 57
5.1. Thickness-dependent time-resolved photoluminescence spectroscopy 58
5.2. Exciton-phonon interactions and PL lifetimes in $CsPbBr_3$ nanoplatelets 62
5.3. Chapter summary 67

6. The influence of octahedral tilt and electronic coupling on the optical properties of layered hybrid perovskites 69
6.1. Interlayer spacing and formation of multiple quantum well structures 70
6.2. Ligand-mediated octahedral tilting and emission wavelength 71
6.3. Electronic coupling between multiple perovskite layers 75
6.4. Chapter summary 80

7. Conclusion and outlook 81

A. Appendix 85
A.1. Quantum yield of $MAPbBr_3$ nanoplatelets 85
A.2. XRD on $MAPbBr_3$: reflection multiplicity 86
A.3. EDX of degraded $MAPbBr_3$ nanoplatelets 87
A.4. Calculation of the exciton Bohr radii of $MAPbBr_3$ and $MAPbI_3$ 88
A.5. Kronig-Penney model calculations for $MAPbBr_3$ platelets 88
A.6. Quantum size effects in $MAPbI_3$ nanoplatelets 89
A.7. Thickness-dependent time-resolved PL spectroscopy of $MAPbI_3$ nanoplatelets . 91
A.8. Lifetimes in $CsPbBr_3$ nanoplatelets 92
A.9. Exciton-phonon interactions and PL lifetimes in $CsPbX_3$ nanocubes 92
A.10. Orthorhombic to monoclinic phase transition for $C_{12}PbI_4$ 96
A.11. Kronig-Penney and DFT for layered hybrid perovskites 97

Bibliography 99

Acknowledgments 115

1. Introduction

Metal halide perovskites constitute a class of semiconductors that has received drastically increasing attention from the research community in recent years. This has largely arisen out of the huge success and rapid progress of perovskites as absorber material in photovoltaic devices. The development of renewable energy technologies like solar energy conversion is elemental in keeping up with increasing global energy demand and crucial for climate stability.[1,2] Furthermore, perovskites are promising candidates for a diverse array of optoelectronic devices such as light-emitters. Light-emitting diodes (LED) are an energy-efficient alternative to light bulbs. Due to the large variety of possible applications of perovskites in key technologies, fundamental research on this material is essential to design highly efficient devices.

In recent years, the huge potential of perovskites for high-efficient optoelectronic devices has come to light. Although research on metal halide perovskites has been ongoing for more than a century and the discovery of a frequency-dependent photo-conductive response in metal halide perovskites dates back to 1958, the breakthrough of metal halide perovskites for optoelectronic applications came in two waves: the first one in the 1990s and the more prominent second one ever since 2009.[3,4]
In the 1990s, quasi-two-dimensional (2D) layered hybrid perovskites have been the subject of intense investigation. These materials constitute of inorganic metal halide perovskite sheets separated by organic layers. Mitzi and coworkers[5] implemented layered hybrid perovskites for the first time successfully into thin-film field-effect transistors. Furthermore, these perovskites were successfully implemented as active layers in LEDs.[6] As layered hybrid perovskites naturally self-assemble in molecular precise layered heterostructures, they are a convenient choice for thin-film applications. Additionally, the broad choice of components comprising the inorganic sheets as well as the organic spacer offers a rich variety of interesting material properties. Amongst the adjustable properties the polarization, luminescence, and conductivity of the organic layer play a significant role for optoelectronic applications. Especially the organic interlayers provide dielectric confinement effects that can drastically increase exciton binding energy, oscillator strength, and lifetime.[7,8]
The interest in metal halide perovskites seemed to subside for a while after the year 2000 until first reports of the utilization of bulk or three-dimensional (3D) organic-inorganic per-

ovskites as sensitizer material in dye-synthesized solar cells appeared in 2009. Perovskites replaced the common dye and the first devices reached power conversion efficiencies of 3.8 %.[9] When in 2012 the first non-sensitization type perovskite solar cell was demonstrated by Snaith et al.[10], its power conversion efficiency reached remarkable 10.9 %. Since then perovskite solar cells have undergone a considerable rise in efficiency. In the year 2014, when the work for this thesis started, already more than 15 % were achieved, and the current record in power conversion efficiency amounts to 23.3 % under laboratory conditions.[11] In comparison, the most common technology used for solar energy conversion are silicon solar cells that allow large scale production of modules with efficiencies of 15 %. In contrast to energy-intense fabrication of classical silicon solar cells, however, perovskite solar cells are low-cost solution processable. Still, there are some drawbacks to these materials. The major ones are their toxicity as well as their limited chemical and thermal stability. Some of the perovskites, including the ones investigated in this thesis, contain lead. Attempts to overcome these drawbacks are the replacement of the lead with less toxic elements like tin.[12,13] A promising way to address the stability issue is the incorporation of 2D nanoplatelets in optoelectronic devices.[14,15] Another successful approach to increase photoluminescence stability of perovskite nanocrystals in LEDs is their growth into mesoporous alumina.[16]

Together with the advances of perovskite solar cell technology, increasing effort was invested in understanding the origin of the exceptional performance of perovskite solar cells. Originally, the main focus laid on 3D perovskites and their application in solar devices. The most commonly used perovskite, methylammonium lead iodide ($MAPbI_3$), possesses excellent optical and electrical properties. A relatively small bandgap, high absorption coefficients, long charge carrier lifetimes, and ambipolar charge transport ensue the high efficiency of the photovoltaic devices.

With the success of the solar applications, layered hybrid perovskites have experienced a renaissance as well. Additionally, the field broadened and other members of the 3D perovskite family have been explored. The optical and electronic properties of perovskites are tunable by varying the composition of constituting halide ions. To a smaller degree also the crystal distortions, induced by cations or ligands, have an impact on the material properties. Thus, besides their application in solar cells, perovskites can be used for a whole variety of optoelectronic devices. In particular, halide perovskite LEDs have emerged as an important area of scientific research since the first report in 2014.[17] In the same year, the first synthesis of stable colloidal perovskite nanocrystals with bright fluorescence was reported.[18] The emergence of perovskite nanocrystals boosted the interest in metal halide perovskites. Compared to their bulk counterpart, size and dimensionality of nanocrystals offer additional parameters for tuning their optical properties. The tunability together with their efficient photoluminescence turns the material into an interesting system for

applications as well as for fundamental studies. For this new class of perovskite colloidal nanocrystals, there is still a lack of studies which correlate their optical properties with their geometry and quantitatively describe quantum size effects. This is one of the scientific questions that motivated my PhD study.

Throughout this thesis, I will present the research I have conducted on colloidal 2D perovskite nanoplatelets and layered hybrid perovskites. The aim of the study was to investigate size-dependent properties, carrier dynamics and structure-function relationships between ligand-induced distortion and the optical bandgap.

This thesis is structured in seven chapters. After this general introduction to the topic, the theoretical concepts necessary for understanding this thesis' experiments and their results are presented in chapter 2. A short introduction is provided into semiconductors of lower dimensionality, as well as into 3D metal halide perovskite semiconductors. Afterwards, the two types of lower-dimensional perovskites that are investigated in this thesis are presented, namely layered hybrid perovskites and the emerging colloidal perovskite nanocrystals. Chapter 3 demonstrates the experimental procedure applied: sample preparation, structural and optical measurement techniques. The main results of this work are presented in chapters 4 to 6. In chapter 4 the experimental results on the methylammonium lead bromide ($MAPbBr_3$) nanoplatelets are presented and discussed. The synthesis method that is established in this work is described. Subsequently, the syntheses products are analyzed with X-ray diffraction and electron microscopy revealing the shape of the synthesized crystals to be nanoplatelets. Thereafter, the quantum size effect that is found to emerge in perovskite nanoplatelets is discussed. Through model calculations the quantum size effect in this material is quantitatively analyzed for the first time. Chapter 5 provides a detailed investigation on the discovered thickness-dependent charge carrier recombination dynamics that arise in $MAPbBr_3$ nanoplatelets of different thickness. Moreover, exciton-phonon interactions are investigated in homogeneously dispersed cesium lead bromide ($CsPbBr_3$) nanoplatelets with a thickness of 3 layers of unit cells. Furthermore, temperature-dependent lifetimes are analyzed and discussed. In chapter 6 the experimental results of the layered hybrid perovskites based on alkylammonium lead iodide (C_lPbI_4) are presented. Their structure is analyzed in detail and related to the measured emission wavelengths. An additional energy correction is presented that relies on effective mass model calculations. The model calculations and their results, that agree well with the measured data, and limitations of the model are subsequently discussed in detail. The thesis ends with a brief conclusion and an outlook in chapter 7 on the contribution of my work to current research and possible future applications of perovskites in modern optoelectronic devices.

2. Background

In this chapter, the fundamental background necessary to understand this thesis is presented. The chapter is structured in three sections. First, the basics of low-dimensional semiconductors in general are presented. In particular, quantum confinement effects are discussed with respect to the density of states distribution, optical properties, electronic coupling, and excitons. Second, three-dimensional (3D) organic-inorganic and all-inorganic lead halide perovskites are briefly presented as a basis for later comparison with the results from lower-dimensional perovskites. The perovskite crystal structure, band structure, and density of states are briefly presented. Furthermore lattice distortions, exciton-phonon interactions, and charge carrier dynamics are discussed. Most of the cited literature was published during the work on this thesis, as perovskites have become a field of very intense research in recent years. In the third section, two types of two-dimensional (2D) perovskites are presented, namely layered hybrid perovskites and colloidal perovskite nanocrystals. Layered hybrid perovskites have been widely studied since their first successful application in transistors in the 1990s. An introduction is given to their crystal structure, their band structure in comparison to 3D perovskites, and the effects of lattice distortions on the optical bandgap. Finally, the concept of colloidal nanoplatelets is briefly explained. As this type of material was reported for the first time in 2014, just when the work for this thesis started, only a short introduction is given into this topic.

2.1. Fundamentals of 2D semiconductors

Organic-inorganic lead halide perovskites investigated in this thesis are a class of semiconductors. When the dimensionality of a semiconductor is reduced, the optical and electronic properties are altered in comparison to the bulk counterpart. An introduction to these size effects is given in the following.

2.1.1. From solids to 2D heterostructures and nanocrystals

Considering a bulk or 3D semiconductor, the size of the crystal is large in comparison to next-neighbor distances between the ions. Therefore, an infinite lattice approximation is used.[19] The wave functions are completely delocalized in real space and the band structure is a continuous dispersion of energy as a function of momentum. The assumption of an infinite lattice expansion holds no longer if the semiconductor is reduced to nanoscale in one or more dimensions.[20] Quantum size effects are observed if the carrier motion in a semiconductor is limited in one dimension to the order of the de Broglie wavelength λ_B or the mean free path, if this number is smaller.[19]
Figure 2.1 depicts the density of states (DOS) for electrons of a 3D, 2D, 1D, and 0D semiconductor nanostructure. Reducing the dimensions of a semiconductor from 3D to 2D results in a localization of the wave functions of electrons and holes. This leads to a step-function like density of states distribution and a larger bandgap. Further decrease in dimension will eventually lead to a discrete DOS distribution for the case of a 0D semiconductor. Originally, when the theory was developed in the 1930s, the restrictions of the theory to infinite bodies were regarded to be meaningless.[21] Small crystallites of a few µm in size are still large compared to next-neighbor distances. Yet the idea to study quantum size effects in ultrathin layers became popular in the late 1950s.[22] Thin films of

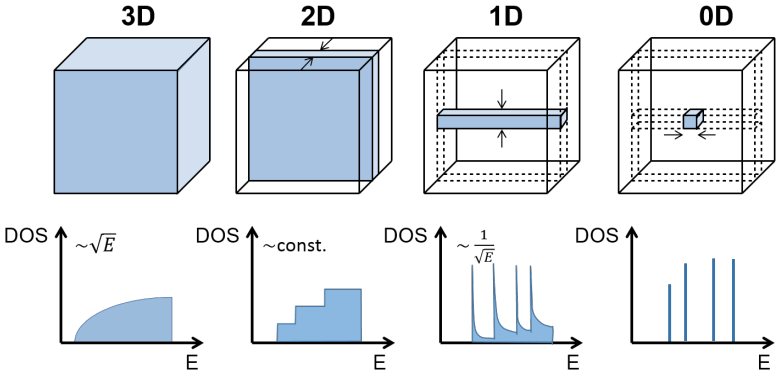

Figure 2.1.: From bulk to lower dimensional semiconductors. Schematic drawing of densities of states (DOS) as a function of dimension. Illustration based on reference[20].

metals, semimetals, and semiconductors were investigated in the 1960s. In the late 1960s, first experiments were carried out on 2D multilayer periodic semiconductors, also referred to as superlattices further discussed in subsection 2.1.3.[21] The first superlattices were realized with classical semiconductors such as GaAs/AlGaAs.[21] Since the 1990s organic-inorganic layered hybrid perovskites have been widely studied.[23] An introduction to this material is provided in subsection 2.3.1. Since the year 2000, transition metal dichalcogenides and honeycomb monolayer materials are in the focus of research.[24] With the 2009 comeback of 3D perovskites due to the discovery of their huge potential for photovoltaic applications, also layered hybrid perovskites came back into the focus. Moreover, since 2014 colloidal perovskite nanocrystals presented in subsection 2.3.2 are an emerging field of research.[25]

2.1.2. Quantum confinement in 2D semiconductors

If the carrier motion in a semiconductor is limited in one dimension to the order of the de Broglie wavelength or the mean free path, if this number is smaller, quantum size effects are observed. The de Broglie wavelength λ_B depends on the effective carrier mass m^* of the electron (or hole) in the crystal and the temperature T:[21]

$$\lambda_B = \frac{h}{p} = \frac{h}{\sqrt{3\, m^*\, k\, T}}. = \frac{1.22\,\mathrm{nm}}{\sqrt{E_{kin}\,/[\mathrm{eV}]}}. \tag{2.1}$$

The perovskite nanocrystals and layered perovskites used for this work can be synthesized with large lateral dimensions of a few hundred nanometers in two dimensions but only a few nanometers in the third dimension. As one dimension is significantly smaller than 100 nm the nanocrystals are termed 2D nanocrystals or nanoplatelets. Therefore, quantum mechanical confinement effects have to be considered when describing the properties of the nanocrystals mathematically. In a 2D semiconductor the exciton can extend in two dimensions homogeneously but is restricted in the third dimension by the surrounding material, e.g. by solvent or by the crystal's ligand.

To describe and solve this mathematically, the quantum mechanical hydrogen problem has to be extended by the spatially depending dielectric constant ϵ. In particular the dielectric mismatch of the crystal and its surrounding and its impact on excitonic properties will be further discussed in subsection 2.1.5. In addition, the electron affinity χ, defined as the energy to remove an electron from the material to vacuum, is spatially depending, as well. So far, there is no general solution to this problem. An exact expression exists, however, for periodically alternating structures.[26]

Infinite quantum well

In a first approximation, one can consider the real crystal as a quantum well (QW) of infinite depth where electron and hole wave function are confined. The eigenenergies E_n (equation 2.4) can then be calculated by solving Schrödinger's equation 2.3 with $V(x) = 0$ and with boundary conditions given by equation 2.2. [19]

$$\Psi(0) = \Psi(L) = 0, \tag{2.2}$$

$$H\Psi_n(x) = \left(-\frac{\hbar^2}{2m}\frac{\partial^2}{\partial x^2} + V(x)\right)\Psi_n(x) = E_n\Psi_n(x), \tag{2.3}$$

$$E_n = \frac{\pi^2\,\hbar^2}{2\,m\,L^2}\,n^2, \tag{2.4}$$

where L is the length of the quantum well, m is the mass of the particle, and n is an integer number. This model overestimates the eigenenergies E_n of a real crystal as the confinement imposed by the ligand is strong but not infinite.

Two-step infinite quantum well

In a refinement of the infinite quantum well, it is taken into account that the nanocrystal is not surrounded by vacuum but by ligands. This leads to an infinite two-step model as sketched in figure 2.2. The boundary conditions for the solution are given by equation 2.5 and 2.6 with the potential given by equation 2.7. [27]

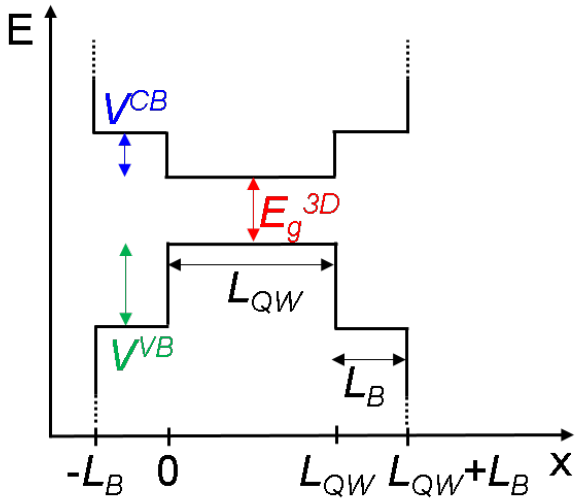

Figure 2.2.: Two-step infinite quantum well. Schematic drawing of a two-step infinite quantum well in real space with L_{QW} the thickness of the nanocrystal and L_B the length of the surrounding ligand.

$$\Psi_{\mathrm{I}}(x_0) = \Psi_{\mathrm{II}}(x_0), \tag{2.5}$$

$$\frac{1}{m^*_{QW}}\frac{\partial}{\partial x}\Psi_{\mathrm{I}}(x_0) = \frac{1}{m^*_{B}}\frac{\partial}{\partial x}\Psi_{\mathrm{II}}(x_0), \tag{2.6}$$

$$V(x) = \begin{cases} V_{CB(VB)} & \text{for } 0 \leq x \leq L_{QW}, \\ 0 & \text{for } -L_B \leq x \leq 0 \text{ or } L_{QW} \leq x \leq L_{QW} + L_B, \\ \infty & \text{else.} \end{cases} \tag{2.7}$$

In equation 2.5 and 2.6, x_0 is the boundary of crystal and ligand, that is $x_0 = 0$ and $x_0 = L_{QW}$. In a real system the assumption of isolated crystals with infinite potential depth outside the ligand is not valid and leads to an overestimation of E_n for strongly confined crystals.

2.1.3. Superlattice and miniband formation

In the experiments, the nanoplatelets and the layered perovskites were found to stack. Thus they can be interpreted as multiple quantum wells with the perovskite crystals forming wells separated by the ligands acting as barriers (figure 2.3 a).[28] The electron and hole wave functions can extend outside the quantum well and hybridize with neighboring platelets, leading to the formation of minibands (figure 2.3 b). For an infinitely long stack of platelets, the one-band effective mass Kronig-Penney model can be applied. Therefore, the separate dispersion for electrons and holes can be written as:[26]

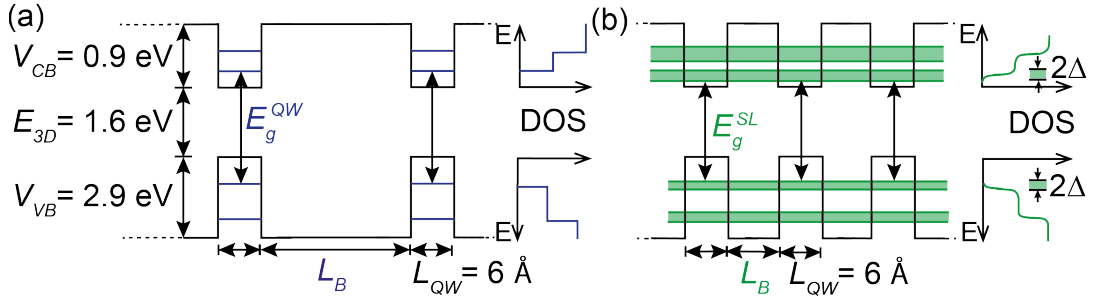

Figure 2.3.: Isolated quantum wells and superlattice formation. (a) Schematic representation of the energy levels in an isolated quantum well and the corresponding step-like density of electronic states. (b) Schematic representation of the energy levels in a quantum well superlattice and the corresponding density of electronic states. Electronic coupling leads to the formation of minibands with a width of 2Δ and a concomitant lowering of the transition energy $E_g^{SL} < E_g^{QW}$. Illustration based on Grahn et al.[29]

$$\cos\left(kL_{QW}\right)\cosh\left(\alpha L_B\right)+\frac{1}{2}\left(\eta-\frac{1}{\eta}\right)\sin\left(kL_{QW}\right)\sinh\left(\alpha L_B\right)=\cos(\delta), \tag{2.8}$$

where

$$k=\sqrt{\frac{2m_{\mathrm{e(h)}}^{QW}E_{\mathrm{e(h)}}}{\hbar^2}}, \tag{2.9}$$

$$\alpha=\sqrt{\frac{2m_{\mathrm{e(h)}}^{B}\left(V_{CB(VB)}-E_{\mathrm{e(h)}}\right)}{\hbar^2}}, \tag{2.10}$$

$$\eta=\frac{\alpha\, m_{\mathrm{e(h)}}^{QW}}{k\, m_{\mathrm{e(h)}}^{B}}, \tag{2.11}$$

where $E_{\mathrm{e(h)}}$ are the quantization energies of the electron and hole, L_{QW} and L_B are the widths of the quantum well and barrier, respectively, $m_{\mathrm{e(h)}}^{QW}$ and $m_{\mathrm{e(h)}}^{B}$ are the effective masses of the electron and the hole in the quantum well and barrier, respectively, and δ is a real parameter equal to $q\left(L_{QW}+L_B\right)$, where $q=\left(\left(2\pi n\right)/\tilde{L}\right)$, $\tilde{L}$ is the length of the lattice, and $n\in\mathbb{Z}$. So far, only free electrons and holes are considered. If these carriers are bound in an electron-hole pair (exciton), the bandgap energy has to be modified according to equation 2.16 given in subsection 2.1.5.

2.1.4. Excitons

The band structure of a solid describes the allowed energies and k-values of electrons and holes. Upon photo-excitation, an electron can be excited into the conduction band (CB), leaving a hole in the valence band (VB). As electrons and holes are charged, they interact electrostatically. The attractive force between them can be derived according to Coulomb's law and is given by:[19]

$$F(r)=-\frac{e^2}{\left(4\pi\,\epsilon_0\right)\epsilon\, r^2}, \tag{2.12}$$

where r is the distance of electron and hole, e is the elementary charge of an electron, and ϵ is the dielectric constant of the solid. If the Coulomb interaction between an electron and hole is large, the two particles are bound together in an electron-hole pair, a so-called exciton. Depending on the exciton binding energy, they may dissociate into free particles at room temperature or they are tightly bound. The exciton binding energy for the n^{th} level in a 3D semiconductor is given by:[19]

$$E_b(n)=\frac{\mu\, e^4}{2\left(4\pi\,\epsilon_0\right)^2\epsilon\,\hbar^2}\frac{1}{n^2}=\frac{\hbar^2}{2\,\mu\, a_0^2}\frac{1}{n^2}, \tag{2.13}$$

where a_0 is the Bohr radius of the hydrogen atom ground state given by equation 2.15 and μ is the reduced exciton mass calculated with the electron and hole effective masses m_e^* and m_h^* depending on the material according to

$$\frac{1}{\mu} = \frac{1}{m_e^*} + \frac{1}{m_h^*}. \tag{2.14}$$

$$a_0 = \frac{4\pi\epsilon_0\hbar^2}{m_0 e^2}. \tag{2.15}$$

There are two types of excitons that are used to describe excitons in solids.[19] Depending on the material, the exciton properties can be described rather as Wannier-Mott or as Frenkel excitons. Wannier-Mott or 'free-excitons' are present in materials with high polarizability (figure 2.4 a). The wave functions are strongly delocalized and the average separation of electrons and holes is much larger than the lattice constant. The electron-hole pair is weakly bound with a binding energy of about 10 meV. For unpolar semiconductors, such as organic semiconductors, Frenkel excitons are present (figure 2.4 b). The hole and electron are localized and tightly bound with binding energies of several tens or hundreds of meV. In semiconductors of low-dimensionality, the exciton picture is altered as described in the next subsection.[19]

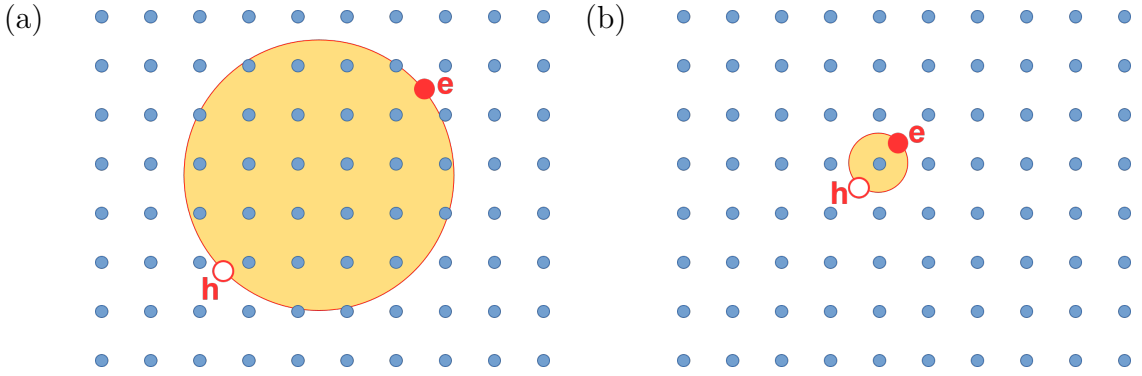

Figure 2.4.: Exciton models. Schematic drawing of (a) Wannier-Mott exciton and (b) Frenkel exciton. Illustration based on reference[19].

2.1.5. Excitons in the high confinement regime

Dielectric confinement effects

When reducing the dimensionality of a semiconductor from 3D to 2D, the basic excitonic properties change fundamentally.[21,30] Figure 2.5 a illustrates schematically this change for a 3D and a 2D semiconducting perovskite crystal in real space. In the 3D crystal, the electrostatic interaction between the electron and hole forming an exciton are screened by

the crystal. In comparison, the exciton in a thin 2D structure is confined to the crystal plane. The reduction from 3D to 2D on its own, neglecting all dielectric effects, already causes the exciton binding energy to increase by a factor of 4 due to geometric reasons only.[31] Additionally, the exciton is not completely screened by the crystal but the electric field lines joining the electron and hole begin to extend outside of the sample as illustrated in the figure. Thus the screening depends largely on the dielectric constant ϵ_s of the medium surrounding the crystal. In case it is smaller than the dielectric constant ϵ_{2D} of the crystal, $\epsilon_s < \epsilon_{2D}$, the dielectric effects will result in enhanced exciton binding energies in the 2D crystal compared to the 3D one. This effect is known as dielectric confinement effect.[32,33] Figure 2.5 b sketches the absorption spectra of a 2D and a 3D crystal. Besides the enhanced exciton binding energy, the bandgap also increases when the dimensionality is reduced.[21,30,31]

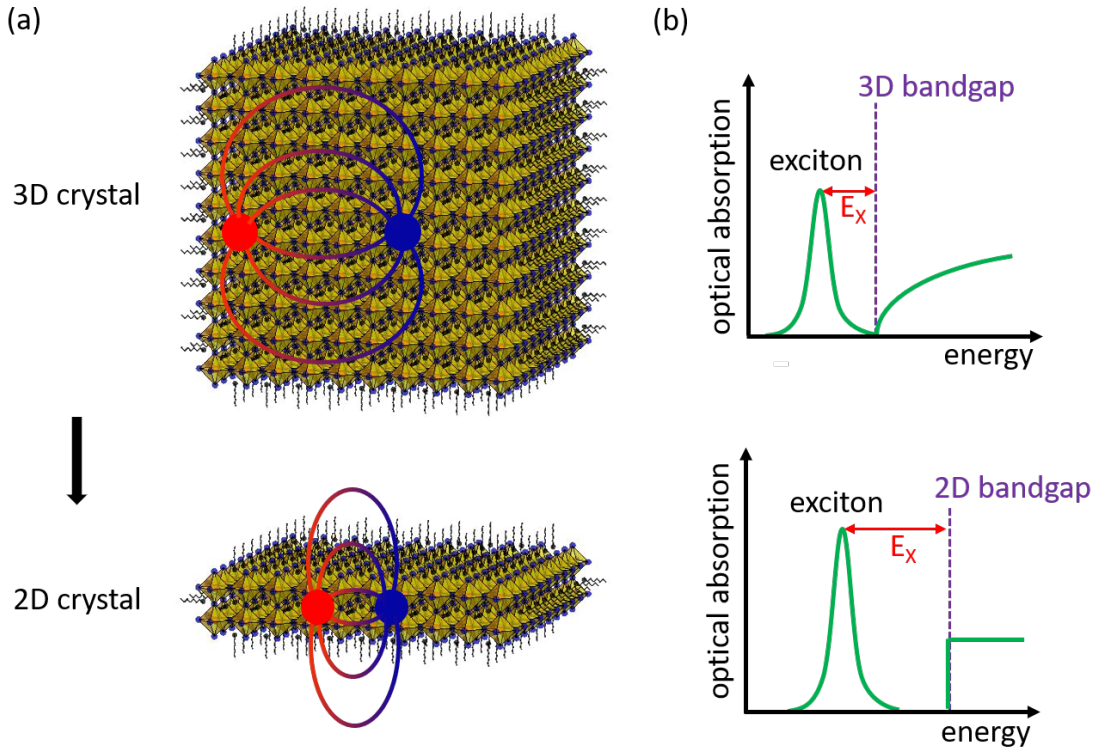

Figure 2.5.: Excitons and absorptions spectra of 3D and 2D crystals. (a) Schematic drawing of electrons and holes bound into excitons in a 3D bulk crystal and a 2D nanoplatelet. In the 3D crystal the Coulombic interaction between the two charges is screened by the surrounding crystal, while this is not the case in the nanoplatelet. (b) Impact of the change in dimensionality on the electronic and excitonic properties, schematically represented by optical absorption. When changing from 3D to 2D, the bandgap and the exciton binding energy E_X are both expected to increase. The excited excitonic states and Coulomb correction for the continuum absorption are not included for reasons of clarity. Illustration adapted from Chernikov et al.[30]

Approximation of exciton binding energies

The transition energy E_χ of the exciton is defined as the difference between the sum of the bandgap energy of the bulk material $E_{\mathrm{g}}^{\mathrm{3D}}$, the quantization energies of the electron and hole, E_e and E_h, and the exciton binding energy E_b:[19]

$$E_\chi = E_g^{3D} + E_e + E_h - E_b. \tag{2.16}$$

The exciton Bohr radius of the three-dimensional exciton is defined as:[34,35]

$$a_B = \frac{\epsilon}{\epsilon_0}\frac{m_0}{\mu}a_0. \tag{2.17}$$

where a_0 is the Bohr radius of the hydrogen atom ground state given by equation 2.15, ϵ_0 and ϵ are the dielectric constants of vacuum and the material, respectively, m_0 is the mass of the free electron, and μ is the effective exciton mass given by equation 2.14.
The exciton binding energy has to be calculated separately in the weak and in the strong confinement regime. In a weak confinement regime, when $L_{\mathrm{QW}} \gg a_{\mathrm{B}}$, the exciton binding energy can be described by the following equation:[34]

$$E_b = \left(\frac{\epsilon}{\epsilon_0}\right)^2 \frac{\mu}{m_0} R_H, \tag{2.18}$$

where R_H is the Rydberg constant, ϵ_0, ϵ , m_0, and μ as in equation 2.17.
In a strong confinement regime characterized by $L_{\mathrm{QW}} \ll a_{\mathrm{B}}$ where L_{QW} is the size of the crystal, the exciton binding energy can be calculated according to the following equation:[26]

$$E_b = -\frac{e^2}{\epsilon^{QW} L^{QW}} \left(ln\left(8\frac{\epsilon^{QW} L^B}{\epsilon^B a_B} \right) - 2C + 2\gamma_0 \right), \tag{2.19}$$

with e the elementary charge, ϵ^{QW} and ϵ^B dielectric constant of the crystal and its surrounding, respectively, a_B the exciton Bohr radius, $C = 0.5774$ the Euler constant, $\gamma_0 = 0.528$ a constant found during the calculation.[26] Following reference[26], it is at least possible to estimate the increase in the exciton binding energy due to a high confinement. Equation 2.19 can only be applied for the following strong limitations to the region of permissible values of the parameters ϵ_{QW}, ϵ_B, L_{QW}, and L_B:[26]

$$\epsilon_B \ll \epsilon_{QW}, \tag{2.20}$$

$$L_{QW} \ll \frac{4\pi\epsilon_0\epsilon_{QW}\hbar^2}{2\mu e^2}, \tag{2.21}$$

$$\frac{\epsilon_B}{\epsilon_{QW}}\frac{4\pi\epsilon_0\epsilon_B\hbar^2}{2\mu e^2} \ll L_B, \tag{2.22}$$

$$\frac{\epsilon_B}{\epsilon_{QW}} L_{QW} \ll L_B \ll \frac{\epsilon_{QW}}{\epsilon_B} L_{QW}. \tag{2.23}$$

2.2. Fundamentals of 3D perovskites

2.2.1. Perovskite crystal structure

Originally, the name "perovskite" was given to the mineral form of $CaTiO_3$, found in the Ural mountains by the German scientist Gustav Rose in 1839.[36] The mineral was named in honor to the Russian mineralogist Lev Aleksevich von Perovski. Today, the term perovskite refers to a broad class of materials that crystallize in the form ABX_3. Hereby B is a cation in the center of an octahedra, formed by six halide ions X (figure 2.6 a). And A is a small organic molecule or inorganic ion located between these octahedra (compare to extended crystal structure in figure 2.6 b).[37] Within the crystal, charge balance has to be achieved. Therefore, if the A and X ions are both monovalent, the B ion has to be bivalent.

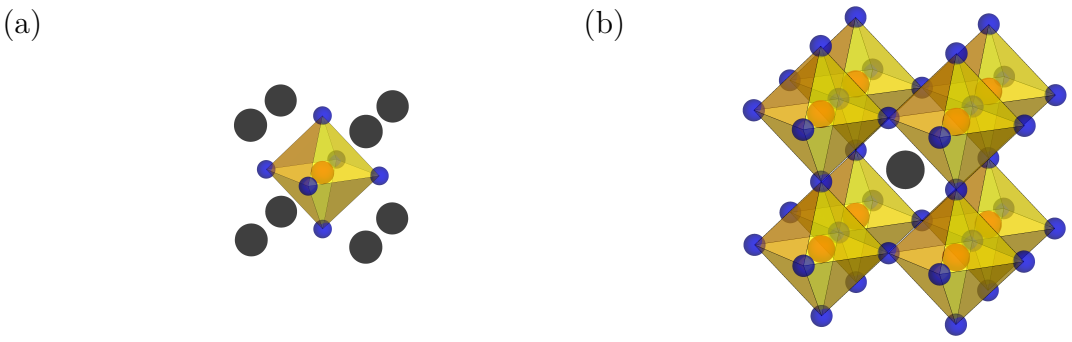

Figure 2.6.: Perovskite crystal structure (a) Schematic drawing of the cubic perovskite structure ABX_3. One unit cell of lead halide perovskites composes of one methylammonium $CH_3NH_3^+$ or Cs^+ ion (A-site ion, black), one lead ion Pb^{2+} (B-site ion, orange), and three halide ions Cl^-, Br^- or I^- (X-site ion, blue). (b) Extended perovskite network structure connected by the corner-shared octahedra indicated in yellow. Illustration based on reference[37].

In addition to charge balance, a size balance is required within the perovskite crystal. The stability of a perovskite is described by the semiquantitative Goldschmidt formula:[38]

$$t = \frac{r_A + r_X}{\sqrt{2} \cdot (r_B + r_X)}, \tag{2.24}$$

where r_A, r_B, and r_X are the ionic radii of the ions A, B, and X. The crystal adopts a perovskite structure similar to $CaTiO_3$ if $0.8 \leq t \leq 1.0$.[37] For smaller values of t the corner-sharing octahedra collapse and the resulting structures can be described as a double chain of $[BX_5]^{3-}$ as depicted in figure 2.7. When the cation is too large, the corner-sharing octahedra turn into single chains of face-sharing octahedra. In the case of $0.8 \leq t \leq 1.0$,

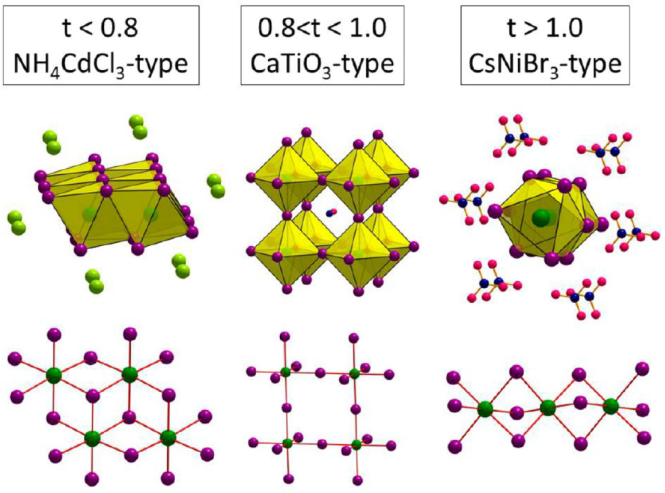

Figure 2.7.: Stability of the perovskite structure according to the semiquantitative Goldschmidt criteria. Structural motifs for the ABX_3 halide compounds as a function of the ionic radii given by the semi-empirical Goldschmidt formula (see equation 2.24). The figure is adapted with permission from Stoumpos et al.[37] Copyright 2015 American Chemical Society.

when corner-sharing octahedra are formed, there are several crystal configurations possible, depending on external stimuli like temperature and pressure. More details are provided in the next subsection.

The requirements on size and charge of the ions leave room for a rich variety of possible ion combinations.[37] In current research, the A component is typically a large anion which can be an ion like cesium (Cs^+) or a small organic molecule like methylammonium ($CH_3NH_3^+$ or short MA). The B ion is typically lead (Pb^{2+}) or tin (Sn^{2+}) and the halide ions are chloride (Cl^-), bromide (Br^-), or iodide (I^-).

The perovskite composition and crystal configuration influence its optical and electronic properties. One of the perovskites investigated in this thesis is bulk-like perovskite nanocrystals composed of methylammonium lead bromide, hereafter abbreviated $MAPbBr_3$. Exemplary for $MAPbX_3$ with X = Cl, Br, I, the band structure of $MAPbI_3$ will be discussed in the next subsection.

2.2.2. Electronic band structure and temperature-dependent effects

The electronic band structure of a solid describes the range of allowed energies and k-values for electrons and holes.[19] Band theory was successfully applied to explain the origin of many physical properties such as optical absorption, excited state lifetime and carrier recombination dynamics. There are several methods that model the band structure of a solid. One of these methods are density functional theory (DFT) calculations.[19]

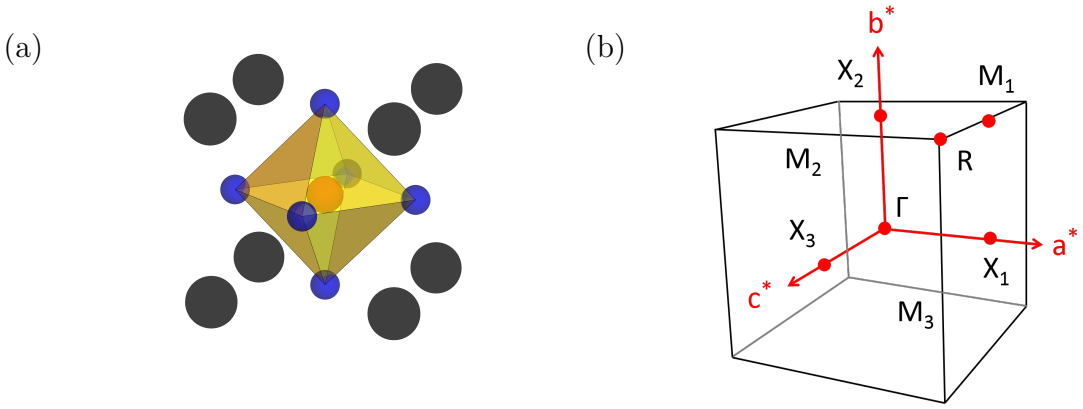

Figure 2.8.: Perovskite crystal structure in real and reciprocal space. (a) Schematic drawing of the cubic perovskite structure ABX_3 in real space and (b) the first Brillouin zone in the reciprocal space. Illustration adapted from Shirayama et al. [39]

Figure 2.8 a depicts the ideal cubic crystal structure in real space with space group $Pm\bar{3}m$. $MAPbBr_3$ crystallizes in the cubic configuration at room temperature. [40] The electronic band structure of the tetragonal phase of $MAPbI_3$, adopted at room temperature, is directly connected to the cubic phase. [39] Figure 2.8 b shows the corresponding Brillouin Zone in reciprocal space. The representation of the unit cell in k-space is the basis to establish a better understanding of the described symmetry. It helps to correlate the crystal structure to the electronic band structure. The points of high symmetry are indicated as usual: The Γ-point is located at the center, the R-points, M-points, and X-points mark the edges, the middle of the edges, and the center of the faces, respectively. In case of a distorted, pseudocubic unit cell, the M-points and X-points are indexed as they differ slightly from each other depending on which edge they are located. [39]

Figure 2.9 a depicts the band structure obtained by Shirayama et al. [39] from DFT calculations. For the calculations the authors assumed a simple pseudocubic structure. $MAPbI_3$ possesses a direct bandgap located at the R-point. The band curvatures for the VB and the CB at the R-point are quite similar. [39] In many semiconductors, the energy dispersion of the bands close to the band extrema can be approximated by a parabolic function: [19]

$$E(k) = \frac{\hbar^2 k^2}{2m^*}, \tag{2.25}$$

with the reduced Planck constant $\hbar$ and m^* the effective masses of the electron (hole) in the CB (VB). From equation 2.25, the effective masses of the charge carriers can be derived as:

$$m^* = \hbar^2 \left[\frac{\partial^2 E}{\partial k^2} \right]^{-1}. \tag{2.26}$$

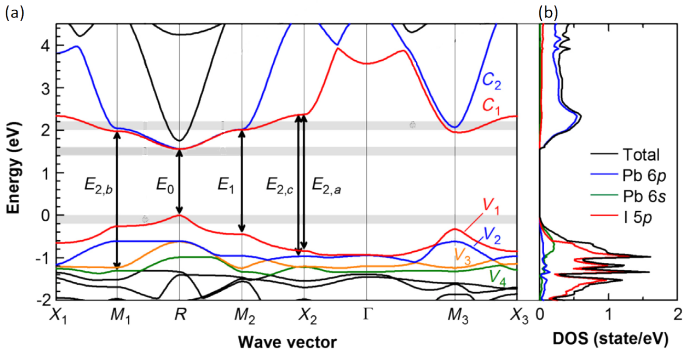

Figure 2.9.: Perovskite band structure and DOS. (a) The band structure of $MAPbI_3$ and (c) DOS as calculated by Shirayama et al.[39]. $MAPbI_3$ possesses a direct bandgap located at the R-point. Reprinted figure with permission from Shirayama et al.[39] Copyright 2016 by the American Physical Society.

The effective masses of electrons and holes near the bandgap of $MAPbI_3$ account for $m_e^* = 0.23m_e$ and $m_h^* = 0.29m_e$, respectively.[41] Thus, the charge carrier effective masses are almost equal allowing good ambipolar charge transport. This is one of the reasons for the material's suitability for solar absorber devices.[41] The VB effective masses of $MAPbBr_3$ and $MAPbCl_3$ are very similar to $MAPbI_3$.[42] For the CB, however, the effective masses show a slight divergence in the order I < Br < Cl.[42]

Figure 2.9 b shows the density of states (DOS) of $MAPbI_3$ corresponding to its band structure as obtained by Shirayama et al.[39] The partial DOS of the Pb *6s*, Pb *6p*, and I *5p* states are shown, as well. Comparing their share to the overall DOS, one can see that Pb *6s* and I *5p* contribute in large parts to the top of the VB. The bottom of the CB is mainly composed of Pb *6p*. The MA ions are further away from the band edges. Their σ/σ^*-bonds are found at least 5 eV below the highest occupied state and 2.5 eV above the lowest empty state, respectively.[43,44] Thus these ions do not directly contribute to the electronic properties of perovskites.[45] Yet, MA has an indirect impact through lattice distortion as discussed further below.
Likewise the MA ions in $MAPbX_3$, the Cs^+ ions in $CsPbX_3$ neither provide significant direct contribution to frontier orbitals. Thus $MAPbX_3$ and $CsPbX_3$ generally parallel one another in terms of the composition of their partial density of states of their lowest electronic transition.[41,44]

The impact of ion exchange on the bandgap

The VB maximum and the electronic band structure of $MAPbI_3$ are determined by the inorganic PbI_6 network. A detailed representation of a bonding diagram for a $[PbI_6]^{4-}$

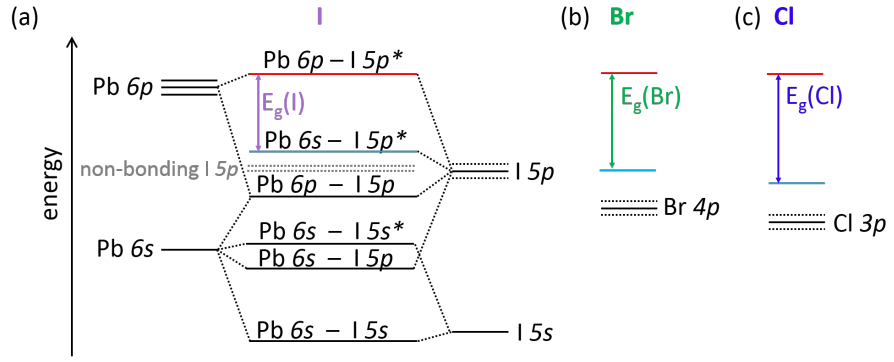

Figure 2.10.: Bonding diagram and bandgap for different halides. (a) Bonding diagram of cluster and energy levels of 3D $MAPbI_3$ according to Umebayashi et al.[46]. Halide exchange leads to larger bandgaps in (b) 3D $MAPbBr_3$ and (c) 3D $MAPbCl_3$ according to Smith et al.[47].

cluster and all hybridized orbitals is depicted in figure 2.10 a. The lowest unoccupied molecular orbital (LUMO) consists of Pb *6p* and I *5s* antibonding orbitals. The highest occupied molecular orbital (HOMO) consists of Pb *6s* and I *5p* antibonding orbitals, respectively. The energy levels close to the band edge in 3D $MAPbI_3$ are indicated, as well. As already mentioned, the partial DOS of $MAPbI_3$ reveals that the VB is in large parts composed of Pb *6s* and I *5p*, similar to the $[PbI_6]^{4-}$ cluster, and the bottom of the CB is mainly composed of Pb *6p*.[46,48] For $MAPbBr_3$ and $MAPbCl_3$ a simplified scheme of the energy levels is shown in figures 2.10 b and 2.10 c, respectively. Halide exchanges alter the bandgap of the perovskites. The smaller the halide, the bigger the bandgap. Thus the bandgap of $MAPbI_3$ is smaller than the one of $MAPbBr_3$. The bandgaps are direct in both materials.[46,47,48]

The influence of phase transitions and octahedral tilting on the bandgap

As discussed above, the MA states are far from the band edges and thus do not directly influence the bandgap.[43,44] Its influence on the band structure lies in its structure directing role.[37] Due to the nature of the ion it causes the adjacent octahedra to leave the ideal position and tilt in regard to each other. This can be assessed by the Pb-I-Pb angle. While the overall architecture is still composed of corner-sharing octahedra, the angle may adopt values from 180° down to 150°. For even smaller angles the structure type changes or the material becomes amorphous.[49,50] The tilt alters the orbital overlap and thus the bandgap of the structure. In recent years, the importance of octahedral tilt has been experimentally and theoretically analyzed. Filip et al.[43] investigated the steric cation size and its impact on the bandgap of 3D perovskites. Ideally, one might expect

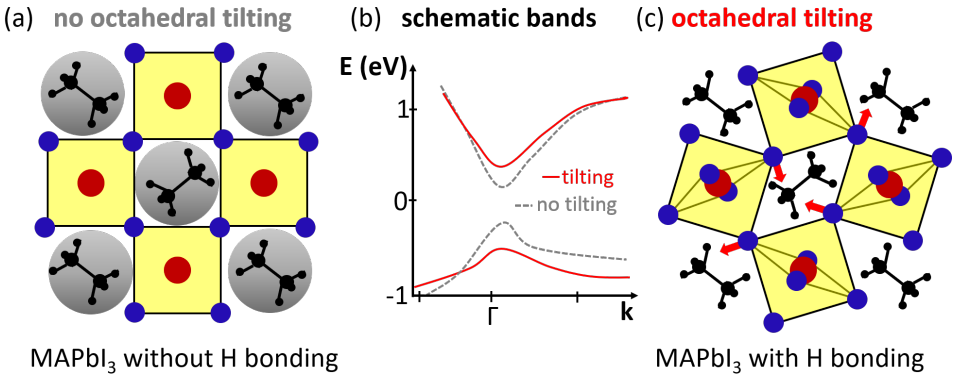

Figure 2.11.: Octahedral tilting and its impact on the bandgap. Schematic drawing of 3D $MAPbI_3$ composed of PbI_6 octahedra and MA ions adopting highly symmetric cubic (a) and an orthorhombic structure (c). Coulombic interactions represented by the red arrows induce octahedral tilting resulting in a larger bandgap as represented by the schematic (b). Drawing adapted from Lee et al.[48]

that all bandgaps in a given ABX_3 series where "BX_3" is identical and only A changes are very similar.[37] However, it is not the ion size alone that determines the degree of octahedral tilting.[48] In organic-inorganic perovskites, also the MA bonding plays an important role. While steric effects determine the tilt in inorganic halide perovskites, hydrogen bonding between an organic A-cation and the halide frame plays a significant role in hybrids.[48] Considering only the steric size of MA, 3D $MAPbI_3$ should adopt an ideal cubic crystal structure at room temperature. However, the MA ions can deform the perovskite lattice through steric and Coulombic interactions. Thus the structure of 3D $MAPbI_3$ at room temperature is not ideal cubic (compare to figure 2.11). The octahedral tilting is the reason for the changes in the electronic structure close to the band edges, changing the bandgap energetics.[37,48]

Temperature-dependence of the bandgap

Without exception, the perovskites undergo a series of structural changes upon application of external stimuli such as temperature or pressure.[37] These phase transitions are fully reversible, even though in some cases the phase change can be kinetically blocked or the transition can be delayed up to several days.[37] The tilting of the octahedra is a central element of these phase transitions. The phase transitions depend on the ion composition of the perovskites. In the case of $MAPbX_3$, the MA ions plays a central role. The structural change is schematically shown in figure 2.12. Starting from the ideal cubic archetype structure in which all B-X-B angles are 180° ($Pm\bar{3}m$ space group), changes in temperature or pressure force the inorganic octahedra to tilt and thereby lower the symme-

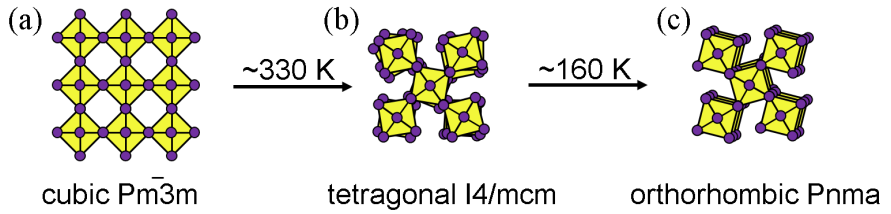

Figure 2.12.: Temperature-induced crystal phase transitions in $MAPbI_3$. In this schematic the PbI_6 octahedra are yellow, the iodine atoms are purple, and the MA cations are not shown to better highlight the distortions of the Pb-I network. (a) In the cubic structure the octahedra are not rotated. (b) In the tetragonal structure the octahedra in neighboring planes along the c axis (pointing out of the plane of projection) rotate in the opposite sense. (c) In the orthorhombic structure the neighboring planes of octahedra along the c axis rotate in the same sense. Drawing based on Whitfield et al. [52]

Structural phase and space group	$MAPbBr_3$	$MAPbI_3$
cubic Pm$\bar{3}$m	$T > 225\,K$	$T > 328\,K$
tetragonal I4/mcm	$157\,K < T < 220\,K$	$162\,K < T < 328\,K$
orthorhombic Pnma	$11\,K < T < 145\,K$	$T < 162\,K$

Table 2.1.: Tabular representation of structural phase transition induced by temperature in $MAPbBr_3$ and $MAPbI_3$ as reported by Swainson et al. [51] and Baikie et al. [53], respectively.

try. Above 330 K, the perovskite adopts a cubic structure with space group Pm$\bar{3}$m and the MA ion can rotate freely. [51] When the crystal is cooled, the MA ions switch between stable configurations and the crystal structure is tetragonal with space group I4/mcm below 330 K. Below 160 K the MA ion position is fixed and the perovskite adopts an orthorhombic configuration with space group Pnma. [51,54] Analogously to $MAPbI_3$, $MAPbBr_3$ undergoes the same phase transitions but at different temperatures as summarized in table 2.1. For $CsPbBr_3$ nanocrystals there is still an ongoing debate on the crystal structure, both cubic and orthorhombic phases have been reported in literature. [55,56]

With the phase transition, the Pb-I-Pb bonding angle changes abruptly, altering also the bandgap. When the temperature increases gradually, the bandgap of $MAPbX_3$ and $CsPbX_3$ undergoes a gradual blue-shift. That is unlike most well-known semiconductors like Si, Ge, GaAs or InAs that undergo a red-shift. [57] This unusual trend originates from the inverted band structure of perovskite. While conventional semiconductors like GaAs possess a *p*-type character VB and an *s*-type character CB, the VB maximum of $MAPbI_3$ is determined by Pb *6s* and I *5p* states and the CB minimum by non-bonding Pb *6p* states. When the unit cell volume V decreases with temperature, the interactions of the anti-bonding Pb *6s* and I *5p* states are enhanced, resulting in a raise of the VB maximum. The

CB minimum is nearly unchanged by the shrinking unit cell and thus perovskites exhibit a positive gap deformation potential α_V given by:[58,59]

$$\alpha_V = \frac{\partial E_g}{\partial \ln(V)} > 0. \tag{2.27}$$

Interestingly, literature reports of such observations are limited to a small group of materials. Besides bulk $MAPbX_3$, $CsPbX_3$, and $CsSnX_3$ perovskites, black phosphorus,[60] lead salts (PbS, PbSe, and PbTe),[61,62,63] and cuprous halides (CuCl, CuBr, and CuI)[64] are known to exhibit a similar behavior.

Temperature-dependence of phonon-exciton interactions

Considering the fixed energies between ground state and excited states in case of excitons, one could expect sharp lines in the emission and absorption spectra. However, these lines are significantly broadened around the transition energy. At temperatures close to 0 K and assuming the absence of further scattering mechanisms such as phonon emission, the linewidth for a single emitter is given by a Lorentzian line shape:[65]

$$I(E) = \frac{I_0}{(E - E_0)^2 + \left(\frac{\gamma}{2}\right)^2}, \tag{2.28}$$

with a FWHM $\gamma = \Delta E$ given by the uncertainty principle $\Delta E \cdot \tau \geq \hbar$ with the lifetime τ of the excited state. Herein, γ is also referred to as the natural linewidth. For $T \neq 0$, there are further mechanisms that induce an additional spectral broadening. The temperature-dependent broadening of the PL is mainly caused by lattice vibrations in a crystal which perturb the motions of the electrons. The interactions between phonons and charge carriers are attributed to three different types, namely the deformation potential, piezoelectric effects and the Fröhlich interaction.[66] The deformation potential describes the interactions of an electron with acoustic or optical phonons. It can be viewed as equivalent to displaced ions in the crystal analogous to homogeneously induced strain altering the electronic band structure of the crystal. The piezoelectric interaction can occur in crystals that lack a center of symmetry. In these crystals strain may induce electric fields influencing the interaction of phonons and electrons. In contrast, the third type of interaction, the Fröhlich interaction, is not strain induced but describes Coulombic interactions. Due to displacements of oppositely charged out-of-phase atoms, electrons interact with the optical phonon modes.

These interactions vary with temperature due to their dependence on the phonon population and and thus the PL emission linewidth changes with temperature. The most dominant contributions to the PL broadening are interactions with optical and acoustic

phonons:[67,68]

$$\Gamma(T) = \Gamma_{AC} + \Gamma_{LO} = \gamma_{AC}\, T + \frac{\gamma_{LO}}{\exp\left(\frac{E_{LO}}{kT}\right) - 1}. \tag{2.29}$$

The first term (Γ_{AC}) stems from excitons coupling to acoustic phonons. It mainly relates to the deformation potential and Γ_{AC} depends linearly on temperature with a factor γ_{AC}. The second term, Γ_{LO} with the Fröhlich coupling constant γ_{LO}, describes the exciton-longitudinal optical phonon scattering. It is associated with the Bose-Einstein distribution of LO phonons given by $\left(\exp\left(\frac{E_{LO}}{kT}\right) - 1\right)^{-1}$ with the energy of the LO phonons E_{LO}, the Boltzmann constant k, and the temperature T.
Additionally, there is a temperature-independent term Γ_0 contributing to the broadening. It includes the inhomogeneous broadening Γ_{inh} that arises from inhomogeneities of a sample stemming e.g. from size distribution of crystals in a sample or by defect states in a single crystal. The inhomogeneous broadening can be described by a Gaussian line shape. Neglecting the natural linewidth, $\gamma \ll \Gamma_{inh}$, equation 2.29 becomes:[65,67,68]

$$\Gamma_{total}(T) = \Gamma_0 + \Gamma_{AC} + \Gamma_{LO} = \Gamma_0 + \gamma_{AC}\, T + \frac{\gamma_{LO}}{\exp\left(\frac{E_{LO}}{kT}\right) - 1}. \tag{2.30}$$

A convolution of all broadening effects would result in a Voigt line shape with many free parameters.[65] Instead, a simple Gaussian line shape is often a very good approximation of the Voigt function and is thus commonly used and likewise in this thesis.

Excitons and exciton binding energies

The roles of excitons and free carriers in perovskites have been discussed in many studies.[69,70,71,72] To this day the reported E_b values vary widely. In the case of $MAPbI_3$, these values range from about $E_b = 2 - 55\,\text{meV}$[73], measured with various different experimental techniques.[25,74] For $MAPbBr_3$ the exciton binding energies are reported with values ranging from about $E_b = 25 - 76\,\text{meV}$[75,76,77]. In general, semiconductors with a larger bandgap display stronger excitonic features as the background screening is reduced. Accordingly, $MAPbBr_3$ shows increased excitonic behavior compared to $MAPbI_3$.[78] The reported exciton binding energy for $CsPbBr_3$ amounts to $E_b = 37 - 44\,\text{meV}$[55,79,80] and is thus comparable to the values reported for $MAPbBr_3$.

2.2.3. Charge carrier recombination dynamics

Charge carrier recombination mechanisms and the resulting dynamics play an important role in the functioning of semiconducting materials in electronic devices. For solar cells,

the charge carrier lifetime determines the time available to extract charge carriers. To determine charge carrier lifetimes experimentally, photoluminescence (PL) lifetime measurements are carried out. The resulting decay curves for the charge carriers can be analyzed. The decay of a free charge carrier density $n(t)$ can be expressed through the rate equation [81]

$$\frac{dn}{dt} = -k_1 n - k_2 n^2 - k_3 n^3. \tag{2.31}$$

Each term in this equation depends on the charge carrier concentration n and describes different contributing mechanisms. k_i are the recombination coefficients. k_1 stems from exciton recombination or trap state mediated recombination (figure 2.13 a). k_2 originates from free electron and hole recombinations (figure 2.13 b) whereas k_3 represents the contribution from Auger recombinations (figure 2.13 c).

When the decay curves can be fitted with a monoexponential function, this can be due to either excitonic recombination or due to trap state related recombination of either electron or hole. In order to distinguish these two mechanisms, excitation density dependent measurements can be performed. In the presence of trap state assisted recombination, their contributions will vanish at sufficient high densities due to a saturation of trap states.

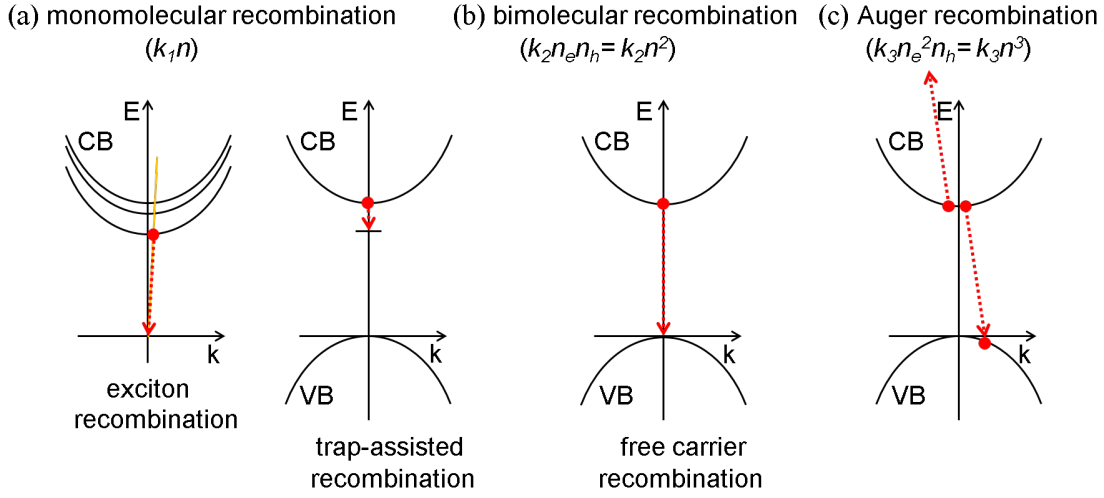

Figure 2.13.: Schematic drawings of charge carrier recombination mechanisms active in organic-inorganic metal halide perovskites. (a) Trap-assisted recombination is a monomolecular process. It involves the capture of either an electron (as depicted) or a hole in a specific trap state, such as a defect. Exciton recombination is a monomolecular process, as well. (b) Bimolecular recombination may occur between electrons and holes, from either the CB minimum to the VB maximum or states higher in the band. (c) Auger recombination is a higher-order process that involves at least three particles. The energy of an electron (or hole) is thereby transferred to another electron (or hole) allowing non-radiative recombination with a hole (or electron). All processes have to satisfy energy and momentum conservation. Illustration adapted from reference [81].

The bimolecular charge carrier recombination rate constant k_2 reflects intrinsic electron-hole recombination. It depends on both, electron (n_e) and hole (n_h) densities. If the density of both carrier types is equal, as it is the case for $MAPbI_3$, then the recombination depends on $n_e n_h = n^2$.[81]
Finally, k_3 is the Auger rate constant. Auger recombination is a many-body effect that involves the recombination of an electron and a hole accompanied by energy or momentum transfer to an additional electron or hole. Potentially, also a phonon is absorbed or emitted. Auger effects are highly depending on excitation densities. Experimentally, they can be avoided when the excitation densities are chosen sufficiently low.[81]

2.3. Perovskites of lower dimensionality

So far, bulk or 3D perovskites were discussed. As explained in section 2.1, a decrease in dimensionality of a semiconductor results in altered electronic and optical properties. In this section, two representatives of perovskites of lower dimensionality are discussed, namely layered hybrid perovskites and colloidal perovskite nanocrystals. The former are quasi-2D like heterostructures and the latter may be synthesized down to 0D. In the following subsections both structures are shortly presented.

2.3.1. Layered hybrid perovskites

In the late 1980s, layered hybrid perovskites were described for the first time.[23] In the following decade they were intensively investigated for optoelectronic applications.[82,83] In recent years, when 3D perovskites have come into the focus of research, the interest in layered hybrid perovskites has risen as well.

Crystal structure

The above mentioned 3D perovskites with the general formula ABX_3 have rather rigid structural constraints. Despite from the required charge balance, in particular the size constraint for each of the ions limits the choice of ions.[37] Layered hybrid perovskites belong to the extended perovskite family that includes perovskites of lower dimensionality. Like their 3D-parent structure, they are composed of corner-sharing BX_6 octahedra. Note that the corner-sharing octahedra network determines the dimensionality of the resulting perovskite structure. In case of layered hybrid perovskites, the octahedra form 2D sheets that are separated by the A cations. There are no known size restrictions for the A site ion.[28,84] It has to have a functional group that binds ionically to the octahedra and stabilizes them. The organic moiety can then be chosen from a variety of chemical structures.

Thereby, the properties of the moiety can for example be chromophoric, luminescent, conducting, polarizable or polymerizable.[28,84]

In this thesis, layered hybrid perovskites of the general formula A_2BX_4 are investigated. The A site is an alkylammonium with ammonium functional group and an aliphatic moiety of different length as sketched in figure 2.14. The B and X sites are lead (Pb) and iodide (I), respectively. The PbI_6 octahedra compose 2D sheets that are stabilized by the ammonium functional group of the A-site ion. The chemical correct formula $(C_lH_{2l+1}NH_3)_2PbI_4$ is hereafter abbreviated as C_lPbI_4 where l is the number of C-atoms giving the length of the chain. Samples with $l = 4, 6, 8, 10, 12, 16, 18$ were prepared for this work. In principal any number of C-atoms between 4 and 18 is possible, also the odd numbers.[85,86,87] As this thesis aims to investigate the influence of the ligand length on the optical properties of the structures, only a few lengths between 4 and 18 were prepared for this thesis.

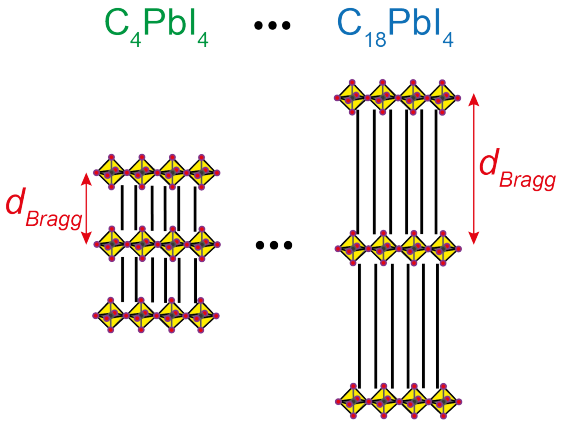

Figure 2.14.: Schematic drawing of layered hybrid perovskite structures of C_lPbI_4. Like their 3D-parent structure, layered 2D perovskites are composed of corner-sharing PbI_6 octahedra (yellow). The PbI_6 octahedra form 2D sheets that are stabilized by the ammonium functional group of the A site ion. Here, the A site is an alkylammonium with ammonium functional group and an aliphatic moiety (black vertical lines) of different length. Illustration based on Saporov et al.[84].

Band structure and type-I alignment

In general, a reduction in dimensionality of the 3D perovskite structure leads to enhanced bandgap energies E_g.[34,88] Moreover, for a family of structures comprising of the same metal halide octahedra, the lowest energy electronic transition follows the trend $E_g^{3D} < E_g^{2D} < E_g^{1D} < E^{0D}_{\mathrm{HOMO-LUMO}}$. When the dimensionality of the BX_6 octahedra network is reduced, the bandwidth of both the CB and VB is reduced accordingly, resulting in a larger energy difference between the VB maximum and CB minimum. In particular, the reduced band dispersion becomes evident orthogonal to the organic-inorganic interface

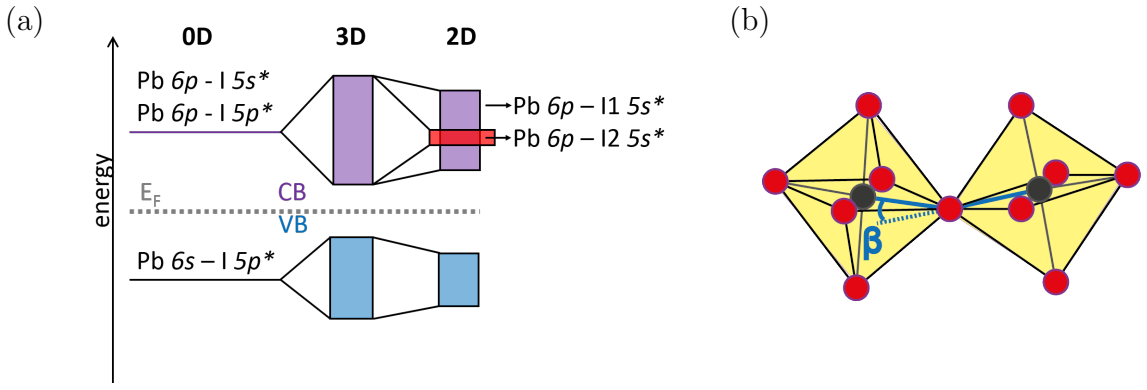

Figure 2.15.: Reduction in dimensionality and octahedral tilting lead to a narrow bandwidth in 2D perovskite compared to the 3D analogue. (a) Atomic orbitals contributing to VB and CB in 3D versus 2D perovskites. The reduction in dimensionality and octahedral tilting result in a narrower bandwidth in the 2D crystal compared to the 3D counterpart according to Umebayashi et al.[46]. (b) The tilt of the PbI_6 octahedra can be quantified by the Pb-I-Pb tilt angle β.

in layered hybrid perovskites. Figure 2.15 a depicts a schematic drawing of the bandwidth when the dimensions are reduced from 3D to 2D for $MAPbI_3$.[46] As the total DOS shows, the 2D crystal consists of a number of localized bands in contrast to the wide bands of the 3D counterpart. Additionally, the bandwidth further narrows due to octahedral tilting.[46] Thereby the angle between two adjacent octahedra, accessed through the Pb-I-Pb bridging tilt angle, differs from the ideal of 180°. This difference is the tilt angle β schematically depicted in figure 2.15 b.

Most theoretical studies of layered hybrid perovskites either provide a general description of the electronic band structure, mostly using density functional theory (DFT),[46,88,89,90] or focus on the excitonic coupling using effective mass parameters for the carrier dispersion and abrupt dielectric confinement schemes.[7,91] As layered hybrid perovskites are very large systems for DFT simulations, their simulation might reach limitations regarding computational resource.[54] A fruitful alternative to DFT calculations was already proposed earlier by Mitzi and coworkers[28] based on a quantum well (QW) concept. In this picture, the inorganic 2D perovskite layers are interpreted as quantum wells for electrons and holes separated by the organic ligands forming a barrier, leading to a picture of a type-I heterostructure as depicted schematically in figure 2.16.

Excitons and exciton binding energies

As mentioned earlier, going from 3D to 2D leads to a 4-fold increase of the exciton binding energy due to spatial confinement.[31] Additional, the mismatch of dielectric constants in

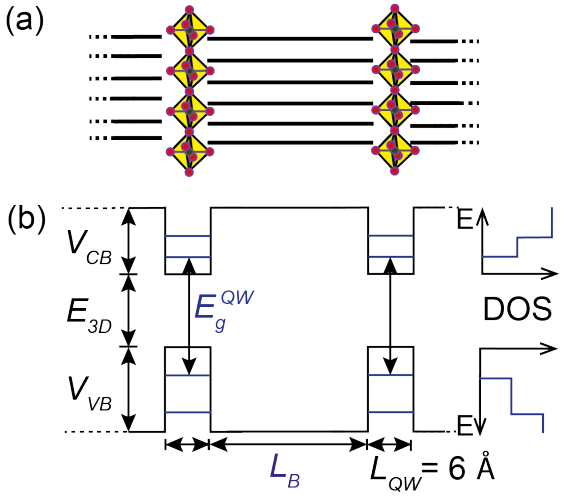

Figure 2.16.: Layered hybrid perovskite as quantum well heterostructure. (a) Sketch of layered hybrid perovskite comprised of inorganic PbI_6 octahedra arranged in 2D sheets that are separated by organic ligands. (b) In the quantum well concept, the inorganic 2D perovskite layers are interpreted as quantum wells for electrons and holes separated by the organic ligands forming a barrier. The energy level scheme is a type-I heterostructure. Illustration based on Mitzi et al. [28].

quantum well and barrier leads to dielectric confinement and further enhancement of the exciton binding energies. [31] This includes reported values of 320 meV for $C_{10}PbI_4$ and 360 meV for C_4PbI_4. [84] Due to the above mentioned quantum and dielectric confinement effects the nature of the exciton is hard to determine. It was proposed that it is Wannier type, however with a small radius. [84]

2.3.2. Colloidal perovskite nanocrystals

The first $MAPbX_3$ (X=Br, I) nanocrystals were synthesized by Kojima et al. [9] in 2009. Hereby, the perovskite precursor solutions were spin coated onto a porous material and formed upon the fast evaporation of the solvent. The nanocrystals had a size of 2-3 nm and were successfully incorporated as sensitizers into dye-synthesized solar cells. In 2012, Kojima et al. [92] reported the preparation of luminescent perovskite nanocrystals, again based on a template method.

The first solution-based synthesis of colloidal $MAPbBr_3$ nanocrystals was reported by Pérez-Prieto and colleagues [18] in 2014, the year when the work for this thesis started. Unlike the templating method, the solution-based synthesis uses an additional large organic cation (octylammonium, OA). This ion has the same functional group as the small organic A-site cation methylammonium. Thus OA binds to the perovskite crystal but, unlike MA, cannot incorporate into the 3D perovskite crystal structure (figure 2.17 a, b).

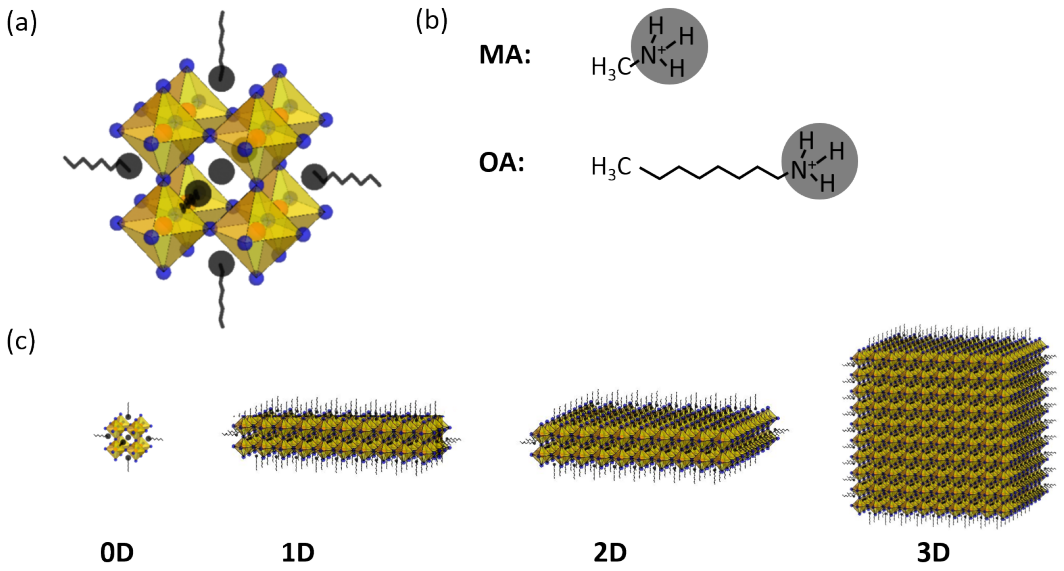

Figure 2.17.: Low-dimensional perovskite crystal geometries. (a) Sketch of a $MAPbX_3$ nanocrystal surrounded by octylammonium (OA) ligand chains pointing outwards. (b) Methylammonium (MA) fitting in the 3D crystal structure and OA, too big for this crystal structure but with same ammonium functional group. (c) Possible nanocrystals: perovskite zero-dimensional quantum dots (0D), one-dimensional nanowires (1D), two-dimensional nanoplatelets (2D), and bulk-like nanocrystals (3D).

Consequently, this cation acts as a capping ligand and prevents further crystal growth. In principle, this approach can yield nanocrystals of various sizes and dimensions, such as perovskite quantum dots (0D), nanowires (1D), nanoplatelets (2D) and bulk-like (3D) nanocrystals (see sketch in figure 2.17 c).
Pérez-Prieto and colleagues [18] obtained spherical particles on nm scale. Figure 2.18 a displays an HRTEM image of such a particle proving its highly crystalline structure. The sketch shows the corner-sharing octahedra of $MAPbBr_3$ perovskite. Figure 2.18 b displays a photograph of a dispersion of these nanoparticles under UV-light. The PL spectra of the particles in solution and on substrate are shown in figure 2.18 c with PL peaks located at 527 nm and 530 nm, respectively. Figure 2.18 d displays TEM images of the circular nanoparticles. Some rectangular features are visible especially behind the circular particles, hinting at a more complex morphology of the obtained nanocrystals.

In this thesis, $MAPbBr_3$ nanocrystals with octylammonium as ligand were synthesized with a new variation to the synthesis of Pérez-Prieto and colleagues [18], yielding nanoplatelets of different thicknesses. For the first time the quantum size effect in these nanoplatelets is quantitatively described through model calculations. Furthermore, thickness-dependent and temperature-dependent photoluminescence lifetime measurements are carried out. The recorded lifetimes decrease with thinner nanoplatelets as the exciton binding energy

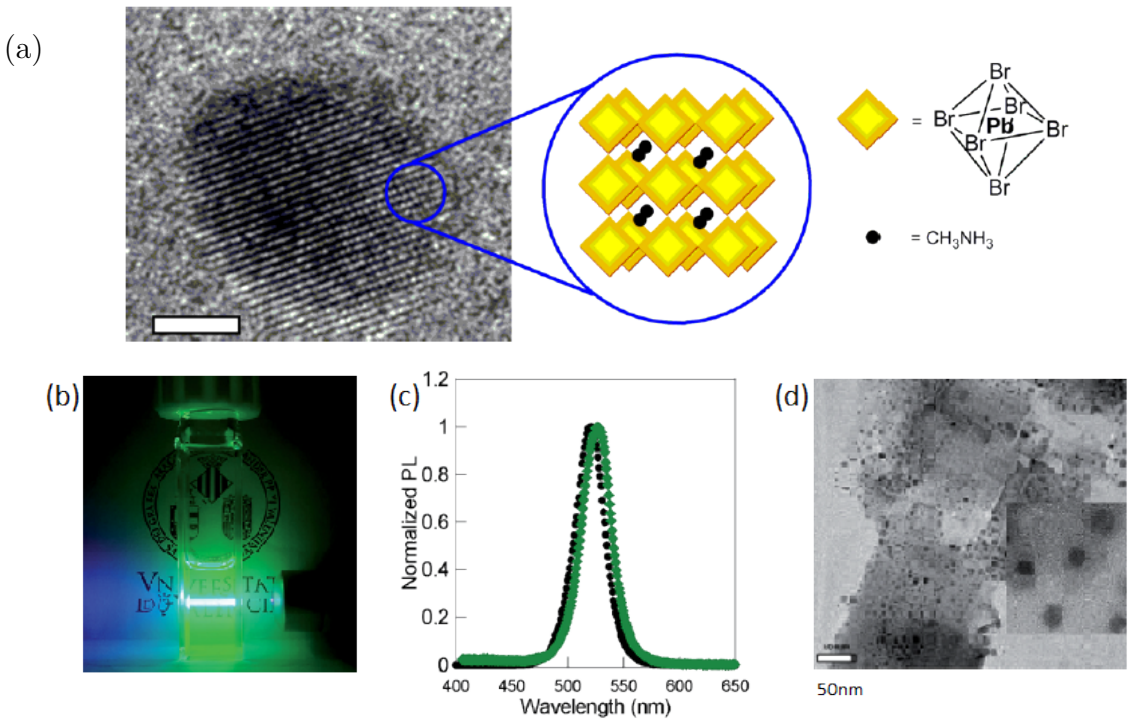

Figure 2.18.: $MAPbBr_3$ perovskite nanocrystals. (a) HRTEM image of an isolated, highly crystalline $MAPbBr_3$ nanocrystal (scale bar: 2 nm) together with a schematic representation of the perovskite unit cell. Adapted from Schmidt et al.[18]. Copyright American Chemical Society 2014. (b) Image of the toluene dispersion of $MAPbBr_3$ nanocrystals under UV-laser pointer excitation. (c) Normalized PL spectra of $MAPbBr_3$ nanocrystals in toluene (green) and on substrate (black). (d) TEM images of perovskite nanocrystals (scale bar: 50 nm). Figure 2.18 (b) to 2.18 (d) adapted with permission from Gonzalez-Carrero et al.[93] Copyright Royal Society of Chemistry 2015.

increases. A theoretical model considering acoustic and optical phonons as the main sources for scattering of excitons, shows that the former dominate at temperatures below 90 K and the latter above this temperature.

The interlayer distance in layered hybrid perovskites is systematically varied to investigate its impact on structure-function relationships and electronic coupling between the perovskite layers. It is found that the optical bandgap is determined mainly by two parameters, namely the tilt angle of the perovskite octahedra and the interlayer distance.

3. Methods and materials

This chapter provides an overview of all synthesis methods and measurement techniques used in this thesis. Three different types of perovskites are synthesized for further investigation in the results part of this thesis. The first one are colloidal perovskite nanoplatelets of different thicknesses based on methylammonium lead bromide ($MAPbBr_3$). The second one are cesium lead bromide ($CsPbBr_3$) nanoplatelets of $n = 3$ layers of unit cells in thickness. The third one are polycrystalline films of layered hybrid perovskites with varying interlayer distance based on alkylammonium lead iodide (C_lPbI_4). In the results part, structure-function relationships will be discussed for these three types of perovskites with respect to their dimensionality, geometry, and optical properties. The measurement techniques can be divided into those used for structural characterization and those for optical characterization. First, the methods used for structural analysis, including X-ray diffraction and electron microscopy are explained. Then the optical characterization techniques including absorption and photoluminescence (PL) measurements as well as a streak camera and a time-correlated single photon counting (TCSPC) setup for temperature-dependent time-resolved PL spectroscopy are presented.

3.1. Syntheses

3.1.1. Colloidal $MAPbBr_3$ nanoplatelets of different thicknesses

The synthesis of the $MAPbBr_3$ nanoplatelets was carried out by a modification of the synthesis reported by Schmidt et al.[18] Three precursor salts are needed for the procedure, namely octylammonium bromide (OABr), methylammonium bromide (MABr), and lead bromide ($PbBr_2$). As depicted in figure 3.1, these three precursors are first added in a good solvent for perovskites (DMF). The perovskite crystals will only form once the precursor salts are added to an antisolvent for perovskite (toluene).
In a first step, the precursor salts were prepared. The precursor OABr was prepared by adding HBr to octylamine. Likewise, the precursor MABr was prepared by adding HBr to a solution of methylamine in ethanol. For both precursors the acid was added in slight molar excess (1.1 : 1.0 ratio) to ensure full protonation of the precursor amines. Subsequently, the ammonium salts were dried and crystallized in a rotary evaporator. Stock solutions of $PbBr_2$, OABr, and MABr were prepared using dimethylformamide (DMF) as solvent. Hereafter, the three precursors were mixed and diluted in DMF such that a series of precursor solutions was obtained with fixed total concentration of $PbBr_2$ (0.05 M) and ammonium ions (0.05 M) but a varying fraction of OABr. All solutions were kept at 80 °C to ensure full solubilization. In order to induce crystallization of the desired product, the precursor solution was added drop by drop into toluene under vigorous stirring. Here, 20 mL of toluene for every mL of precursor solution was used. The resulting precipitates

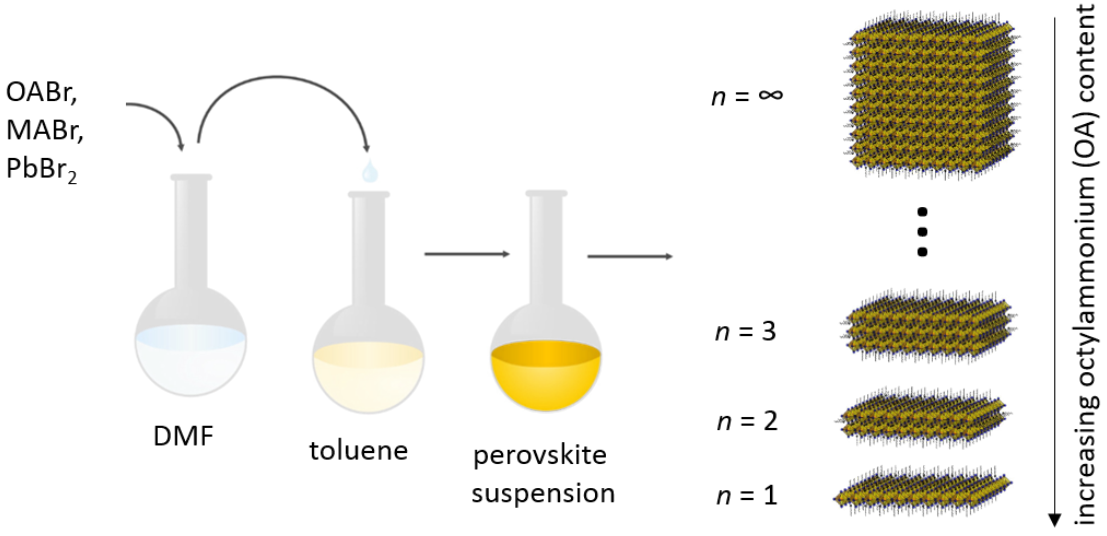

Figure 3.1.: Schematic of the synthesis of the perovskite nanoplatelets. The three precursor solutions are joint in DMF and subsequently added dropwise into toluene where the perovskite nanocrystals precipitate.

were centrifuged and subsequently redispersed in neat toluene through mild sonication and stirring. Finally, each sample underwent three full washing cycles with toluene. These purification steps ensure that excess ligands are extracted from the suspension. Thus, the final perovskite suspension is stable and can be drop casted or spin coated on substrate. Analyses regarding the composition, shape and optical properties of the product are described in chapter 4 to 5. Results on $MAPbI_3$ nanoplatelets similarly synthesized to the $MAPbBr_3$ nanoplatelets can be found in appendix sections A.6 and A.7.

3.1.2. Synthesis of $CsPbBr_3$ nanoplatelets

The $CsPbBr_3$ nanoplatelets with 3 layers of unit cell thickness were prepared by Dr. Yu Tong at the same chair where the experiments for this thesis were conducted. In a first step, the precursors were prepared. For the Cs-oleate precursor 0.1 mmol Cs_2CO_3 powder was dissolved in 10 ml oleic acid at 100 °C under continuous stirring. For the $PbBr_2$ precursor solution 0.1 mmol $PbBr_2$ powder, 100 µl oleylamine, and 100 µl oleic acid were dissolved in 10 ml toluene at 100 °C. These ligands help to solubilize $PbBr_2$ in toluene.
The synthesis was carried out at room temperature and under ambient atmosphere. The thickness of the synthesized nanoplatelets was controlled through varying the ratio of the two precursors, Cs-oleate and $PbBr_2$ precursor, and the amount of acetone, which acts as an antisolvent. In the synthesis for the 3 ML sample, 150 µl Cs-oleate precursor, 1.5 ml of $PbBr_2$ precursor, and 2 ml acetone were used.
For the synthesis $PbBr_2$-oleylamine/oleic acid precursor was given into toluene. Herein, the Cs-oleate precursor is added under vigorous stirring at room temperature. After 5 s, acetone is added which initiates the formation of nanoplatelets. The solution was stirred for 1 min and subsequently centrifuged at 4000 rpm for 3 min. The precipitate was redispersed in 2 ml of hexane.

3.1.3. Layered hybrid perovskites with varying interlayer spacings

The layered hybrid perovskites investigated in this thesis are based on *n*-alkylammonium lead iodide $(C_lH_{l+1}NH_3)_2PbI_4$ with $l = 4, 6, 8, 10, 12, 16$, and 18. Hereafter the formula will be abbreviated as C_lPbI_4. These types of perovskites are well-known in literature.[23,85,86,87] For their synthesis two precursor salts were used. One precursor was *n*-alkylammonium iodide ($C_lH_{2l+1}NH_3I$) and the other one was lead iodide (PbI_2). These salts were dissolved in DMF and upon evaporation of the solvent the perovskites formed according to

$$2\,C_lH_{2l+1}NH_3^+\,I^- \;+\; Pb^{2+}\,I_2^- \;\rightarrow\; (C_lH_{2l+1}NH_3^+)_2\,Pb^{2+}\,I_4^-. \tag{3.1}$$

The precursor salt $C_lH_{2l+1}NH_3I$ was obtained by reacting the long-chain amine with HI in slight excess to ensure full protonation (ratio of 1.0 : 1.1). Subsequently, the ammonium salts were dried in a rotary evaporator and washed three times with diethylether. The products were light yellow to white powders. These precursors were dissolved in DMF such that a 1 molar solution was obtained. The other precursor salt, PbI_2, was dissolved in DMF to obtain a 0.3 molar solution. Small amounts of the precursor stock solutions were mixed in a stoichiometric ratio PbI_2 to *n*-alkylammonium iodide of 1:2. This mixture was heated to 70 °C in an oil bath and drop casted on a glass substrate. The substrate was heated to 70 °C to ensure full evaporation of the solvent. Hereby a polycrystalline film of perovskites was obtained. Before any of the experiments described in chapter 6 was carried out, the substrates were left at room temperature for several hours to ensure that the crystal phase was the one that the respective crystals adopt at room temperature.

Electron microscopy on polycrystalline films of layered hybrid perovskites

As mentioned above, layered hybrid perovskites based on C_lPbI_4 are a well-known type of perovskites. Therefore, first analyses of the drop casted films are presented here in the methods section. Figure 3.2 displays exemplarily a scanning electron microscopy (SEM) image of $C_{10}PbI_4$. It comprises of a polycrystalline film with crystalline domains in µm size with a maximum of several tens of µm.

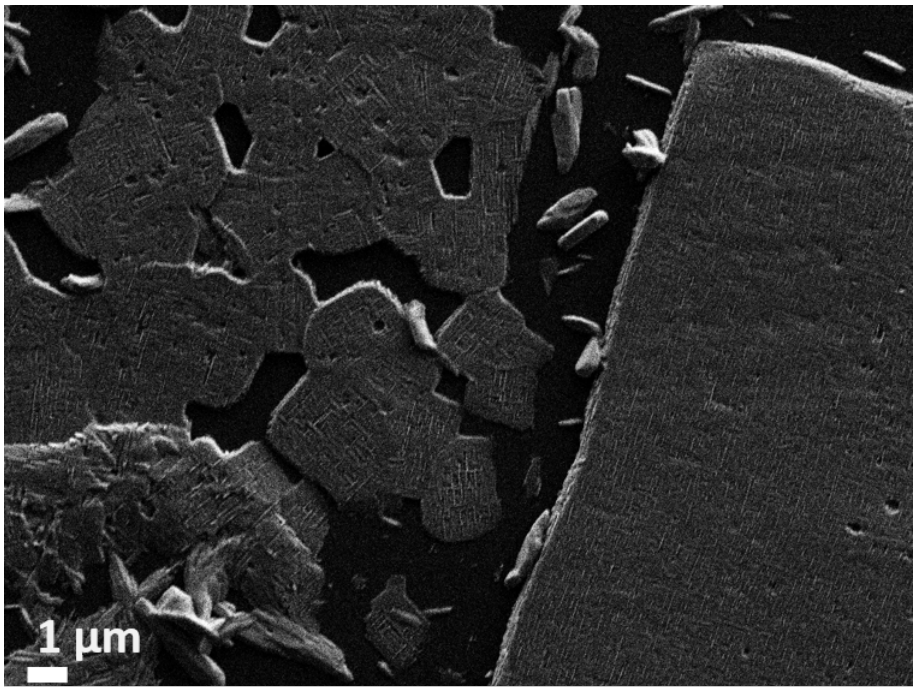

Figure 3.2.: Structural analysis of layered hybrid perovskites. SEM image of $C_{10}PbI_4$ displaying crystalline domains in µm size with a maximum of several tens of µm.

3.2. Structural characterization

In this thesis, nanocrystals were investigated regarding their composition and size. Analyses of structures on nanoscale is challenging as conventional light microscopes cannot resolve these structures. The resolution limit for microscopes is given by Abbe's law: [94]

$$d \geq \frac{\lambda}{NA_{objective}}, \tag{3.2}$$

where d is the minimal resolvable spacing, λ is the wavelength, and $NA_{objective}$ is the numerical aperture of the lens of the microscope. For an optical microscope the shortest resolvable distance is about $\lambda/2$. For green light this is equal to about 250 nm. There are several approaches to resolve structures on smaller scales. Two of them are presented in the following. Both techniques use sources that generate light with wavelengths of several orders of magnitude below the wavelength of visible light. The first one is X-ray diffraction, using high-energetic X-ray, and the second one is electron microscopy, relying on accelerated electrons.

3.2.1. X-ray diffraction

X-ray diffraction (XRD) is a non-invasive structural analysis method using X-rays. X-rays were first discovered by Wilhelm C. Röntgen in 1895. [95] Max von Laue discovered that these X-rays are diffracted by crystals and was awarded the Nobel Prize in 1914 for this discovery. [96]

XRD is a well established technique for more than a century by now. It relies on the fact that X-rays, like other electromagnetic waves, are diffracted by a grating. Since the wavelengths of X-rays are approximately the same size as the lattice constant of a crystal, the technique allows to analyze ordered or crystalline structures. A disadvantage of XRD is that it is a indirect measurement technique that relies on models. Often, other imaging methods, such as electron microscopy are used as supporting measurements to understand the XRD data in detail. The crystal properties that can be determined include the crystal structure, the dimensionality, and chemical bonds.

For this thesis, three different XRD setups were used. These setups have different resolution limits that are described below. For the data analysis, different models were used that are described along with the measurement technique.

Theta - 2 Theta X-ray diffraction

For the layered hybrid perovskites, X-ray diffraction (XRD) analyses were performed at room temperature with a *Bruker D8 Advance A25* diffractometer provided by the chair

of Prof. Dr. Thomas Bein. During the measurement, the source and detector are moved in a circle around the sample and their relative position is recorded in 2θ. The method is also called $\theta - 2\theta$ XRD. The samples were scanned over the angular range of $2\theta = 2°$ to $2\theta = 60°$ with a step size of 0.02°. The radiation used was Cu-Kα ($\lambda = 1.52\,$Å). The database *Mercury*[97] with entries from references[85,86,87] was used for data analysis.

Bragg's law

From the measured 2θ angle of the XRD measurements, the Bragg distance d_{Bragg} was calculated by using Bragg's equation:[98]

$$n\,\lambda = 2\,d_{Bragg}\,sin\theta\,, \tag{3.3}$$

where n is an integer number, λ is the wavelength of the source, d_{Bragg} is the distance between two lattice planes, and θ is the incident and scattered angle (see figure 3.3).

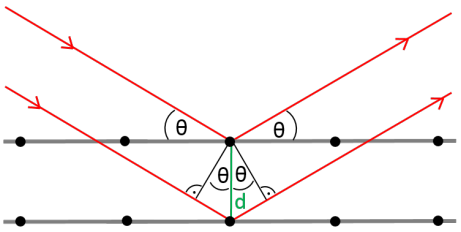

Figure 3.3.: Bragg's distance. The path difference between two incident and scattered waves is $2\,d_{Bragg}\,sin\theta$. Bragg's equation (equation 3.3) gives the relation between interplanar distance d_{Bragg} and diffraction angle θ.

X-ray powder diffraction

For the analysis of perovskite $MAPbBr_3$ nanoplatelets, X-ray powder diffraction (XRD) measurements were performed. To obtain powders the solvent of the perovskite suspensions was evaporated in a rotary evaporator.

For XRD measurements of single crystals or polycrystalline films the diffraction signal depends on the crystal orientation in respect to the source and detector. In contrast, XRD measurements of crystalline powder with isotropic orientation allow in principle to obtain reflections of all reflective planes if not hindered by the resolution limit. This is due to the averaging over all crystal orientations in the powder. The used setup has a microfocus X-ray source from *Xenocs* with Mo target ($\lambda = 0.71\,$Å). The divergence of the collimated beam is less than 0.2 mrad in vertical and horizontal direction. The beam diameter at the sample is around 1 mm and the flux is typically $3.3 \cdot 10^6$ photons/s. The signal is detected in a two-dimensional plane. The detector (*Pilatus 100 k*, 1 mm sensor, *Dectris*)

has a quantum efficiency of 76 %. The recorded powder rings were transformed to 2θ angles via radial integration with the *Igor Pro* software plug-in *Nika*.[99] The samples were measured over an angular range of $2\theta = 2°$ to $2\theta = 34°$. All powder XRD measurements were done by Dr. Stefan Fischer in the group of PD Dr. Bert Nickel.

Crystallite size analysis

From the XRD peak width, the crystallite size can be extracted for nanocrystals smaller than 100 nm - 200 nm.[100] In general, neglecting instrument broadening, a perfect crystal consisting of an infinite number of perfectly periodic planes would result in a delta peak. However, in real crystals crystal imperfections such as lattice strain, faulting or small size broaden the peaks. Neglecting strain and faulting, the peak broadening gives a simple method to determine the crystallite size (assuming a perfect instrument resolution). A common description of this broadening effect is the Scherrer equation:[100]

$$B_{hkl}\,(2\theta) = \frac{0.94\,\lambda}{L_{hkl}\;cos(\theta)}\,, \tag{3.4}$$

where B_{hkl} is the full width at half maximum (FWHM) in radians, extracted from the XRD spectrum. The factor 0.94 is an empirical factor, L_{hkl} is the crystallite size, λ the wavelength of the used source and 2θ the angle between diffracted and incident beam.

Energy dispersive X-ray spectroscopy

Energy dispersive X-ray (EDX) measurements were carried out for elemental analysis of the $MAPbBr_3$ nanocrystals. The used instrument was an HRTEM *Titan 80-300* with a Si(Li) detector. For an EDX measurement the sample is excited by the X-ray source. The recorded emission spectra are characteristic for each element and thus allow to determine the elemental composition of the sample. The samples for EDX were prepared by drop casting about 20 µl of the sample on a copper grid covered with a holey carbon film. All EDX measurements for this thesis were carried out by Dr. Markus Döblinger at the chair of Prof. Dr. Thomas Bein.

3.2.2. Electron microscopes

Scanning electron microscope

A scanning electron microscope (SEM) was used to analyze the morphology of the nanocrystals synthesized in this work. A focused electron beam scans the substrate surface where electrons are scattered depending on the sample surface, shape and composition. The

beam is generated with an electron gun and a chosen acceleration voltage. Ring coils serve as magnetic lenses that focus the beam onto the sample. In principle, the image resolution is limited by equation 3.2, that can be formulated as:

$$\lambda_B = \frac{h}{\sqrt{2\,e\,m_0\,V}}, \tag{3.5}$$

with the de Broglie wavelength of the electrons λ_B, the Planck constant h, the elementary charge e and the acceleration voltage V. There are two detectors. The in-lens detector records directly scattered electrons and a secondary electron detector at the side of the sample records secondary electrons. The SEM used for this work is a *Gemini Ultra Plus* field emission scanning electron microscope with a nominal resolution of about 2 nm (*Zeiss*, Germany). The accelerating voltage was 0.5 kV, the working distance 1 mm and the images were taken with the in-lens detector. For the SEM measurement, 20 µl of the samples were drop casted on a copper grid with a holey carbon grid.

Transmission electron microscope

Transmission electron microscopy (TEM) uses an accelerated and focused electron beam that is transmitted through the sample to form an image and thus uses electron diffraction. High accelerating voltages allow for a high resolution. The transmission through the sample allows to detect small differences in electron transmission.
The geometry of the nanocubes and nanoplatelets was investigated using a *JEOL JEM-1011* TEM provided by the group of Prof. Dr. Joachim Rädler. The TEM was operated at an accelerating voltage of 80-100 kV, allowing for a resolution of 1 nm to 3 nm. Preliminary to the measurements about 20 µl of the diluted sample were drop casted on a copper grid covered with a holey carbon film.

High-resolution transmission electron microscope

High-resolution TEM (HRTEM) is a technique that allows direct imaging of the atomic structure of the sample. This is achieved through very high accelerating voltages and the resulting electron wavelength lies below the atomic separation in solids. The strong atomic scattering factor of electrons allows to detect even weak scattering centers. However, spherical and chromatic aberrations limit the resolution of HRTEM and the k-space resolution of the electron beam is poorer than in XRD.
In this thesis, HRTEM images in TEM mode were recorded with a *Titan 80-300* at an accelerating voltage of 300 kV to distinguish between perovskite nanocrystals and precursor residuals and decomposed nanocrystals. All HRTEM related measurements were performed by Dr. Markus Döblinger and Dr. Andreas Wisnet at the chair of Prof. Dr. Thomas Bein.

3.3. Optical characterization

3.3.1. Absorption spectroscopy

Absorption spectroscopy was conducted at room temperature with a commercially available instrument from *Agilent Technologies, Cary 5000 UV-Vis-NIR*. The two methods that were used are described in the following. The samples were measured in quartz cuvettes.

Linear absorption

The instrument records the difference in intensity of two beams emitted from a xenon lamp with attached monochromator for spectral resolution. One beam passes through the sample. The other beam is unaffected and serves as a reference. The setup thus allows only to record the transmitted light T. It is not possible to distinguish between scattered and absorbed light. Therefore, only diluted solutions of nanoparticles that show little scattering were measured with this setup. The absorption A is calculated using $A = 1 - T$. The measurements were carried out in the range from 300 nm to 800 nm in steps of 0.5 nm.

Integrating sphere

In order to measure absorption spectra of highly scattering materials, such as dispersed nanocrystals or crystalline films, an integration sphere (*Diffuse Reflectance Accessory*) can be mounted to the setup. Then the sample is placed in the center of the highly reflective sphere and the detector is no longer placed in the pathway of the incoming light but at a 90° angle. Thus, the transmitted as well as the scattered light can be detected and the absorption can be recorded. The integration sphere was used to acquire absorption spectra of the highly scattering drop casted films of layered hybrid perovskites.

3.3.2. Photoluminescence spectroscopy

The photoluminescence (PL) spectroscopy and photoluminescence quantum yield measurements (PLQY) were conducted at room temperature with the commercial devices *Horiba, Fluorolog 3* and *Agilent Technologies, Cary Eclipse Fluorescence spectrophotometer (Varian Inc.)*.

For PL measurements the samples were excited by a xenon lamp which was focused through an entrance slit onto the sample. The PL light was detected through the detector's slit at an angle of 90° to the incoming light. The slit width determines the resolution of the

measurement. Here, the slit widths were chosen 1 nm for the entrance slit as well as for the detector slit. For the measurements on the colloidal perovskite nanocrystals in quartz cuvettes an excitation wavelength of 350 nm was used and the measurements were carried out over a spectral range from 380 nm to 650 nm in steps of 0.5 nm. For the crystalline films of layered hybrid perovskites on glass substrates an excitation wavelength of 400 nm was used. The measurements were carried out over a spectral range from 420 nm to 600 nm. The PLQY measurements were carried out in an integrating sphere *K-Sphere Petite* from *Horiba* that can be installed at the PL setup. The sample was placed in the center of the sphere and excited through a small slit while the signal was collected through a second slit. Two spectra were acquired: One of the sample and one of reference, e.g. a clean glass substrate or a cuvette with pure solvent. The difference in the excitation peak area of both measurements is proportional to the absorbed intensity and to the number of absorbed photons N_{abs} while the area gain at the PL peak is proportional to the number of emitted photons N_{emission}. The PLQY Φ_{PL} can be calculated as $\Phi_{PL} = \frac{N_{\text{emission}}}{N_{\text{abs}}}$.

3.3.3. Streak camera: time-resolved photoluminescence spectroscopy

For time-resolved PL measurements a streak camera *Hamamatsu C5680 with synchroscan unit M5675* was used. The sample was excited by a pulsed diode Laser *PDL 800B-405 nm* from *Pico Quant*. The excitation wavelength was 405 nm with a power density per pulse of 1.5 µJ cm^{-2}. The repetition rate was 750 kHz, corresponding to approximately 1.3 µs between two pulses. The resolution limit of the diode laser and sweep unit is about 300 ps. The working principle of the streak camera is sketched in figure 3.4. The sample is excited by the laser pulse. The emitted photons are time delayed in respect to the pulse and to each other depending on when they were emitted by the sample. Before entering the actual streak unit, the photons are spectrally resolved with a spectrometer. In the streak

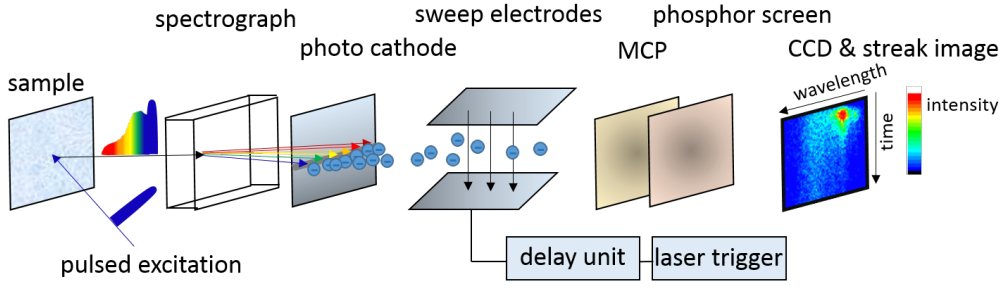

Figure 3.4.: Schematic illustration of the geometry and working principle of a streak camera. Photons excited by a short laser pulse and spectrally resolved by a spectrometer pass through a deflection unit that allows time-resolved detection. Details of the working principle are provided in the main text.

unit, the incoming photons are converted into electrons by a photo cathode. Subsequently, the electrons are accelerated and pass a parallel capacitor. Due to linearly changing voltage at the capacitor, that is synchronized with the laser pulse, the electrons are deflected depending on the instant of time they enter the capacitor. That is, electrons entering the capacitor first are less deflected than those entering the capacitor later. Thus, a streak image of the decay dynamics is created where the time-dependent intensity is converted into a spatial resolved intensity. A micro channel plate (MCP) amplifies the signal before a phosphor screen reconverts the electrons into photons that are subsequently detected by a CCD camera. In the resulting streak image, the delay times of incoming photons are resolved in y-direction of the resulting streak image. The x-axis records the wavelength and the signal intensity. It is color coded from black (no signal) and blue (low signal) to red (high intensity) and white (over-saturated). These spectra can be fitted and decay times, characteristic of the samples, can be extracted.

3.3.4. Setup for temperature-dependent time-correlated single photon counting

Temperature-dependent steady-state PL and time-correlated single-photon counting (TCSPC) were measured with a setup schematically depicted in figure 3.5. The sample was spin coated on a sapphire substrate and glued into the vacuum chamber of the cryostat with conductive silver lacquer from *Busch*. The flow cryostat from *CryoVac* was operated with a control unit that adjusts valves and the heating wires. For thermal isolation the vacuum chamber was operated at a pressure of 10^{-5} to 10^{-6} mbar achieved with a *TurboDrag pump* (*Pfeiffer Vacuum, TMH071P*). Liquid helium was pumped from a liquid helium storage dewar through the cryostat with a diaphragm vacuum pump (*Vacuubrand, type ME 4 NT*). The entire cryostat was placed on a stage that allows the sample to move in all spatial directions.
The spectrograph consists of a monochromator (*Acton SpectraPro SP2300*) and a charge-coupled device (CCD) as light sensor *PIXIS 400 eXcelon* from *Princeton Instruments*. It is operated with the software *LightField*. The CCD saturates at 65 000 counts. In the monochromator the light beam is parallelized with a concave mirror. In imaging mode it is then directed to a mirror whereas in spectroscopy mode it is directed on a reflection grid instead. A second concave mirror focuses the light onto the CCD where the intensity in a specific wavelength range is measured and sent to a computer (PC).
As light source a white light laser *(NKT Photonics, SuperK Extreme, EXR-20*) was used. With the *SuperK Extend-UV unit* a single excitation wavelength in the region between 330 nm and 480 nm can be selected from the laser continuum. For this work an excitation wavelength of 400 nm was used. The light beam was focused on the sample with a

planoconvex lens ($f = 75\,\mathrm{mm}$). The laser spot size was roughly $1\,\mathrm{mm}^2$ and a repetition rate of 77.9 MHz at 100 % beam intensity was used. The resolution limit of the setup is about 1 ns. Faster decay times cannot be resolved. The power was 6.5 µW, thus the excitation density was $20\,\mathrm{nJ\,cm^{-2}}$. The fluorescence light from the sample was collected with a long working distance objective *SLCPLFL 40x/0.55* from *Olympus* and directed in a parallel way to the above mentioned biconvex lens to record the spectra as described before.

The setup offers the possibility to record the PL decay using a second exit of the monochromator where the light is focused onto a single photon counting module from *Excelitas* which enables TCSPC. For data evaluation, including background subtraction, change from a wavelength axis to an energy axis, extraction of peak positions and FWHM, a software application was programmed with *C++* and *Qt*.

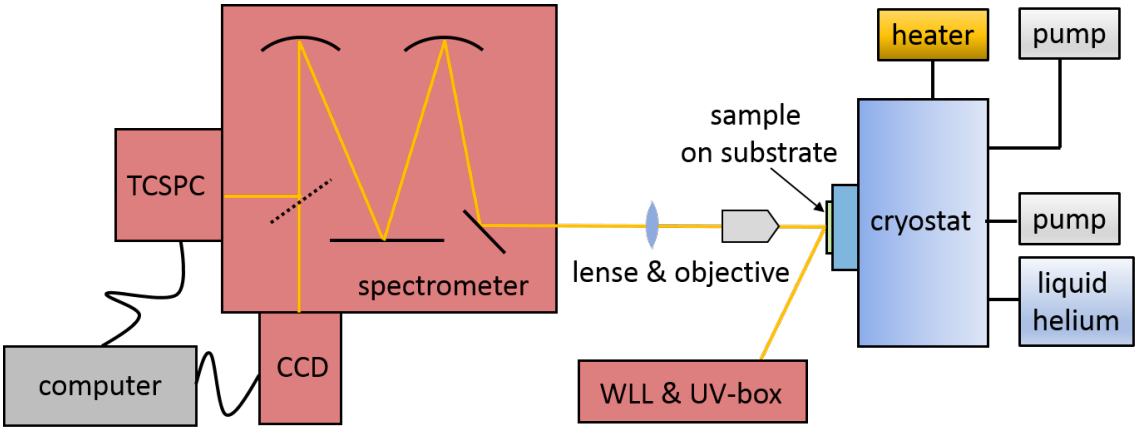

Figure 3.5.: Schematic illustration of the setup for temperature-dependent PL and lifetime measurements. The working principle is described in the main text. TCSPC: time correlated single photon counting, CCD: charge-coupled device (light sensor), WLL: white light laser, UV-box: spectral extension unit for deep-UV.

4. Quantum size effects in perovskite nanoplatelets

Organic-inorganic lead halide perovskites have been known for several decades.[40,101,102,103] Yet, their huge potential for photovoltaic applications as well as for light-emitting devices was only discovered only in recent years.[104,105] Specifically tailored perovskite nanocrystals offer further possibilities to tune the material's properties through size-dependent effects. One possible structure is the two-dimensional nanoplatelet. In comparison to the bulk counterpart, nanoplatelets display increased exciton binding energies, reduced fluorescence lifetimes, and enhanced absorption cross sections.[106,107] These are some of the properties which render nanoplatelets interesting for optoelectronic applications. Although two-dimensional layered hybrid perovskites, comprising macrocrystals, have been known since the late 1980s,[23,82,83] colloidal perovskite crystals on the nanoscale and of lower dimensionality were achieved only in 2014 by the group of Pérez-Prieto[18]. In parallel to the work presented here, several studies on perovskite nanocrystal were published by other groups.[93,108,109,110,111,112] In this chapter, new and systematic variation of the ligand concentration the nanocrystal synthesis is presented. This enables the fabrication of colloidal perovskite nanoplatelets of varying thickness down to a single monolayer. This allows the following thickness-dependent investigations of quantum size effects in this chapter.

4.1. Synthesis

In order to obtain nanocrystals, besides the small organic A-site cation (methylammonium, MA) that fits into the 3D crystal structure of $MAPbBr_3$, an additional large cation (octylammonium, OA) was added. Both cations have the same ammonium functional group, but OA possesses an alkyl moiety of eight C-atoms instead of only one. Therefore OA cannot be incorporated into the 3D crystal structure but binds to the perovskite with the ammonium functional group while the alkyl chain points outwards. Thus OA acts as a ligand, preventing further crystal growth and ensuring colloidal stability. While earlier studies on 2D perovskite had mainly only used a large cation yielding multiple stacks of monolayer perovskite on the macroscale, the use of short and long cations yields nanocrystals of varying size and thickness.[18,23] As described in detail in subsection 3.1.1, the synthesis is based on a precipitation of the target compound. Initially, the perovskite precursor solutions were mixed in due proportions and diluted in a polar solvent. The perovskite crystals precipitate once dropped into a solution of antisolvent for the target compound. This antisolvent is in fact a good solvent for the target's ligands and can therefore ensure colloidal stability of the nanoplatelets. However, the impact of the ligand on the perovskite's geometry and optical properties had not been fully understood. The variation in ratio of long cation to overall organic cation content OA : (OA+MA) presented here, gives the opportunity to probe the role of the ligand.
The synthesis was carried out with varying OA : (OA+MA) content. The OA fractions were varied in steps of 20 % from 0 % to 60 % and in steps of 10 % from 60 % to 100 %. The samples were labeled according to the OA fraction during the synthesis. This fraction might differ from the final content of OA in the solution due to the washing cycles. Under ambient light the samples have a yellowish color, typical of the bromide perovskites.[9,113] The opacity of the samples decreases with increasing OA content as the photograph in figure 4.1 shows.

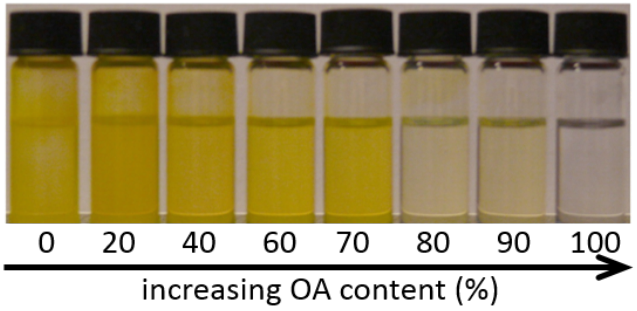

Figure 4.1.: Photograph of perovskite suspensions. The color of the perovskite suspensions under ambient light changes with increasing octylammonium (OA) content from yellow to transparent.

4.2. The ligands' influence on size and shape of perovskite nanocrystals

To investigate the geometry of the nanocrystals, SEM and TEM images were recorded. Figures 4.2 a and 4.2 b show SEM and TEM images of the 20 % OA sample. The SEM image shows clusters of well defined nanocubes with lateral dimensions of several tens of nanometers (sketched in figure 4.2 c). These structures appear rectangular and dark when measured with TEM. Some areas appear almost black and their contours are blurred while some areas are grey with very well defined rectangular structures. The lateral dimensions of the cubic structures range from about 20 nm to 200 nm. The high contrast of the TEM picture stems from low electron beam transmission and indicates a certain thickness of the structures. Therefore, the observed structures are not thin and platelet-like but rather nanocubes. Areas appearing almost dark might stem from stacks of nanocubes while grey areas might show single nanocubes. On the contrary, SEM and TEM measurements of the 80 % OA and 60 % OA samples reveal thin platelet-like structures (figures 4.3 a and 4.3 b). The SEM image shows nanoplatelets of different thicknesses. Some are almost detached from the rest but most platelets lie unordered on top of each other. The lateral dimensions of the platelets are of about 100 nm to 150 nm regardless of their thickness. The thicknesses, however, account for only a few nanometers and display a wide range of values.

The TEM image shows rectangular structures orderlessly stacked one upon another. Areas where most of the electron beam is transmitted appear light grey and offer low contrast to the grey background. These areas contain very few or single platelets. Areas that transmit less of the incident electron beam appear dark and contain stacks of multiple platelets.

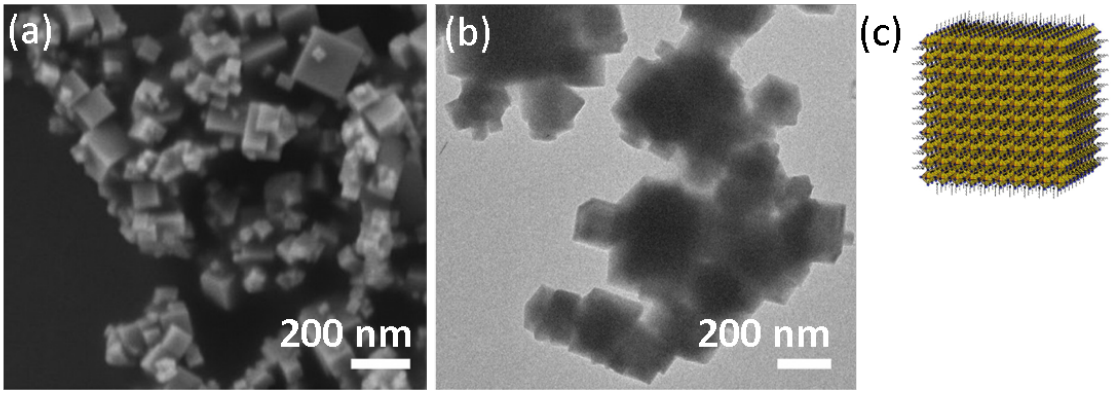

Figure 4.2.: SEM image, TEM image, and sketch of $MAPbBr_3$ nanocubes. (a) SEM and (b) TEM image of nanostructures found in the 20 % OA sample showing clusters of nanocubes. (c) Sketch of a perovskite nanocube surrounded by ligand chains sticking outwards.

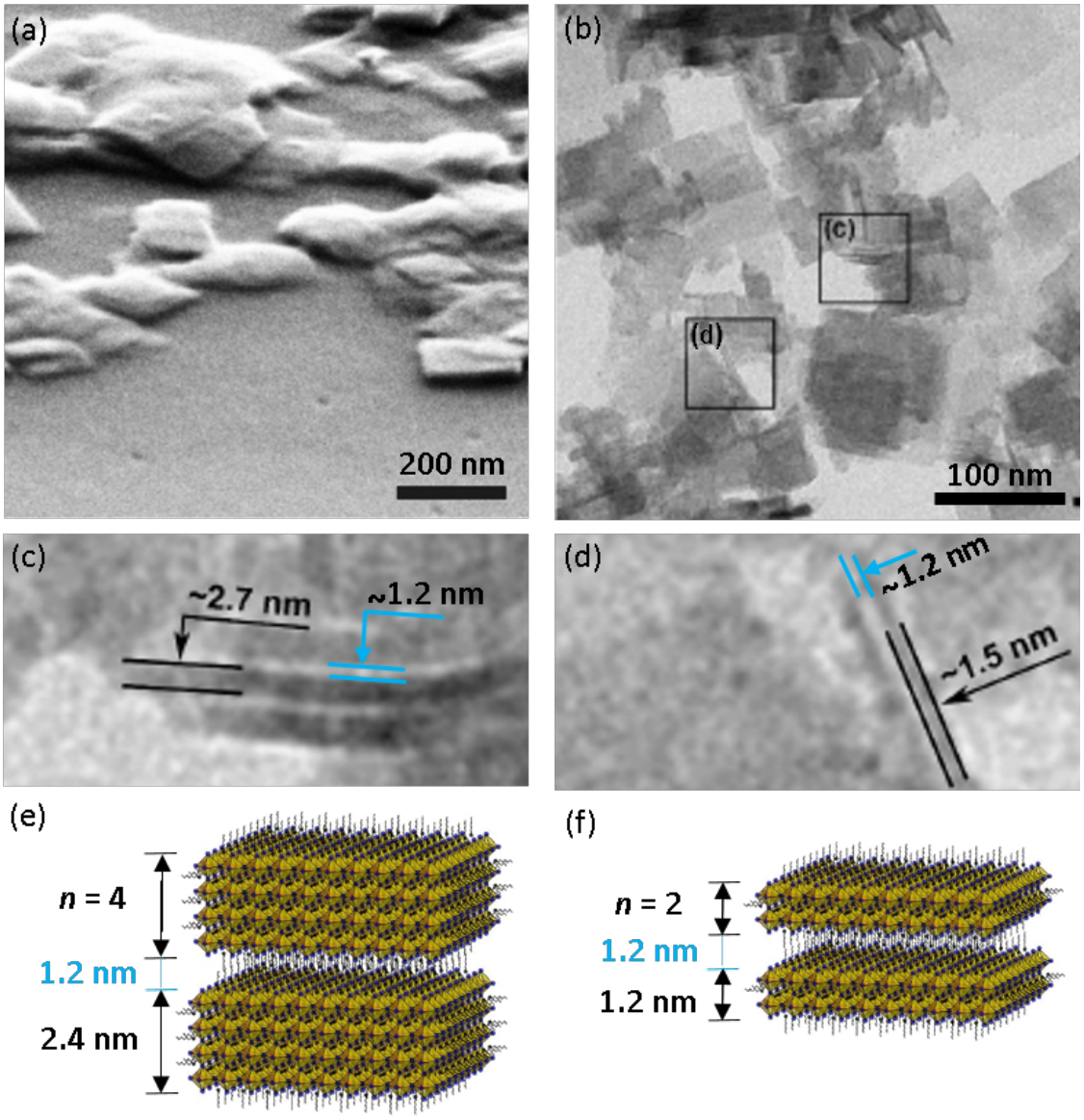

Figure 4.3.: SEM image, TEM images, and sketch of $MAPbBr_3$ nanocubes. (a) SEM image of nanostructures found in the 80 % OA sample showing stacks of nanoplatelets. (b) TEM image of a drop casted sample of 60 % OA containing nanoplatelets. The dark contrast indicates that the nanoplatelets stack together. Some platelets appear to be standing on their sides, allowing an estimate of their thickness (c-d). The distance between neighboring platelets is estimated from the image. It comprises of intercalated organic ligand giving low contrast in TEM (indicated by blue marks). (e) Sketch of two nanoplatelets with $n = 4$ unit cells thickness stacked on top of each other with intercalated ligand chains in between them. The height of one unit cell or layer accounts for 6 Å. (f) Two nanoplatelets of $n = 2$ unit cells thickness stacked on top of each other.

The lateral dimensions of the platelets are about 100 nm but the varying image contrast especially in areas of single flakes indicates that their thicknesses differ from one another. Figures 4.3 c and 4.3 d show parts of the TEM image with a higher magnification. Both

pictures reveal rod-like structures that form very regular structures of alternating dark and light grey areas. The dark areas display widths of about 2.7 nm and 1.5 nm in figures 4.3 c and 4.3 d, respectively. The widths of the light grey areas, in contrast, account in both pictures for about 1.2 nm. Considering the dark color of the rod-like structures, these cannot stem from nanorods of only 2-3 nm cross section but are nanoplatelets standing on their sides. This allows the assignment of the measured width of the dark area to the thickness of the thinnest nanoplatelets found in the 60 % OA sample (figures 4.3 c, d). Knowing that the nanoplatelets comprise of an integer number of unit cells with an approximate height of 6 Å,[114] the measured thickness of 2.7 nm is attributed to nanoplatelets of $n = 4$ or $n = 5$ layers of unit cells in height as sketched in figure 4.3 e. The value of 1.5 nm is attributed to nanoplatelets of $n = 2$ layers of unit cells sketched in figure 4.3 f. The nanoplatelets are surrounded by outwards sticking organic ligand chains, comprising of hydrogen and carbon atoms. These two elements are known to give low contrast when measured with TEM and thus the ligand was expected to be hardly visible in the TEM images as observed. The length of one ligand chain accounts for about 1 nm[114] and therefore the region of low contrast between the nanoplatelets is too narrow for non-intercalating ligands. The OA ligands however are known to intercalate and form stacks of about 1.2 nm[114] matching the observed distance between the platelets. Therefore, it is concluded that intercalating ligands of two neighboring platelets separate the platelets. This confirms that the platelets indeed stack. This observation will play a role when analyzing the material's optical properties in section 4.5.
Figure 4.7 b in section 4.4 shows TEM images of all samples. With increasing OA content the image contrast decreases gradually. This reduction is due to higher electron transmittance in thinner structures. The depicted nanostructures undergo a clear change in morphology from nanocubes to nanoplatelets of decreasing thicknesses.

To confirm that the synthesis product is actual perovskite, X-Ray powder diffraction (XRD) measurements were carried out at room temperature. The prevalent peaks in the XRD spectra of the samples 0 % OA to 80 % OA are attributed to lattice planes of a cubic crystal structure with the space group $Pm\bar{3}m$ and with a lattice constant of 5.93 Å, characteristic of the bulk $MAPbBr_3$ perovskite at room temperature (figure 4.4).[18,40,115,116,117,118] Apart from the perovskite peaks, the 100 % OA sample shows multiple other diffraction peaks. Comparison of these peaks to the peaks of pure $PbBr_2$ shows that the 100 % OA sample contains additional pure precursor $PbBr_2$. Altogether, the positions of the XRD peaks confirm that perovskites were formed in all the suspensions. As described in subsection 3.2.1 the Scherrer approximation allows an estimate of the crystallite sizes from the peaks' full width at half maximum (FWHM). These and further phenomena are discussed in the following for a more detailed understanding of the spectra.

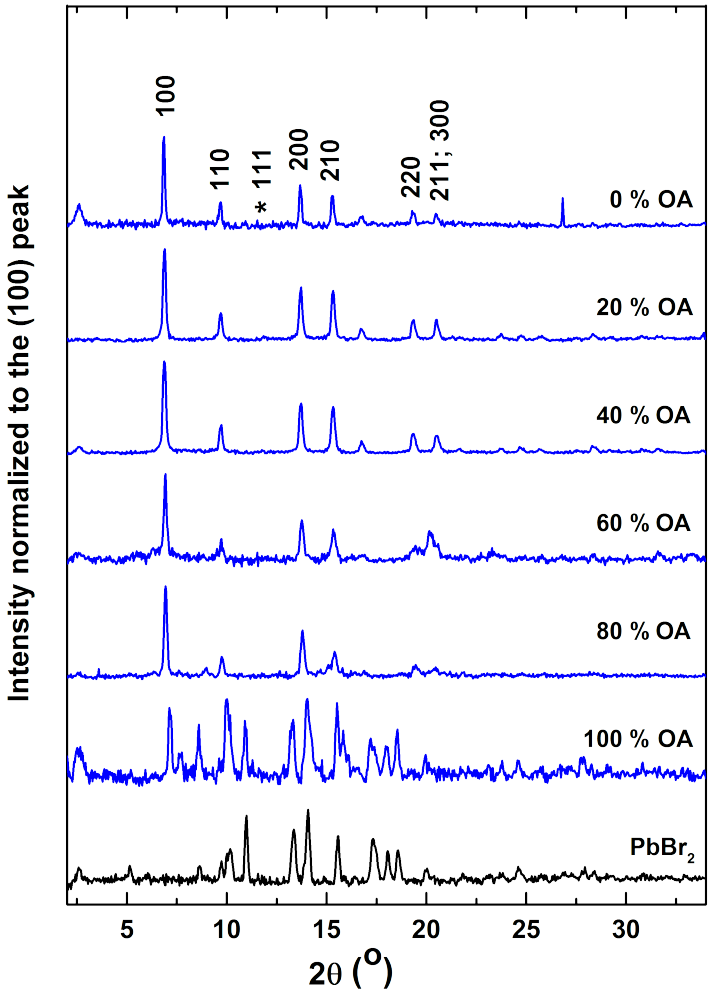

Figure 4.4.: XRD scattering spectra of perovskite powders with varying OA content and of pure $PbBr_2$. The Miller indices (hkl) are indicated. The peaks stem from perovskite and show a relative decrease in intensity with increasing OA content. All spectra are normalized to the (100) peak. The position of the (111) reflection is marked with an asterisk as its intensity is too low to be resolved.

In general, very large, defect-free crystals cause sharp reflection peaks (δ-peaks) in the XRD spectra (assuming a perfect instrument resolution).[100] For very small crystals, however, the reflection peaks broaden and decrease in intensity.[100] This peak broadening due to small particle size can be described with the Scherrer approximation and the size of a well ordered crystal can be determined from the peak width (equation 3.4). The investigated $MAPbBr_3$ nanoplatelets have a finite crystal size. Hence, a relative peak broadening and a loss of intensity with decreasing thickness of the nanoplatelets could be expected. Yet, as illustrated in figure A.1 a in the appendix, the nanoplatelets' size decreases only

in one dimension whereas the other two dimensions are still relatively large. Furthermore, the nanoplatelets are in a cubic crystal configuration with the space group $Pm\bar{3}m$ at room temperature. For this anisotropic crystal shape and cubic crystal configuration the Scherrer approximation is not directly applicable for the following reasons.

As a result of the cubic crystal configuration, the (100) peak has a multiplicity of six (figure A.1 b). All 6 planes provoke scattering peaks at the same spectral position. Of the 6 planes, 4 scatter in the plane of the platelets while only 2 get diffracted out-of-plane. Due to the anisotropic crystal shape, only the diffractions out-of plane are affected by the thinning of the structures, while the crystallite size in the remaining 4 directions is too big to cause a resolvable peak broadening. As the diffracted power, that is the integrated intensity of the diffraction peak A, is proportional to the number N of scattering planes squared ($A \propto N^2$) the contributions of the small dimensions of the platelets to the diffraction peak is negligible compared to the non-broadening contributions. Consequently, the observed spectral superposition of in-plane and out-of-plane directions is an intense and narrow peak. As the platelets are arbitrarily orientated in the sample this effect cannot be avoided by a separate analysis of different sectors of the 2D diffraction patterns. To still investigate the peak broadening effect, a plane that yields only scattering in out-of-plane direction would be needed. A peak fulfilling this requirement is the peak of the (111) reflection. This peak possesses a multiplicity of 8 and none of the contributing planes scatters in pure in-plane direction (figure A.1 c). Yet, the signal is too weak to be resolved by the instrument and thus the broadening cannot be investigated.

The relative peak intensities are further analyzed. The (200) and (210) peaks both show reasonably high intensities in the XRD spectra. The (200) peak has a multiplicity of 6, with 2 of its contributors scattering in out-of-plane direction (figure A.1 d). The (210) peak has a multiplicity of 24 with 16 directions with out-of plane contribution (figure A.1 e). As already mentioned, due to spectral superposition a signal broadening cannot be directly measured for any of these peaks. Yet the out-of-plane diffractions are expected to contribute much less to the peak intensity. Thus, the (200) intensity is expected to be up to 1/3 lower for the platelets than for the cubes. Likewise, the (210) intensity reduces by up to 2/3. One can only give upper limits for the expected reduction in peak intensity, as the samples are polydisperse in size and only the very thin nanoplatelets in the dispersions will cause a peak broadening and weakening. Figure 4.5 shows the peak intensities of the (200) peak and the (210) peak. Note that the spectrum is normalized to the (100) peak, that itself undergoes a drop in intensity of up to 1/3. As a result, the curve of the (200) peak almost remains static as expected and the (210) clearly decreases for thinner structures. The trend of decreasing peak intensity thus can be observed in the spectra for the (200) and (210) peaks, supporting the conclusion drawn from electron microscopy above, that the structures grow thinner with increasing OA concentration.

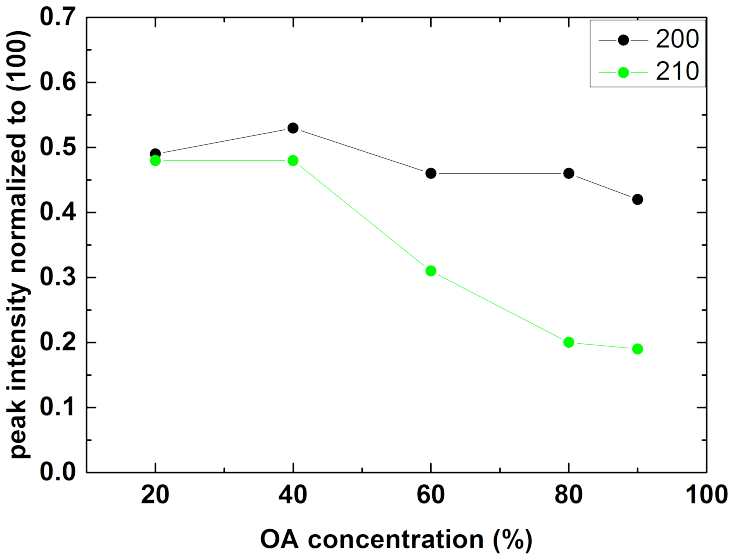

Figure 4.5.: Development of relative diffraction peak intensities with increasing OA concentration. The (200) peak has a multiplicity of 6 (compare also to appendix figure A.1). 2 planes give reflections with out-of plane contribution. Therefore the intensity of the (200) peak should drop by up to 1/3 for thinner structures. As the spectrum is normalized to the (100) peak, undergoing a drop in intensity of up to 1/3 as well, the (200) peak almost remains static. The (210) peak has a multiplicity of 24, 16 with out-of plane contribution, therefore the intensity drops by up to 2/3 of its initial intensity.

4.3. Decomposition of nanoplatelets through electron beam exposure

In some of the acquired TEM images circular structures, in the size range of nanometers to tens of nanometers can be observed along with the nanoplatelet structures (figure 4.6 a). These circular structures resemble spherical nanoparticles as reported in previous studies.[18,93,109,112] They are often accompanied by a rectangular background or seem to align in a rectangular pattern whenever there is no background to be seen. During the measurements, some of the nanoplatelets were observed to transform first into rectangular structures with nanoparticles and subsequently into only nanoparticles. These nanoparticles shrank in size and finally vanished completely under continuous exposure to the electron beam. Previous studies have also reported this effect, but the nature of the particles was unknown.[109,112] High-resolution TEM (HRTEM) reveal these structures to be highly crystalline (figures 4.6 b and 4.6 c). A Fast Fourier Transformation (FFT) was applied (figure 4.6 d). From the observed fringes the lattice parameters and thus the material can be determined. The measurement was along the [-110] zone axis. Fringes

are observed at 2.9 Å and $\Theta = 70°$ and at 2.5 Å and $\Theta = 55°$. These can be attributed to (111) and (11-1) lattice planes of pure lead provoking fringes at 2.86 Å and $\Theta = 70.5°$ and the (00-2) plane with fringes at 2.48 Å and $\Theta = 54.7°$, respectively.

To further determine the nature of the quasi-particles, energy-dispersive X-ray spectroscopy (EDX) measurements were carried out. Many of the particles show a molar content of Pb : Br between 1 : 1.3 and 1 : 0.75 (appendix figure A.2). These values differ from the ratio expected for pure perovskite nanocubes (1 : 3), pure perovskite nanoplatelets consisting of a monolayer (1 : 4) or pure $PbBr_2$ (1 : 2). Therefore, these nanostructures are most likely not perovskite but are rather composed of a mixture of $PbBr_2$, pure Pb, and possibly other phases. In comparison, when EDX measurements were carried out on thin rectangular structures, a ratio of approximately 1 : 2.8 of Pb : Br was found. This ratio also differs from the value expected for perovskites. However, the measurements were difficult to perform as the transformation of the structure from rectangular platelet to circular structures partially occurred during the measurements. This transformation is most likely a degradation process which can result in an altered ratio of the elements. This supports the finding that the synthesis used here as well as in previous studies [18,93,109,112] generally leads to the formation of 2D perovskite nanoplatelets instead of nanostructures with other dimensionalities.

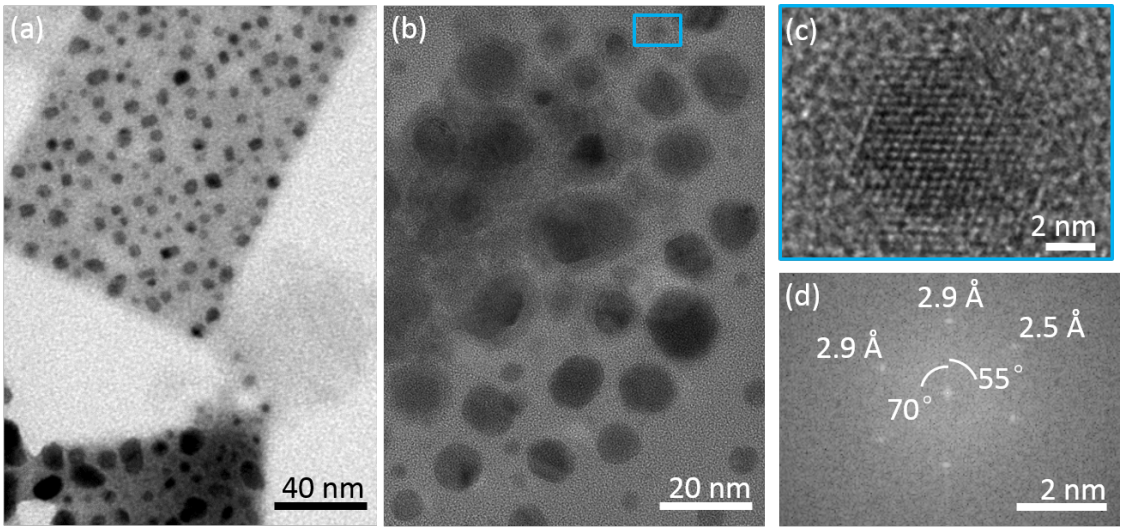

Figure 4.6.: Structural and compositional analysis of circular structures. (a) TEM image of perovskite structures showing circular nanostructures on top of a rectangular nanoplatelet. (b) HRTEM image of circular nanocrystals. (c) High magnification image of one nanocrystal and (d) FFT analysis of its observed lattice planes. The distances and angles match those of metallic lead. The measurement was along the [-110] zone axis. The (111) and (11-1) lattice planes of pure lead will provoke fringes at 2.86 Å and $\Theta = 70.5°$ and the (00-2) plane at 2.48 Å and $\Theta = 54.7°$ which is in good agreement with the observed fringes.

4.4. Thickness-dependence of the quantum size effect

In this section the absorption and emission spectra of the nanocrystals are presented and discussed regarding the size and shape of the structures. As already discussed in section 4.2, the samples contain nanocubes and nanoplatelets of varying thickness as sketched in figure 4.7 a. Figure 4.7 b recaptures these findings. It displays TEM pictures of all samples. The image contrast of the rectangular structures and therefore the nanocrystal thickness decreases from samples with low OA content to samples with high OA content. Under illumination with UV-light, the color of the perovskite suspensions gradually changes from bright green for 0 % OA and 20 % OA to turquoise for samples with higher OA content and finally to dark blue/violet for 100 % OA (figure 4.7 c).

Figure 4.7 d displays the photoluminescence (PL) and absorption spectra for all samples. The emission peaks of the samples up to 60 % OA show a symmetrically shaped single emission peak with maxima between 517 nm and 519 nm. The emission peak of 60 % OA is located at 506 nm and has an asymmetric shoulder at higher energies. The following samples 70 % OA and 80 % OA clearly show multiple peaks, whereas the samples 90 % OA and 100 % OA show single, nearly symmetric peaks at 454 nm and 427 nm, respectively. A similar trend can be observed when comparing the absorption spectra of all samples. The samples with low OA content have steep absorption onsets and a bulk-like absorption spectrum with no pronounced peaks. The samples thereafter show a less pronounced absorption onset but multiple peaks in the absorption spectra. Finally, the absorption spectra of 90 % OA and 100 % OA display clear excitonic peaks.

Considering the chemical composition of the 100 % OA and the observed structure in the TEM, it is unlikely that the emission of this sample stems from anything else than from perovskite nanoplatelets of one unit cell in thickness. During the synthesis for the OA 100 % no methylammonium is used and therefore it is not possible that thicker platelets than monolayers form. Using this as a starting point and knowing that the nanoplatelets must be composed of an integer number n of unit cells, the multiple peaks arising in the PL spectra are attributed to nanoplatelets of different thickness. The blue-shift is in accordance with the quantum size effect described in subsection 2.1.2. Thus the observed emission peaks at 427 nm, 454 nm, 469 nm, 482 nm, and 490 nm, that can be clearly distinguished in the PL curves, are assigned to nanoplatelets of thicknesses of n = 1, 2, 3, 4, and 5 times the unit cell, respectively. This assignment is in agreement with previous reports on the material.[114,119,120] The observed peaks in the absorption spectra are attributed to the respective exciton peaks of nanoplatelets of certain thicknesses. Model calculations supporting this conclusion are subject of the next section.

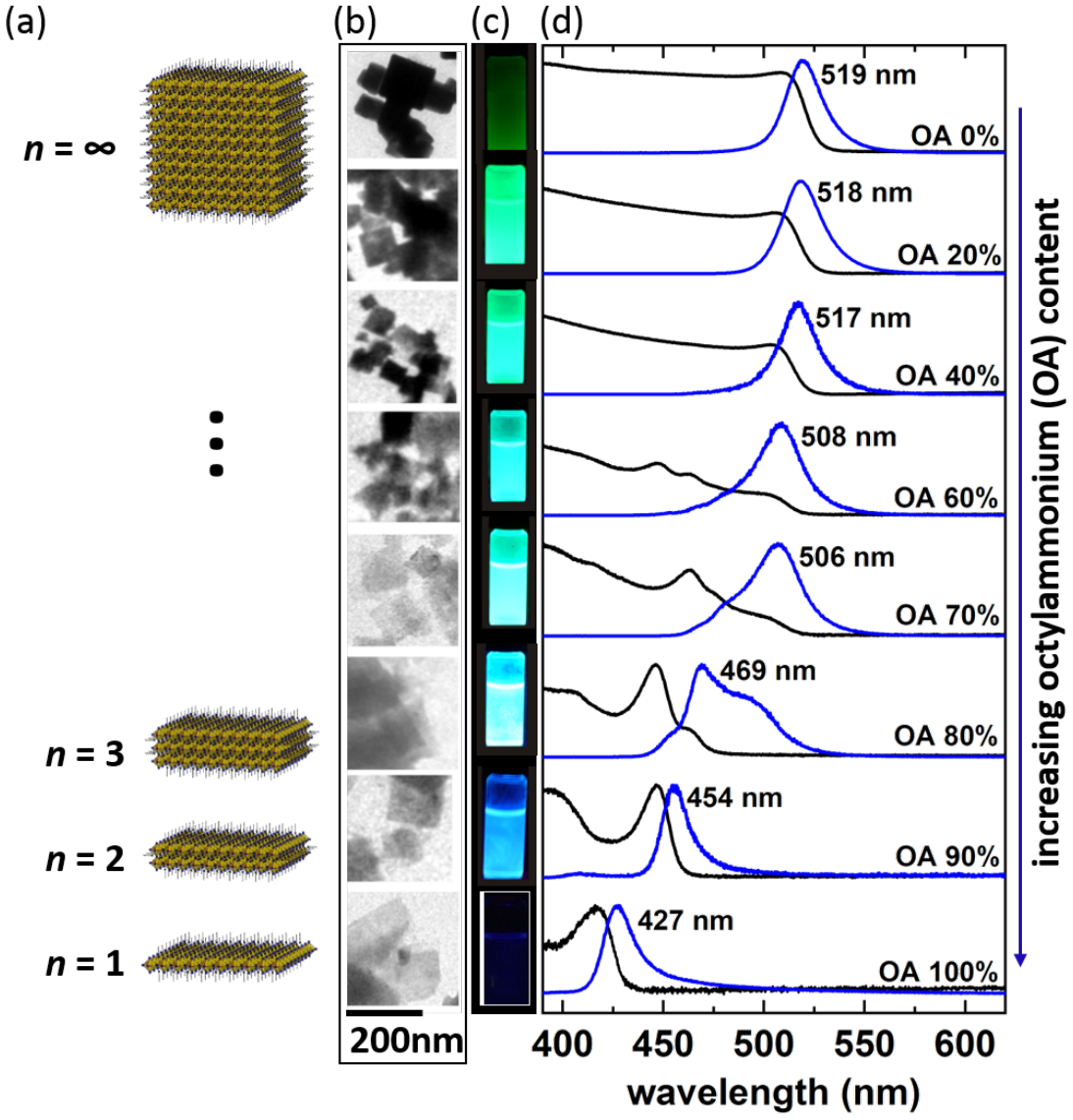

Figure 4.7.: TEM images, photographs under UV-light, absorption and PL spectra of the nanocrystals found in the perovskite suspensions. (a) Schematic drawings of nanocubes and nanoplatelets. (b) The image contrast in TEM pictures and therefore the nanocrystal thickness decreases from samples of low OA content to samples of high OA content. (c) Photographs of the perovskite suspensions under UV light. (d) PL and UV-vis spectra of perovskite films prepared from the suspensions. With thinner structures the PL emission undergoes a blue-shift of more than 90 nm due to quantum size effects.

4.5. Screening effects and enhanced exciton binding energies

Here, the assignment of experimentally found PL emission energies to nanoplatelets of varying thickness in multiples of unit cells n with $n = 1$, to 5 will be quantitatively modeled. Using the thickness of a single layer of 6 Å [114] the PL emission energies from the perovskites are plotted versus their thickness (figure 4.8 e). When calculating quantum confinement in semiconductors, in general an effective mass approximation is used (see subsection 2.1.2). For these calculations, depending on the thickness of the structure, regimes of weak and strong confinement are treated individually. The exciton Bohr radius of bulk $MAPbBr_3$ perovskite is calculated as 1.36 nm (see formula 2.17 and calculation in appendix section A.4), which is slightly more than the height of two unit cells. Therefore, the cases of $n = 1$ and $n = 2$ are considered to be strongly confined in contrast to structures with $n \geq 3$, which are weakly confined.

In a first approach to model the bandgap energies, the nanoplatelets are assumed to be a quantum well with infinite barriers as sketched in figure 4.8 a. The resulting energies are higher than the measured energy values (blue curve, figure 4.8 e).The model oversimplifies the fact that the nanoplatelets are surrounded by a ligand and therefore the confinement is not infinite. As a consequence, the calculated energies are higher than the measured data. In a next step, the model is refined when taking into account that the nanoplatelets are surrounded by ligands sketched in figure 4.8 b. This model yields a curve (green curve, figure 4.8 e) that gives values within the range of error of the experimentally obtained values for $n \geq 4$ but deviates significantly for lower values of n. A further improved model takes into account that the nanoplatelets are not well-separated but actually stack (compare to TEM images in subsection 4.2). Thus, the electron and hole functions extend outside of the platelets and can hybridize with those from neighboring platelets leading to the formation of minibands. Thereby, an infinitely long stack of platelets can be described by the one-band effective mass Kronig-Penney model (figure 4.8 c). Parameters and details can be found in appendix A.5 The resulting curve (orange, figure 4.8 e) reproduces the experimental values well for $n \geq 3$ but overestimates the values for $n = 2$ by 170 meV and $n = 1$ by 600 meV. Considering that the thicknesses for $n \leq 2$ are in the strong quantum confinement regime, an enhanced exciton binding energy has to be taken into account. The exciton binding energy increases for geometrical reasons by a factor of 4 when going from 3D to 2D.[31] In addition, in ultrathin structures the exciton screening is reduced leading to even higher exciton binding energies.[30] In the 3D crystal, the Coulombic interaction between two charges is screened by the surrounding crystal, while this is not the case in the nanoplatelet (see sketch in figure 4.8 d). If the dielectric constant of the crystal's surrounding is smaller than the dielectric constant of the crystal, the dielectric effects will

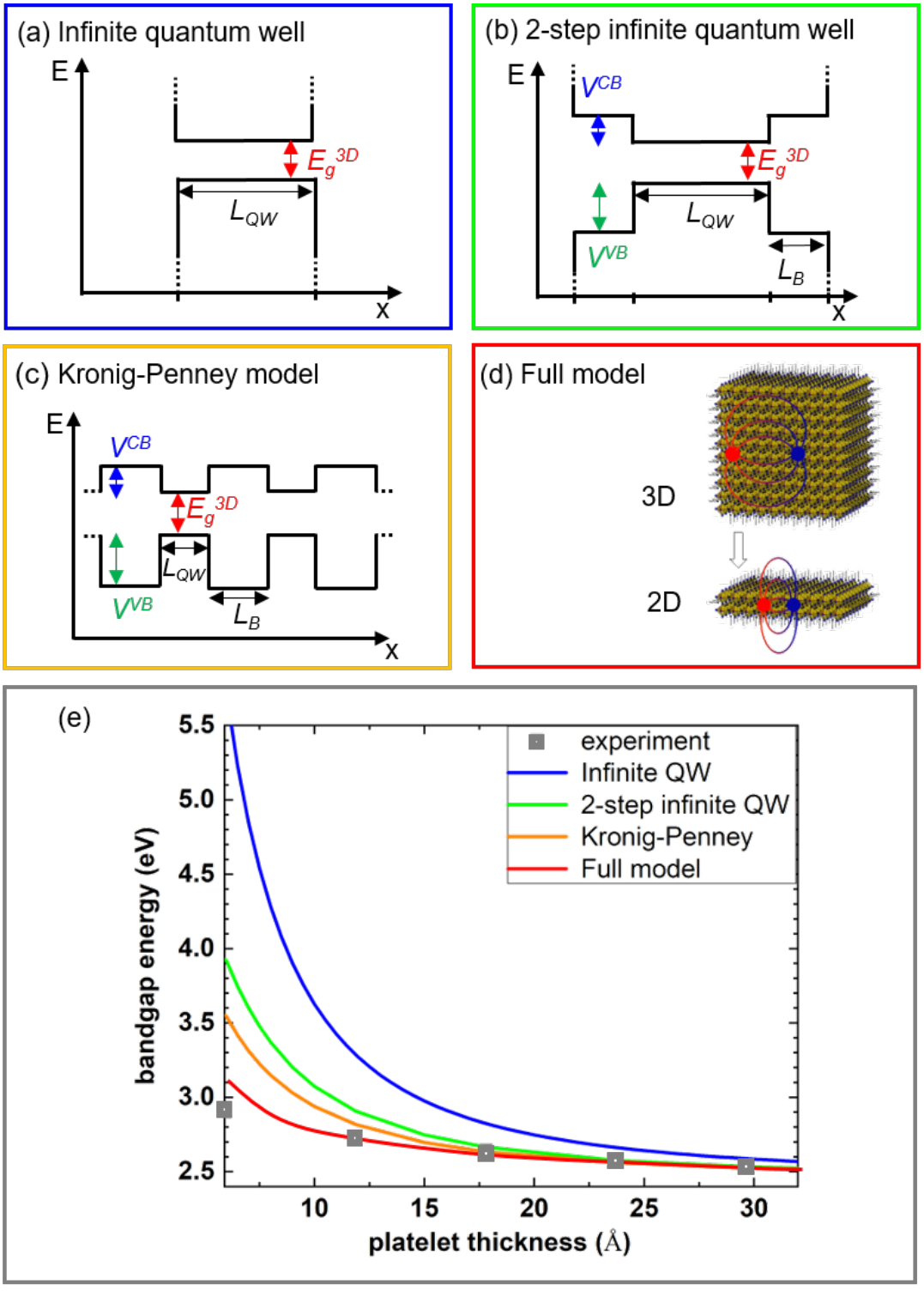

Figure 4.8.: Model calculation of the quantum size effect. (a) to (d) Quantum well models used for (e) model calculations of the energies of perovskite nanoplatelets as a function of platelet thickness (solid lines). Experimental values of the exciton transition energies were obtained from PL measurements (grey squares).

result in enhanced exciton binding energies in the nanoplatelet compared to the bulk-like counterpart.[30] As the dielectric constant of the ligand is significantly lower than in perovskite platelets, the exciton binding energies are enhanced in the thinnest platelets. The modified exciton transition energy E_X is given by $E_X = E_g^{3D} + E_e + E_h - E_b$ (for details see subsection 2.1.5). E_X can be modeled with a formula derived by Guseinov et al.[26] The resulting curve (red, figure 4.8 e) of the full model fits the values for $n \geq 2$ accurately. However for $n = 1$ there remains a discrepancy of 170 meV. A possible source of this discrepancy is the fact that the model calculations approximate the conduction band of the perovskite as parabolic, although it is actually anisotropic.[121] In particular for ultrathin quantum wells this approximation leads to significant deviations as the in-plane curvature of the dispersion relation at the bottom of the subband yields a different effective mass than used in the bulk material. As a consequence, the carrier effective masses depend strongly on the width of the quantum well.[121] Thus, the non-parabolicity could be the source of the remaining mismatch of the full model in the case of $n = 1$. For an accurate calculation of the exciton transition energy in the non-parabolic model, important parameters and constants are not known with sufficient accuracy. Amongst these parameters are the dielectric constants of the perovskite platelets and the adjacent ligand as well as the effective masses in these regions.[122,123] Therefore, this model cannot be employed for this purpose. Possible other methods used to calculate quantum confinement in semiconductors, like density functional theory (DFT), reach certain limitations as well. For density functional theory, for example, an accurate employment of spin-orbit effects represents a limiting factor in accuracy.

4.6. Chapter summary

In this chapter, a new variation of a synthesis was presented for organic-inorganic perovskite nanoplatelets and quantum size effects were investigated in these structures. Through varying the ratio of the ligand to the organic cation in the synthesis perovskite nanoplatelets of different thicknesses down to a monolayer were achieved. During the synthesis higher ligand concentrations resulted in thinner nanoplatelets. PL measurements allowed to experimentally determine the optical bandgaps of perovskite nanocrystals and assign them to nanoplatelets of increasing numbers of unit cells in thickness. The assignment was found to agree well with Kronig-Penney model calculations. Furthermore, it was found that the stacking of nanoplatelets and electronic coupling between them plays an important role in their optical properties. Moreover, for nanoplatelets of one and two unit cells thickness, an enhanced exciton binding energy up to several hundreds of meV was found.

5. Carrier recombination dynamics and exciton-phonon interactions

Understanding carrier recombination dynamics and the interaction of photo-excited charge carriers with phonons in confined perovskite nanocrystals is of fundamental interest and a prerequisite for perovskite application in high-performance optoelectronic devices. Interactions between charge carriers and phonons have an impact on material properties such as carrier diffusion lengths and carrier lifetimes. The synthesis of nanoplatelets presented in chapter 4 allows the investigation of the PL lifetimes and carrier recombination dynamics in dependence of the thickness of the platelets. These measurements at room temperature indicate a reduced lifetime with decreasing thickness most likely related to increased exciton binding energies in the strongly confined nanoplatelets. Furthermore, temperature-dependent steady-state and time-resolved PL measurements were carried out in order to investigate exciton-phonon interactions and decay dynamics in monodisperse $CsPbBr_3$ nanoplatelets with $n = 3$ layer thickness. The results reveal strong exciton-phonon interactions in the nanoplatelets and indicate that the surrounding ligands lead to antiquenching at higher temperatures.

5.1. Thickness-dependent time-resolved photoluminescence spectroscopy

In order to investigate the impact of the platelets' thicknesses on the charge carrier lifetime, time-resolved PL measurements were carried out with a streak camera. This measurement technique allows to resolve the sample's PL lifetime after excitation with a short laser pulse. Hereby, a broad range of wavelengths and their corresponding lifetimes are recorded in one single streak image. In general, time-resolved PL measurements allow an investigation of the decay dynamics of the charge carriers prevalent in the sample. These decay dynamics are influenced by the charge carrier type, as well as properties of the sample, such as its quality and its dimensionality.

The perovskite suspensions were spin coated onto glass substrates. Figures 5.1 a and 5.1 b display the streak camera images recorded at room temperature on two samples, 0 % OA, containing nanocubes, and 60 % OA, containing nanoplatelets of various thicknesses. The excitation wavelength was 405 nm. In both images the wavelength is represented on the x-axis, the time on the y-axis and the PL intensity is color coded. The images allow to extract the spectral position of the PL maxima as well as the decay curves corresponding to each maximum. The 0 % OA image shows only intensity counts around 520 nm. In contrast, the 60 % OA sample shows maxima at multiple wavelengths over a range from 450 nm to 520 nm. In order to extract local PL maxima, the PL intensity counts of the streak image are integrated from 0 ns to 5 ns and the resulting PL spectrum is depicted in figure 5.1 c. The PL spectrum displays local maxima around 450 nm, 465 nm, and 480 nm. Additionally, a broad peak around 506 nm is observed with a shoulder at shorter wavelengths. As already discussed in sections 4.4 and 4.5, the 60 % OA sample contains nanoplatelets of various thicknesses and characteristic emission maxima. Hence, the PL counts around these wavelengths are attributed to radiative recombination from nanoplatelets of $n = 2$, $n = 3$, $n = 4$ unit cells in thickness and thicker nanoplatelets (NP), respectively (compare to section 4.4 and table A.2). Additionally, the emission around 490 nm, that is part of the shoulder of the broad emission peak at 506 nm, is attributed to nanoplatelets of $n = 5$ unit cell thickness.

To extract the decay curves of the nanocubes and the nanoplatelets of different thicknesses separately, the PL counts at these wavelengths are plotted versus time for both streak images (figures 5.1 d, e). In general, the type of the charge carriers and the nature of the decay process determines if the decay is mono-, bi- or tri- molecular (subsection 2.2.3). When the decay curves can be fitted with a monoexponential function, it can either be due to the radiative recombination of excitons or to trap state related recombination of

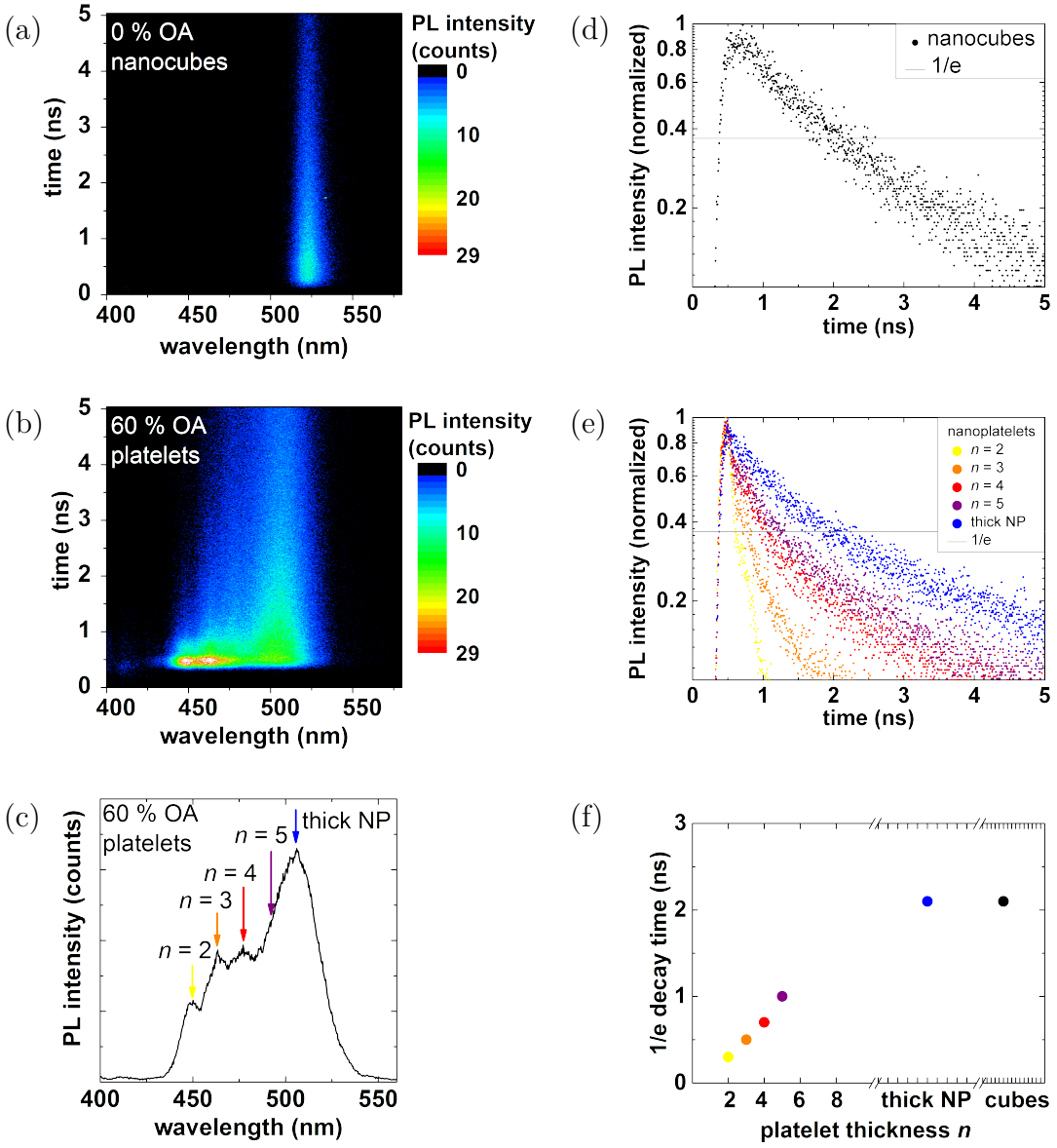

Figure 5.1.: Streak images of different $MAPbBr_3$ samples and analyses. (a) Streak image of a 0 % OA suspension containing $MAPbBr_3$ nanocubes with a single emission maximum at 520 nm. (b) Streak image of a 60 % OA suspension containing nanoplatelets of various thicknesses with characteristic emission wavelengths due to the quantum confinement effect. (c) PL spectrum extracted from (b) by integrating the counts from 0 ns to 5 ns. According to model calculations in previous sections the wavelength maxima are attributed to nanoplatelets with thicknesses of discrete numbers of unit cells $n = 2$ to 5 and to thicker nanoplatelets (NP). (d) PL decay curve extracted from (a) by plotting the counts around 520 nm versus time. (e) Decay curves extracted from (b). (f) 1/e decay times $\tau_{1/e}$ extracted from (d) and (e) show a trend that the lifetime increases with increasing platelet thickness.

either electrons of holes. A bimolecular decay is expected for radiative recombination of free electrons and holes and a trimolecular decay for Auger recombination. For the experiments discussed here, the laser excitation density was chosen low enough that trimolecular decay due to Auger recombination can be excluded. Additionally, effects such as impurities or reabsorption influence the decay dynamics.
The exciton binding energy of the bulk $MAPbBr_3$ lies around 40 meV [75,76,77] which is already higher than the thermal energy at room temperature with a value of 26 meV. As discussed in the previous section, for the $MAPbBr_3$ nanocrystals investigated here the exciton binding energy increases for thinner structures to up to 600 meV for $n = 1$. Therefore, it is unlikely that free electrons and holes are generated in the material and therefore purely excitonic recombination is expected. Consequently, the prevalent carriers are excitons and the PL stems mainly from excitonic recombination which decays monoexponentially. The decay curves measured in these samples cannot be fitted with a single exponential function but they have additional contributions. These might stem from different subensembles of nanoplatelets in the film that was kept under ambient conditions. One subensemble without surface defects and one with surface defects due to exposure to air and therefore strongly reduced or no emission. The two subensembles decay on different time scales resulting in the observed non-monoexponential decay curves. Similar effects were observed by Bohn et al. [124] for colloidal $CsPbBr_3$ nanoplatelets.
To compare the decay times of the different samples, the 1/e decay time constant $\tau_{1/e}$ is extracted from figures 5.1 d and 5.1 e. It amounts to 2.1 ns for the nanocubes and to 0.3 ns, 0.5 ns, 0.7 ns, 1.0 ns, and 2.1 ns for $n = 2, 3, 4, 5$ and thicker nanoplatelets, respectively. The 1/e decay times are graphed against the thickness of the structures in figure 5.1 f. A comparison of these values shows that thinner platelets display a shorter $\tau_{1/e}$. As the radiative decay stems from excitonic recombination, a plausible explanation for the observed trend that $\tau_{1/e}$ is shorter for thinner platelets could be that the higher spatial confinement together with higher exciton binding energy would lead to shorter lifetimes. A similar trend was seen in GaAs quantum wells of different thickness and an inverse dependence of the decay time on the exciton binding energy was derived. [125] The exciton binding energy is found to increase with decreasing quantum well width and thus the decay time is correlated with the quantum well thickness. This correlation is similar to the one observed in this work (figure 5.1 f).

So far, only the total decay time $\tau_{1/e}$ that can be directly extracted from the streak image, was discussed. However, the PL decay occurs via radiative and non-radiative decay. The corresponding radiative and non-radiative decay times τ_r and τ_{nr} are linked to the total decay by [126]

$$\frac{1}{\tau_{1/e}} = \frac{1}{\tau_r} + \frac{1}{\tau_{nr}}. \tag{5.1}$$

The photoluminescence quantum yield (PLQY) Φ_{PL} of the sample is given by[126]

$$\Phi_{PL} = \frac{\tau_{nr}}{\tau_r + \tau_{nr}}. \tag{5.2}$$

When the PLQY and $\tau_{1/e}$ are known for a sample, τ_r and τ_{nr} can be calculated by combining the two formulas above, yielding

$$\tau_r = \frac{1}{\Phi_{PL}} \cdot \tau_{1/e} \tag{5.3}$$

and

$$\tau_{nr} = \frac{1}{1 - \Phi_{PL}} \cdot \tau_{1/e}. \tag{5.4}$$

When the PLQY is close to or equal to one, like it was found for the above mentioned GaAs quantum wells[125], τ_r is almost equivalent to $\tau_{1/e}$. However, for the here investigated nanoplatelets the PLQY is below 30 % (compare to appendix table A.1) and therefore one would need to calculate τ_r for each platelet thickness. Then one could verify if the trend of τ_r with platelet thickness is still valid. For these calculations one would need to know the PLQY for each platelet thickness individually. That is difficult to achieve, however. A drawback of the synthesis method used here is that it yields a suspension of perovskite nanoplatelets that are polydisperse regarding their thickness except for $n = 1$ and $n = 2$. Yet the product yield for $n = 1$ was too low to allow for streak measurements. Thus, it is not possible to determine the PLQY and radiative lifetimes of a dispersion of pure $n = 1$, and neither for pure $n = 3, 4, 5, ...$, separately.

A further drawback of the suspension polydisperse in size is that non-radiative energy transfer and/or PL reabsorption could occur between the samples. For example, the emitted radiation of platelets with $n = 2$ is of sufficiently high energy that it could be reabsorbed by platelets with $n = 3$. This way, during the lifetime measurements, the platelets with $n = 3$ are not only excited by the pulsed laser but possibly constantly reabsorb as long as platelets with $n = 2$ emit. This will have an impact on the carrier lifetimes that can only be solved if the samples were homogeneously dispersed in thickness. Such a modification of the synthesis was carried out at the chair by Dr. Yu Tong and Dr. Verena Hintermayr in parallel to this thesis. Tong et al.[127] altered the synthesis method and succeeded in synthesizing highly emissive $MAPbBr_3$ crystals that are still polydispersed in thickness. Hintermayr et al.[126] developed a synthesis technique for $MAPbI_3$ nanoplatelets with close to monodisperse solutions and minimized contributions for samples up to $n = 3$. In both studies it was demonstrated that the PL lifetime decreases with decreasing nanoplatelet thickness. In both studies, this trend is attributed to the higher spatial confinement and the higher exciton binding energies in 2D structures. In this thesis, the further scope lies on stacks of monolayers and the impact of the interlayer distance that is discussed in chapter 6.

5.2. Exciton-phonon interactions and PL lifetimes in $CsPbBr_3$ nanoplatelets

The temperature-dependence of steady-state and time-resolved PL was measured and analyzed to gain insight into exciton-phonon interactions and carrier recombination dynamics in perovskite nanoplatelets. The investigated samples were $CsPbBr_3$ nanoplatelets with lateral dimensions of about 10 nm and a thickness of 1.8 nm, corresponding to $n = 3$ layers of unit cells. The samples were prepared by Dr. Yu Tong at the same chair where the experiments for this thesis were carried out. In contrary to the previously synthesized $MAPbBr_3$ nanoplatelets, dispersions of $CsPbBr_3$ nanoplatelets can be prepared with a very homogeneous thickness distribution. Considering a reported exciton Bohr radius $r_{Bohr}^{3D} = 7\,\text{nm}$ [110] for bulk $CsPbBr_3$ and an exciton binding energy $E_b^{3D} = 37 - 44\,\text{meV}$ [55,79,80], these nanoplatelets are strongly confined and the exciton binding energy rises to about $E_b^{2D} = 200\,\text{meV}$. [124] So far, the measurements carried out in this work have not been reported for strongly confined $CsPbBr_3$ nanoplatelets but only for weakly confined $CsPbBr_3$ nanocubes of lateral dimensions of 12 nm [66] and 10 nm [128]. The nanoplatelets were prepared with a tip sonication method as briefly presented in subsection 3.1.2. The synthesis yielded nanoplatelets in dispersion of which 20 µl were spin coated onto a sapphire substrate. This substrate was mounted into the cryostat in the TCSPC setup and steady-state PL spectra were taken in steps of about 20 K from 290 K to 10 K. The excitation wavelength was 400 nm and the excitation density was $20\,\text{nJ}\,\text{cm}^{-2}$. A detailed description of the setup and parameters can be found in subsection 3.3.4. The obtained spectra are displayed in figure A.6 a. Each PL emission spectrum was converted from wavelength to energy [129] and fitted by a Gaussian curve fit (figure 5.2 a). From these fits, the PL peak position and the full width at half maximum (FWHM) were determined for each temperature (figure 5.2 b). Furthermore, the PL peak of each PL spectrum was integrated in order to estimate the photoluminescence quantum yield (PLQY) Φ_{PL} for every temperature.

The PL maximum at 290 K is located at 2.728 eV (454 nm) and clearly blue-shifted from the PL maximum of the bulk counterpart at 2.3 eV (540 nm) due to quantum size effects. [130] The PL maximum shifts with temperature. Between 10 K and 230 K, a blue-shift of 12 meV in total is observed with increasing temperature. In contrast, the PL maximum undergoes a red-shift of 6 meV in total between 230 K and 290 K. The blue-shift between 10 K to 230 K can be explained by the p-type character of the conduction band. [66,128] As discussed in detail in subsection 2.2.2, the bandgap of $CsPbBr_3$ is known to undergo a blue-shift with temperature unlike most semiconductors. The red-shift between 230 K to 290 K may does most likely not stem from a phase transition. It it is currently highly debated in literature if $CsPbBr_3$ nanocrystals adopt a cubic or orthorhombic crystal structure at room tempera-

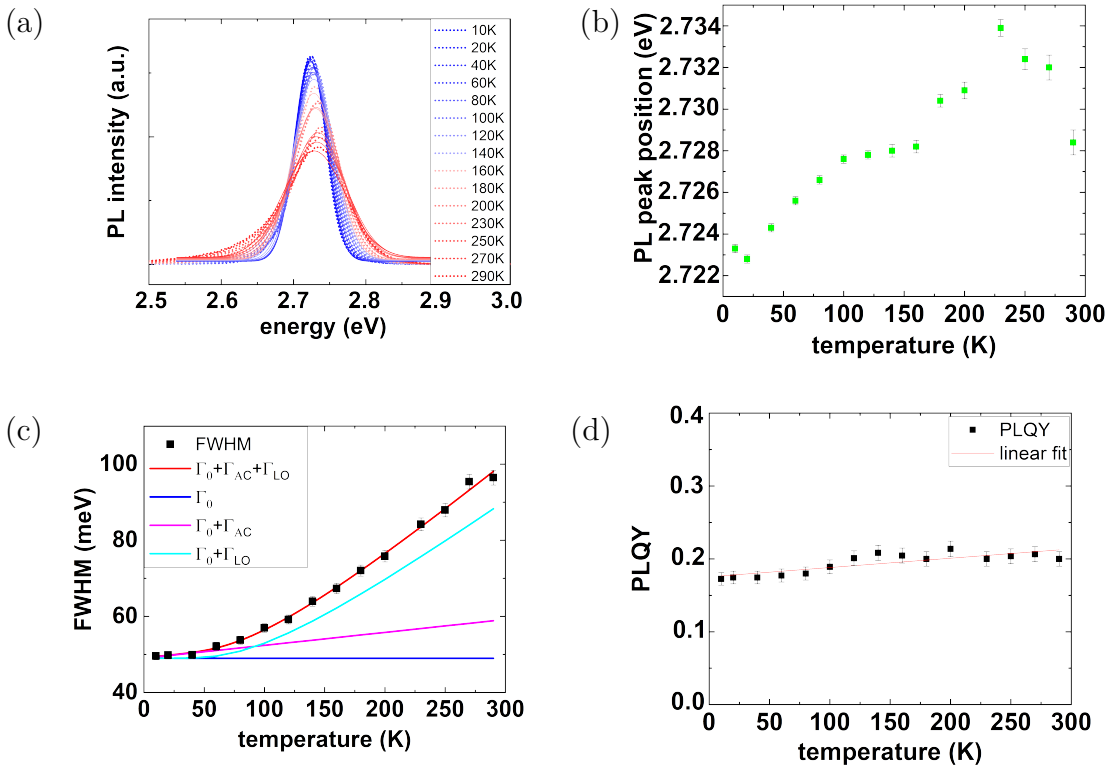

Figure 5.2.: Steady-state PL spectra of $CsPbBr_3$ nanoplatelets at different temperatures and their further analysis. (a) Recorded PL spectra (dotted lines) converted from nm to eV with Gaussian curve fits (solid lines) for different temperatures. (b) PL peak position extracted from (a). (c) The FWHM (black squares) obtained from Gaussian curve fits to the PL spectra in (a) are fitted (red) according to equation 5.5 in order to investigate the exciton-phonon interaction for these nanoplatelets. The individual contributions of the constant offset Γ_0 (blue), the AC phonons ($\Gamma_0 + \Gamma_{AC}$, pink), and the LO phonons ($\Gamma_0 + \Gamma_{LO}$, turquoise) are plotted as well. (d) Photoluminescence quantum yield (PLQY) Φ_{PL} calculated from the integral $A(T)$ of the PL spectra in (a) with equation 5.6 with a linear fit.

ture.[55,56,131,132] Therefore a phase transition at lower temperature cannot be excluded. However, the PL maxima shift gradually and not abruptly as it would be expected for phase a transitions. Consequently, the observed shift does not stem from a phase transition. The observed PL red-shift between 230 K and 290 K likely stems from ligand-induced strain at the platelets surface. The melting point of the oleylamine ligand is around 300 K[133]. The ligands undergo a phase transition when cooled and rearrange due to this phase transition.[134] Thereby ligand-induced strain at the platelets surface, possibly followed by an induced octahedral tilt that can alter the PL emission.

In figure 5.2 c, the extracted FWHM is plotted as a function of temperature. Recalling equation 2.30 discussed in subsection 2.2.2, the overall PL emission broadening $\Gamma_{total}(T)$ is governed mainly by three contributions and is given by the following expression:[67,68]

$$\Gamma_{total}(T) = \Gamma_0 + \Gamma_{AC} + \Gamma_{LO} = \Gamma_0 + \gamma_{AC}\,T + \frac{\gamma_{LO}}{\exp\left(\frac{E_{LO}}{kT}\right) - 1}. \tag{5.5}$$

The first term, $\Gamma_0 = \Gamma_{total}(T = 0\,\mathrm{K})$ is temperature-independent. The second term (Γ_{AC}) stems from excitons coupling to acoustic phonons. It mainly relates to the deformation potential and Γ_{AC} depends linearly on temperature with a factor γ_{AC}. The third term, Γ_{LO} with the Fröhlich coupling constant γ_{LO}, describes the exciton-longitudinal optical phonon interaction. It is associated with the Bose-Einstein distribution of LO phonons given by $\left(\exp\left(\frac{E_{LO}}{kT}\right) - 1\right)^{-1}$ with the energy of the LO phonons E_{LO}, the Boltzmann constant k, and the temperature T.

Equation 5.5 was fitted to the experimental data points and the result plotted (red curve) in figure 5.2 c. The individual contributions of Γ_0, $\Gamma_0 + \Gamma_{AC}$, and $\Gamma_0 + \Gamma_{LO}$ are plotted in the graph as well. The FWHM of the PL depends significantly on the temperature and increases from 49.5 meV at 10 K to 96.5 meV at 290 K, implying a strong exciton-phonon interaction. Below 60 K, the PL broadening is dominated by the contribution of the acoustic phonons while the LO phonon contribution becomes negligible. At $T \approx 90\,\mathrm{K}$ there is a crossover and above this temperature the LO contribution exceeds the acoustic phonon contribution. The curve fit quite accurately describes the data with $R^2 = 0.998$. Including an additional impurity term [66] into equation 5.5 or leaving out the contribution of the acoustic phonons yields poorer results.

The parameters obtained by the curve fit are summarized in table 5.1, as well as values reported for weakly confined $CsPbBr_3$ nanocubes. [66,128] The LO phonon energy E_{LO} is found to be (24.9 ± 5.0) meV and is in between the reported values. The high exciton binding energy in the here investigated $CsPbBr_3$ nanoplatelets of around $E_b = 200$ meV [124] indicates that excitons are highly stable at room temperature as $E_b > E_{LO} \geq kT$. The coupling constant with acoustic phonons, γ_{AC} and the Fröhlich coupling constant γ_{LO} adapt values of (34.2 ± 8.6) meV and (66.7 ± 11.4) meV, respectively. Both values are comparable to the respective values reported for nanocubes. [66,128] A final conclusion whether the decrease in dimensionality from nanocubes to nanoplatelets leads to an increase or de-

Sample	Γ_0 (meV)	γ_{AC} (μeV/K)	γ_{LO} (meV)	E_{LO} (meV)
$CsPbBr_3$ platelets (1.8 nm)	49.1 ±1.0	34.2 ±8.6	66.7 ±11.4	24.9 ± 5.0
$CsPbBr_3$ cubes (12 nm) [66]	40.0 ± 0.5	33.1 ± 11.1	86.7 ± 31.4	44.4 ± 10.2
$CsPbBr_3$ cubes (10 nm) [128]	20	5	45	19*

Table 5.1.: Tabular representation of parameters obtained through a curve fit of the FWHM data and literature values. Constraint values are marked with an asterisk.

crease of the parameters γ_{AC}, γ_{LO}, and E_{LO} is not possible. In order to draw further conclusions measurements on various monodisperse samples containing nanoplatelets of different thickness are necessary. The present literature[66,128] values are ambiguous and thus hinder a final conclusion.

At 290 K, the measured PLQY amounts to (20 ± 1) %. For lower temperatures, the PLQY could not be measured directly. Yet the PLQY $\Phi_{PL}(T)$ for each temperature can be calculated from the ratio of the respective integrated PL peak $A(T)$ and the integrated PL peak at 290 K, $A(T = 290\,\mathrm{K})$:

$$\Phi_{PL}(T) = \Phi_{PL}(T = 290\,\mathrm{K}) \cdot \frac{A(T)}{A(T = 290\,\mathrm{K})}. \tag{5.6}$$

A requirement for the validity of this equation is that the absorption does not change with temperature. This requirement is fulfilled in a first approximation for the sample under investigation for the used excitation wavelength of 400 nm. The PLQY adapts values between a maximum of $\Phi_{PL} = 21$ % at 200 K and a minimum of $\Phi_{PL} = 17$ % at 10 K (figure 5.2 d). A linear curve fit is applied to the data points and reveals an increase of the PLQY when the temperature is raised from 10 K to 290 K. This is surprising as it is the opposite to the usually observed quenching of luminescence with temperature. To explain the trend of the PLQY with temperature, a closer look at the samples is helpful. The nanoplatelets have a high surface-to-volume-ratio of about $1.2\,\mathrm{nm}^{-1}$.[124] Examining semiconductor CdSe quantum dots with a high surface-to-volume ratio, Wuister et al.[134] found a similar trend for the PLQY in their nanoparticles. They observed an antiquenching of the PL at room temperature and attribute the quenching at low temperature to defect states at the nanoparticle surface at lower temperatures. These defect states are introduced by phase changes of the ligand that introduce strain on the crystal surface, resulting in a drop of PLQY. In a further report on CdTe nanoparticles, Wuister et al.[135] showed that depending on the ligand and the solvent, the antiquenching with temperature can be very abrupt and drastic. The here investigated nanoplatelets, too, may be affected by an antiquenching of PL at higher temperatures, albeit that the here observed antiquenching is less abrupt and drastic then reported by Wuister et al.[135] For the implementation of the nanoplatelets in optoelectronic devices operated at room temperature and above this antiquenching might be an advantage. Further experiments with different ligands could be helpful to explore if there is significant antiquenching at room temperature.

Figure 5.3 shows the PL intensity decay measured with TCSPC. The decay curves were recorded for each temperature step between 10 K and 290 K at which also the PL spectra were acquired. The excitation wavelength was 400 nm and the decay curves were measured for the wavelength of the respective maximum of each PL spectrum. Experimental details can be found in subsection 3.3.4. For each decay curve the lifetime $\tau_{1/e}$ is determined, defined as the time at which the PL intensity has dropped to 1/e of its initial value. At

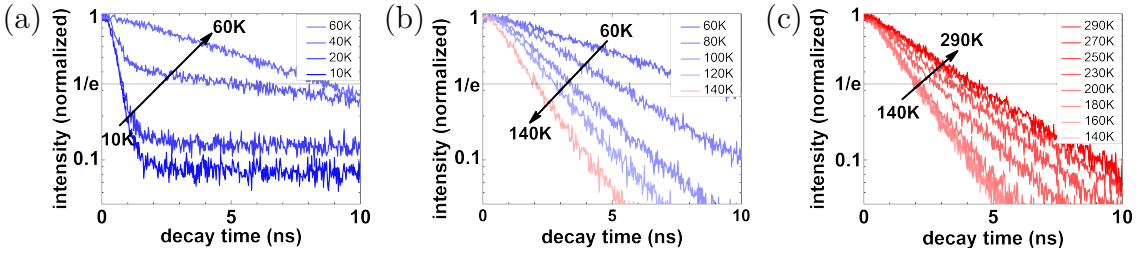

Figure 5.3.: Time-resolved PL measurements of $CsPbBr_3$ nanoplatelets recorded at different temperatures. The temperature-dependent PL lifetime measurements show that the PL lifetimes can be divided into three different parts. (a) From 10 K to 40 K, a short and a long contribution to the decay is observed. With increasing temperature the average decay time $\tau_{1/e}$ increases. (b) From 60 K to 140 K monoexponential decay curves and decreasing $\tau_{1/e}$ with temperature is observed. (c) From 140 K to 290 K the decay curves are monoexponential and $\tau_{1/e}$ increases again.

10 K a biexponential decay is observed with a fast component and a slow component (figure 5.3 a). When the temperature is raised, the fast component becomes slower and the slow component faster. Between 10 K and 60 K $\tau_{1/e}$ increases from 1.0 ns to 8.7 ns with temperature (see also appendix figure A.6 b). In fact, the decay time of 1.0 ns is at the limit of the instrument resolution and might even be faster. The amplitude of the short component decreases and eventually vanishes above $T = 40$K. Between 60 K and 140 K the nanoplatelets exhibit decay curves with a simple exponential behavior and $\tau_{1/e}$ decreases from 8.7 ns to 2.0 ns with increasing temperature (figure 5.3 b). Figure 5.3 c, in contrast, displays monoexponential decay curves between 140 K and 290 K showing an increase of $\tau_{1/e}$ from 2.0 ns to 4.2 ns with increasing temperature.

The decay curves over the whole temperature range likely stem from monomolecular recombination of excitons as the exciton binding energy lies around $E_b^{2D} = 200\,\text{meV}$ [124] in these structures and is thus significantly higher than the thermal energy at room temperature (26 meV). Thus the exciton binding energy is too high for the excitons to dissociate significantly into free charge carriers. As the PLQY of the sample is rather low, equations 5.1 to 5.4 cannot be applied to calculate the radiative and nonradiative decay times τ_r and τ_{nr}. These equations require quantum yields close to unity to be applicable which is not fulfilled for the present samples with PLQY between $\Phi_{PL} = 17\,\%$ and $\Phi_{PL} = 21\,\%$. The low PLQY leaves room for the existence of subensembles of nanoplatelets that are only luminescent at certain temperatures due to enhanced trap-assisted recombination. Especially for these very thin structures with high surface-to-volume ratios, the susceptibility to surface defects can be extremely high, as shown previously by Bohn et al. [124]

Instead of equations 5.1 to 5.4, a three-level system is used to interpret the data for the temperature range from 10 K to 40 K. The three-level system is composed of a zero exciton

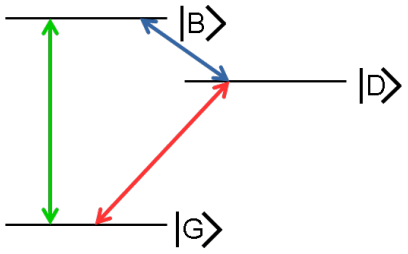

Figure 5.4.: Three-level system used to interpret the data. It is composed of a zero exciton state $|G\rangle$ and two states, denoted $|B\rangle$ and $|D\rangle$, corresponding to the bright and dark excitons.

state $|G\rangle$ and two states, denoted $|B\rangle$ and $|D\rangle$, corresponding to bright and dark excitons (figure 5.4). Between 10 K and 40 K, the fast decay curve stems from the bright exciton transition from $|B\rangle$ to $|G\rangle$ and the slow decay from the dark exciton transition from $|D\rangle$ to $|G\rangle$. Above 40 K, the decay times of bright and dark excitons cannot be resolved any more.

The lengthening of the lifetimes with temperature above 140 K can be attributed to the decreasing coherence volume of the exciton with temperature that leads to enhanced exciton lifetimes. A similar effect was observed in GaAs quantum wells and later described theoretically, albeit at lower temperature.[138,139] However, GaAs quantum wells possess an exciton binding energy of about 10 meV,[140,141] whereas the nanoplatelets investigated here have an exciton binding energy of more than 200 meV[124]. This may explain why the effect is observed at higher temperatures for perovskite nanoplatelets than for GaAs quantum well structures.

The excitonic fine structure and the origin of the bright and dark excitons in $CsPbBr_3$ are currently highly debated.[136,142,143,144,145] Nevertheless, several publications agree on the fact that the size and dimensionality of the sample is a crucial factor when determining the fine structure.[136,142,143,145] Thus one would need to conduct more experiments on the samples investigated here in order to reveal the origin of the bright and dark states and to explain the observed lifetimes over the whole temperature range in detail. Furthermore, in order to fit the decay curves of the nanoplatelets accurately, solving the rate equations is not sufficient. Instead, one would need to solve master equations in order to describe the system in detail.[146]

5.3. Chapter summary

In this chapter, thickness-dependent carrier recombination dynamics in $MAPbBr_3$ perovskite nanoplatelets were investigated as well as exciton-phonon interactions and tempera-

ture-dependent lifetimes in $CsPbBr_3$ all-inorganic perovskite nanoplatelets. Thickness-dependent lifetime measurements demonstrated that thinner structures show shorter lifetimes. Most likely, the higher spatial confinement together with the increased exciton binding energy in thinner structures results in shorter lifetimes. Temperature-dependent steady-state PL measurements on $CsPbBr_3$ nanoplatelets with a thickness of $n = 3$ layers revealed a strong exciton-phonon coupling that leads to significant broadening of the PL emission spectrum with temperature. At room temperature the dominant contribution arises from the Fröhlich type carrier interaction with LO phonons. The Fröhlich coupling constant γ_{LO} was determined to be (66.7 $\pm$11.4) meV and the LO phonon energy E_{LO} as (24.9 $\pm$5.0) meV. At temperatures below $T \approx 90$ K the acoustic phonon interactions dominate over the contributions from LO phonons and γ_{AC} was found to be (34.2 $\pm$8.6) μeV/K. Temperature-dependent PLQY measurements revealed an antiquenching behavior in these nanoplatelets at higher temperatures and indicated that the role of the ligand is highly important in these structures with high surface-to-volume ratio. Temperature-dependent lifetime measurements revealed two different contributions to the lifetimes below 60 K, one fast and one slow component. This is explained by a three-level system with the fast decay from a bright exciton and a slow decay from a dark exciton. To elucidate the origin of these two excitonic states and the exciton fine structure, further experiments are needed. For temperatures above 140 K an increase in the exciton lifetime with temperature is observed that can be attributed to a decreasing coherence volume. Again, this effect as well as the excitonic fine structure highly depend on size and dimensionality of the sample, highlighting the importance of these parameters.

6. The influence of octahedral tilt and electronic coupling on the optical properties of layered hybrid perovskites

Layered hybrid perovskites are a subcategory of perovskites. They consist of multiple stacks of 2D perovskite sheets separated by large organic cations. Similar to 3D perovskites, the substitution of the halide ions offers a possibility to alter the material properties. In comparison to 3D perovskites, however, the choice of the large cation offers an additional parameter to tune the material properties. While the functional group of this cation is an ammonium, the organic moiety can be chosen of variable length and chemical composition. Similar to 3D perovskites, octahedral tilt also plays a role in layered hybrid perovskites. Before the rise of 3D perovskites for solar cell applications, layered hybrid perovskites had been subject of intense studies. First optical studies on alkylammonium lead iodide, that is investigated in this chapter, were already conducted in the late 1980s by Ishihara et al.[23,147] First applications of layered hybrid perovskites as thin-film field effect transistors were shown by Mitzi et al. in the mid 1990s.[82,83] Recently, layered hybrid perovskites have re-emerged as potential technological solutions for next-generation photovoltaic and optoelectronic applications.[148] In this chapter, the interlayer spacing in layered hybrid perovskites is controlled through a systematic variation of the length of the alkyl moiety. The results presented in this chapter allows to gain new insights regarding the effects of ligand-induced octahedral tilt and electronic coupling on the excitonic energies of the perovskite sheets.

6.1. Interlayer spacing and formation of multiple quantum well structures

The layered hybrid perovskites investigated here are based on lead iodide with alkylammonium as additional large cation. The chain length is given by the number of C-atoms l. In this work, it is varied from $l = 4$ to 18. The correct chemical formula $(C_lH_{2l+1}NH_3)_2PbI_4$ will hereafter be abbreviated with C_lPbI_4. Figure 6.1 a displays a schematic drawing of these structures. The perovskite layers consist of corner-sharing PbI_6 octahedra that are separated by intercalated organic cations. Hereby, the ammonium functional groups of the organic cations stabilize the inorganic octahedra while their alkyl chains interact via van der Waals forces.

The samples were prepared as polycrystalline films as described in detail in subsection 3.1.3. Briefly, a 1.0 molar C_l-ammonium iodide solution in dimethylformamide (DMF) and a 0.25 molar lead iodide solution in DMF were mixed in a stoichiometric ratio of 2:1

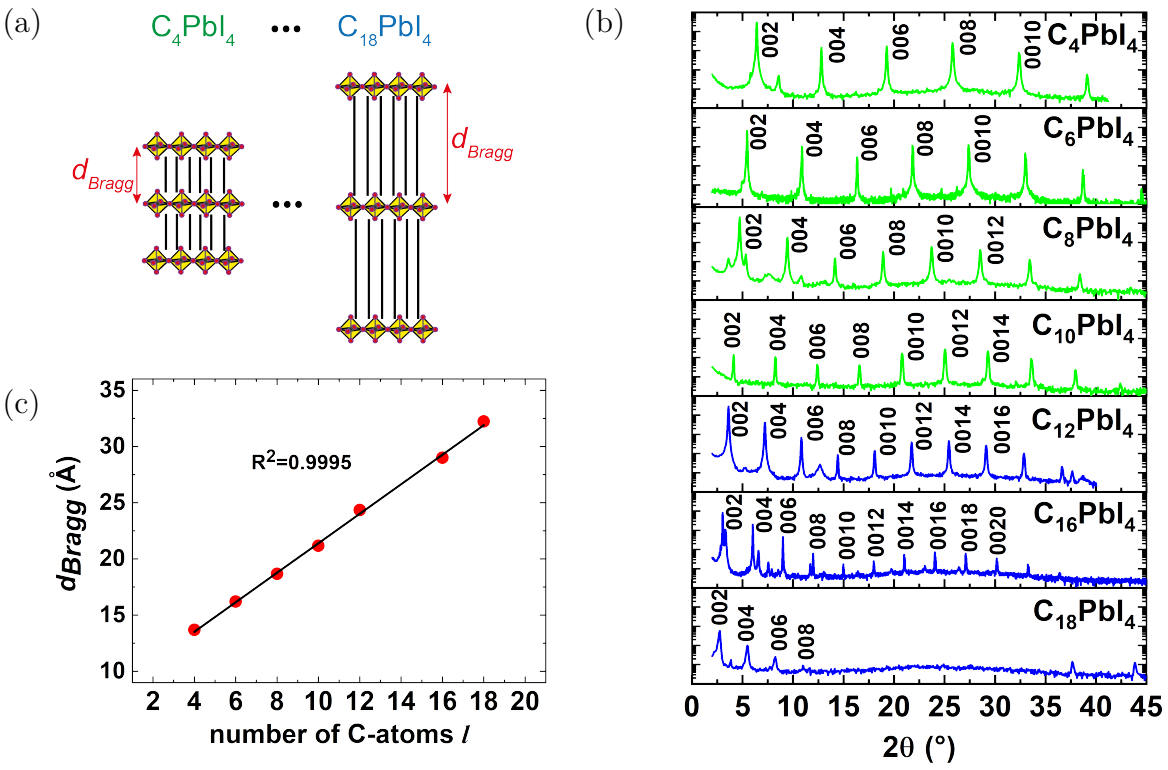

Figure 6.1.: Structural analysis with XRD. (a) Schematic drawing of C_lPbI_4 crystal structures as reported by Billing and Lemmerer [85,86,87] with the octahedra center-to-center distance d_{Bragg}. (b) XRD spectra of C_lPbI_4. All samples show an orthorhombic crystal configuration. [85,86,87,97] (c) Dependence of the interlayer spacing d_{Bragg} on ligands' length derived from XRD spectra using Bragg's law. The black line is a linear fit given by $d_{Bragg} = (1.31 \cdot l + 8.27)$ Å with the number of C-atoms l in the hydrocarbon chains.

and subsequently drop casted on a glass substrate. The perovskite crystals formed upon evaporation of the organic solvent.

As mentioned before, the investigated material is well-known to form quasi-2D structures. To confirm that the synthesized structures were indeed layered hybrid perovskites, X-ray diffraction (XRD) measurements were carried out (figure 6.1 b). All spectra revealed very prominent equidistant peaks typical of 2D structures. Further analysis of the spectra showed that all samples crystallized in an orthorhombic crystal configuration at room temperature, showing prominent peaks in the XRD spectra in the $(002\,k)$ direction where $k = (1, 2, 3, ...)$.[85,86,87,97] When the crystals form on the glass substrate, the unpolar hydrocarbon chains align preferentially perpendicular to the substrate surface and thus the perovskite sheets preferentially stack parallel to the glass substrate.[149] This leads to the observed dominant peaks in the XRD spectra in the $(002\,k)$ direction. As explained in detail in subsection 3.2.1, the distance between two crystal planes can be calculated with Bragg's law (equation 3.3). Here, it was used to determine the octahedron-to-octahedron center-to-center distance between neighboring layers, hereafter referred to as d_{Bragg}. As depicted in figure 6.1 c, d_{Bragg} was found to increase linearly with the length of the organic molecule from 13.6 Å to 31.5 Å, in excellent agreement with previously reported values.[85,86,87] As discussed in subsection 2.3.1, layered hybrid perovskites can be described as multiple stacks of organic and inorganic semiconductor sheets with a band alignment of type-I semiconductors. Further analysis in this respect follow in subsection 6.3. For this, some geometric data concerning the width of the inorganic and organic layers are extracted from the XRD measurements. Taking the width of the PbI_6 perovskite layers $L_{QW} = 6.0$ Å[150] into account, the thickness of the organic ligand layer separating the individual perovskite layers lies between 7.6 Å for C_4PbI_4 and 25.5 Å for $C_{18}PbI_4$. This control over interlayer distance is the starting point for the following investigation on the impact of this parameter on the optical properties of the material.

6.2. Ligand-mediated octahedral tilting and emission wavelength

Here, PL and absorption spectra are discussed and correlated to the samples' structures (sketched in figure 6.2 a). In the beginning the ligand length will be considered as the only influence on the PL spectra. But it will become clear that additional factors must be considered to explain the optical properties. It is found that one of this parameters is the ligand-induced octahedral tilting as discussed in detail further below.

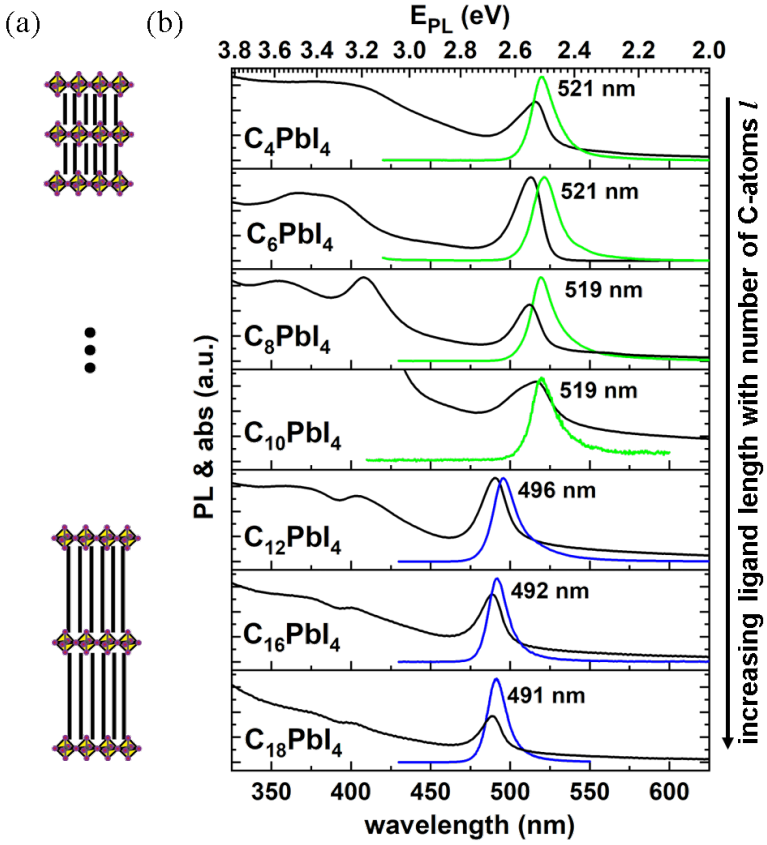

Figure 6.2.: PL and absorption spectra of the C_lPbI_4 films at room temperature. (a) Sketch of the layered hybrid perovskite with varying ligand length. (b) While the samples with relatively short ligands emit around 519 - 521 nm, the samples with long ligands emit around 491 - 496 nm.

sample	**PL peak (nm/eV)**	**exciton peak (nm/eV)**	**Stokes shift (meV)**	**tilt β (°)** from [85,86,87]
C_4PbI_4	521 nm/2.3797 eV	516 nm/2.4028 eV	23 meV	24.93 °
C_6PbI_4	521 nm/2.3797 eV	514 nm/2.4121 eV	32 meV	24.35 °
C_8PbI_4	519 nm/2.3889 eV	512 nm/2.4216 eV	33 meV	23.94 °
$C_{10}PbI_4$	519 nm/2.3889 eV	516 nm/2.4028 eV	14 meV	24.07 °
$C_{12}PbI_4$	496 nm/2.4997 eV	491 nm/2.5251 eV	25 meV	29.81 °
$C_{16}PbI_4$	492 nm/2.5355 eV	489 nm/2.5355 eV	16 meV	30.48 °
$C_{18}PbI_4$	491 nm/2.5407 eV	488 nm/2.5407 eV	16 meV	30.61 °

Table 6.1.: Summary of results from PL and absorption measurements on C_lPbI_4 and octahedral tilt angle β extracted from Billing and Lemmerer [85,86,87].

The color of the films was yellow to orange under ambient illumination at room temperature, in agreement with previous reports on layered hybrid perovskites.[85,86,87] To determine the ligands' effect on the optical properties, absorption and PL spectra were recorded for all samples (figure 6.2 b). As characteristic for 2D semiconductors, all absorption spectra show a prominent 1s exciton peak and a continuum absorption onset at shorter wavelengths. The PL spectra show a single emission peak. All samples display a small Stokes shift to the excitonic peak of $14 - 33$ meV (compare to table 6.1), indicating excitonic recombination. The PL maxima are located at about 521 nm for the films with shorter hydrocarbon chains ($l = 4-10$). These films undergo a slight blue-shift of 2 nm (9 meV) in total with increasing ligand length. The PL emission exhibits a jump of 23 nm (110 meV) to shorter wavelength between the $C_{10}PbI_4$ and $C_{12}PbI_4$ samples, followed by a further gradual blue-shift of 5 nm (25 meV) up to the $C_{18}PbI_4$ perovskite sample. All values are listed in table 6.1. If one only considers the variation in ligand length, one might expect a simple correlation between ligand lengths and PL maxima. Therefore, the jump in PL is quite surprising. In the following, effects and parameters are discussed that are known to lead to a significant change in emission wavelength.

Phase transitions are known to lead to similar jumps in PL and absorption in layered hybrid perovskites. For $C_{12}PbI_4$ a reversible switching of the excitonic energy has been reported by Pradeesh et al.[151] when the crystal structure underwent a temperature-induced phase transition from orthorhombic to monoclinic around 60 °C (see appendix figure A.10). The phase transition is accompanied by a change in the bandgap energy. The change in PL and absorption was reversible when the structure was cooled down and adapted its initial phase. Yet, all samples here crystallized in the orthorhombic structure at room temperature as shown with XRD above. Thus, in contrast to Pradeesh et al.[151], a crystal phase transition cannot explain the observed blue-shift.

Another structural parameter, the Pb-I-Pb bridging angle, is known to undergo slight changes that do not necessarily lead to a phase transition. The effect that the bridging angle differ from the ideal 180° is also referred to as octahedral tilt. Figure 6.3 a shows a sketch where the difference of the bridging angle to the ideal 180° is indicated as tilt angle β. A correlation between E_{PL} and octahedral tilt angle β was experimentally observed for related layered perovskite structures.[43,149,152,153,154,155] For the here investigated C_lPbI_4 with l varying from 4 to 18, detailed structural data is available that was acquired by Billing and Lemmerer.[85,86,87] So far, this data were not yet correlated with optical measurements. Billing and Lemmerer observed a jump in octahedral tilt angles for C_lPbI_4 between $l = 10$ and $l = 12$. The position of the jump in tilt thus coincides with the here

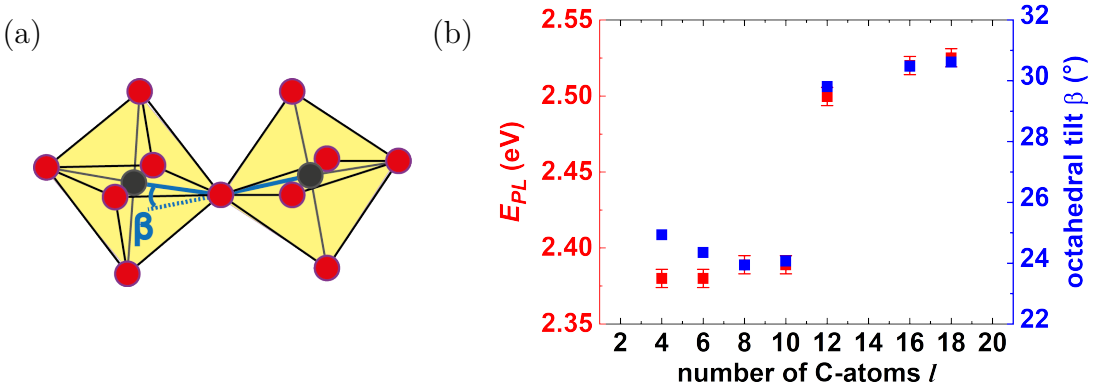

Figure 6.3.: Octahedral tilting and emission wavelength. (a) Schematic drawing of two adjacent octahedra and the tilt angle β in between them. The I^--ions are depicted in red, the Pb^{2+}-ions in black. (b) E_{PL} extracted from the measured data summarized in table 6.1 and PbI_6 octahedral tilt angles extracted from Billing and Lemmerer [85,86,87] in dependence on the hydrocarbon chain length. There is a large jump for both E_{PL} and β between $l = 10$ and $l = 12$. The error bars for the tilt angle β are too small to be depicted.

observed position of the jump in E_{PL}. To visualize a correlation, the experimental values of the octahedral tilt angles as reported by Billing and Lemmerer and the here measured PL energy maxima E_{PL} are plotted against the organic ligand chain length (figure 6.3 b). The jump in octahedral tilt aligns nicely with the jump in E_{PL}. A good correlation between tilt angle and E_{PL} is observed for long ligands, while shorter ligands show deviations from this trend.

Figure 6.4 a shows the PL curves of C_4PbI_4 and $C_{18}PbI_4$ with schematic drawings of their respective octahedral tilt angles that is in large part determining the emission wavelength. The shift in emission wavelength accounts for almost 30 nm (100 meV) and the difference in tilt angle for about 5 °. The relation between these two parameters can be visualized more effectively by plotting the tilt angle directly versus E_{PL} in figure 6.4 b. Applying a linear fit to the graph yields an R^2 value of 0.9744, indicating a good correlation between the two parameters. The samples with long ligands are on the fit within the experimental error. Nevertheless, in the group of short ligands two data points are above the fit and two are below. As the octahedral tilt does not show a simple correlation with the ligand lengths (compare to last column in table 6.1), the two data points above the fit correspond to C_8PbI_4 and $C_{10}PbI_4$, whereas the two data points below correspond to C_6PbI_4 and C_4PbI_4. Discussing the reason why certain octahedral tilt angles are adopted with certain ligands is beyond the scope of this thesis. In the following, the observed trend that octahedral tilt correlates with E_{PL} will be discussed considering recent advances in the field and the applicability of a simple fit of E_{PL} and l.

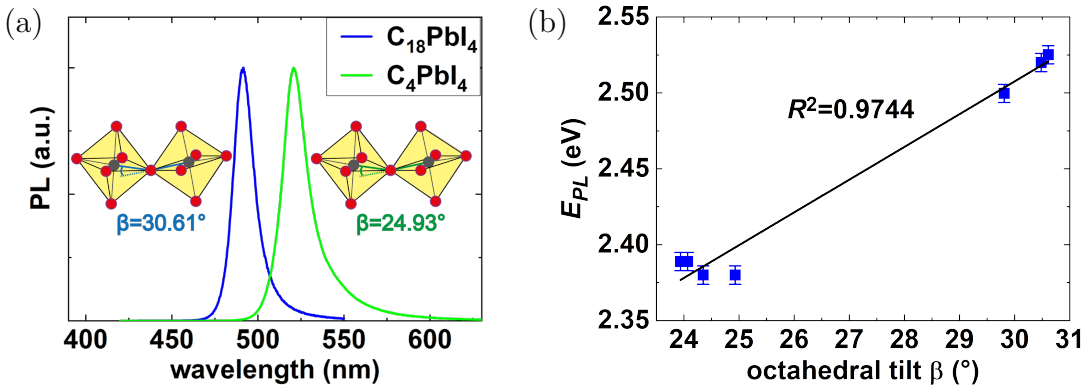

Figure 6.4.: Correlation of octahedral tilting with emission energy. (a) Schematic illustration of the correlation between octahedral tilt and PL spectra for C_4PbI_4 and $C_{18}PbI_4$. The shift in emission wavelength accounts for almost 30 nm (100 meV) and the difference in tilt angle for about 5 °. (b) E_{PL} versus octahedral tilt angle. Both parameters are extracted from data in figure 6.3. The blue line represents a linear fit with $R^2 = 0.9744$. While the fit suggests a very strong correlation of E_{PL} and octahedral tilt within the group of long ligands, there are significant deviations for the short ligands.

6.3. Electronic coupling between multiple perovskite layers

It was shown above that the PL energy in layered hybrid perovskites can be predicted in large parts from the octahedral tilt of the structure. Yet, especially for short ligands this predictions overestimates the bandgap suggesting that additional effects must be considered. Electronic coupling is a distance-depending effect that is known to decrease the bandgap energy in a coupled system. The decrease will be stronger for short distances and vanish for large distances. In this section, this effect will be discussed with respect to the layered hybrid perovskites. First, a short general introduction to the effect is given, followed by model calculations. Thereafter the results and limitations of the model will be discussed.

As explained in detail in subsection 2.3.1, the inorganic perovskite layers can be seen as semiconductor quantum wells with potential wells for both electrons and holes. The quantum wells are separated by a layer of organic ligand, the barrier layer. It is well-known that the PL stems from excitonic recombination in the inorganic layer.[46,88]
Using equation 2.17 the exciton Bohr radius for the 3D bulk counterpart ($MAPbI_3$) can be estimated to be 2.9 nm (see appendix A.4), which is in line with literature values.[156] The inorganic layer, accounting for approximately 6 Å in height, is extremely thin in comparsion to the exciton Bohr radius. This leads to a strong blue-shift of the energetic bandgap and also to higher exciton binding energies (compare to subsection 2.1.5).[34,150,157] In agreement with this assumption, for $C_{10}PbI_4$, an exciton binding energy of 320 meV and

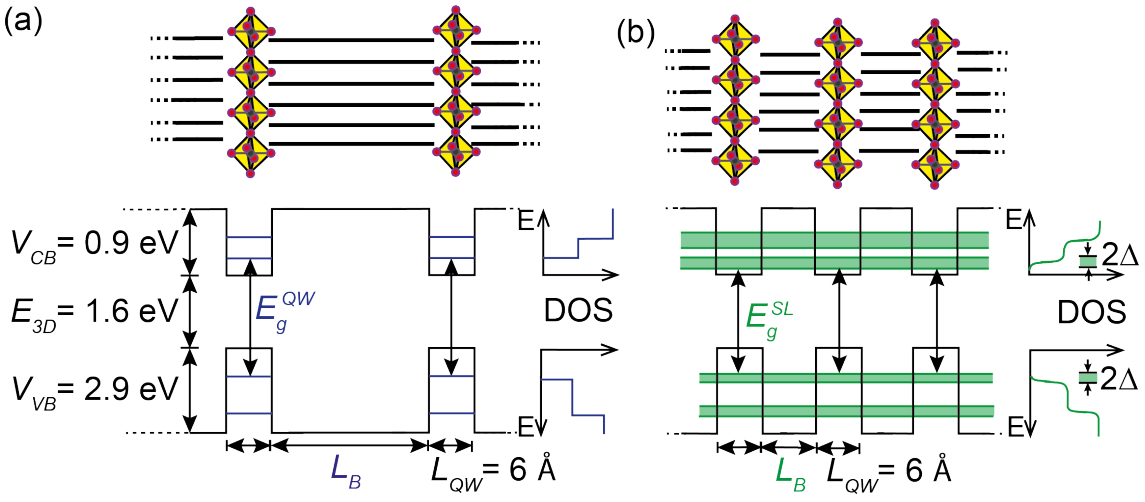

Figure 6.5.: Isolated and coupled quantum wells and the respective energy levels. (a) Sketch of layered hybrid perovskites with long ligands and schematic representation of the energy levels in isolated quantum wells and the corresponding step-like density of electronic states. (b) Sketch of layered hybrid perovskites with short ligands and schematic representation of the energy levels in a quantum well-superlattice and the corresponding density of electronic states. Electronic coupling leads to the formation of minibands with a width of 2Δ and a concomitant lowering of the transition energy E_g^{SL}.

an exciton Bohr radius of 1.6 nm was reported.[157] Yet, if the perovskite layers are brought close enough together, the layers can no longer be considered isolated but electronic coupling between neighboring layers is expected. In classic semiconductor systems, such as GaAs/AlAs, electronic coupling between quantum wells or superlattice formation is a well-known effect.[158,159,160] As explained in detail in subsection 2.1.3, an isolated quantum well has discrete energy eigenvalues and a step-like density of states (DOS) distribution (figure 6.5 a). In a superlattice electronic coupling leads to the formation of minibands of width 2Δ (figure 6.5 b). The electronic coupling increases with decreasing well separation. Although the DOS is continuous in the range of the miniband, the charge carriers recombine between the miniband edges. This leads to a transition energy which is smaller than that of an isolated quantum well. In the limit of an infinitely long barrier, the energy levels of the isolated quantum well are recovered. Apart from the barrier length, there are several other parameters that influence the occurrence of coupling, such as the quantum well potential, the effective masses of carriers, and the quantum well thickness. These parameters are taken into account in the following to model the electronic coupling.

For the calculations, a one-band effective mass Kronig-Penney model was applied. This model can be used to describe the quantum well electronic coupling in the limit of an infinitely long alternating inorganic and organic layer.[161,162] Details and formulas regarding the Kronig-Penney model can be found in subsection 2.1.3. The parameters were set as $L_{QW} = 6\,\text{Å}$, $V_{CB} = 0.9\,eV$, and $V_{VB} = 2.9\,eV$.[150] As mentioned before, the dis-

tance between the layers, L_B, is calculated by subtracting L_{QW} from the Bragg distance, $L_B = d_{Bragg} - L_{QW}$. Parameters that are difficult to choose are the effective masses of electrons and holes. This is due to a lack of experimental values, especially in the 2D case.[163] Nevertheless, they can be approximated from values of the 3D case, where the effective masses for electrons and holes are likely quite similar and approximated to be between $0.1\,m_e$ and $0.2\,m_e$.[164] As the effective masses are expected to be significantly larger (up to 3 to 4 times) in 2D structures than in the bulk case,[165] in this thesis $m^*_{QW} = 0.5\,m_e$ and $m^*_B = 1\,m_e$ were chosen. This should constitute a good approximation. The modified bandgap energy $E_g^{SL}(l)$ is given by the formula:

$$E_g^{SL}(l) = E_g^{3D} + E_e(l,\, q = 0) + E_h(l,\, q = 0), \tag{6.1}$$

where $E_g^{3D}(l)$ is the bandgap energy of the 3D material and $q = 0$ accounts for fact that the material is a direct semiconductor.
Figure 6.6 depicts the calculated values for $E_g^{SL}(l)$ versus the ligand length. For all barrier widths L_B from an infinite length down to the equivalent of a ligand length of $l = 12$, the energy E_g^{SL} assumes a constant value $E_g^{SL}(l \geq 12) = 2.68\,\text{eV}$. This value is equal to the energy for an infinite barrier spacing that recovers the energy of an isolated quantum well E_g^{QW},

$$E_g^{QW} = E_g^{3D} + E_e(l \to \infty,\, q = 0) + E_h(l \to \infty,\, q = 0). \tag{6.2}$$

For ligands $l < 12$, $E_g^{SL}(l)$ decreases exponentially, reaching a minimum of $E_g^{SL}(l = 4) = 2.65\,\text{eV}$ for the lowest length applied ($l = 4$). The drop in energy is due to miniband formation that are hereby shown to occur for ligands $l \leq 11$, but not for longer ligands. The miniband formation lowers the transition energy by $\Delta E(l) = E_g^{QW} - E_g^{SL}(l)$ between $\Delta E(l = 10) = 2\,\text{meV}$ and a maximum of $\Delta E(l = 4) = 28\,\text{meV}$ for the shortest ligand. For all values, see appendix table A.2 in the appendix.

The result that minibands will form for $l < 12$ is in good agreement with the findings of Even et al.,[163] who predicted miniband formation for $l < 12$ using lower effective masses ($0.3\,m_e$ and $0.75\,m_e$). It agrees as well with findings of Ahmad et al.[166] who reported no interlayer coupling for ligand lengths of $l = 12$.
While the calculated results predict very well the trend seen in the experiments, the absolute values of the calculated bandgaps are off by a significant margin. Whereas the calculated values range between 2.65 eV and 2.68 eV, the measured E_{PL} lie between 2.38 eV and 2.52 eV, resulting in a discrepancy of calculation and experiment between 270 meV and 160 meV, respectively. This can be reasonably explained by the fact that transition energies from PL measurements are compared, for which one also has to consider the exciton binding energy.

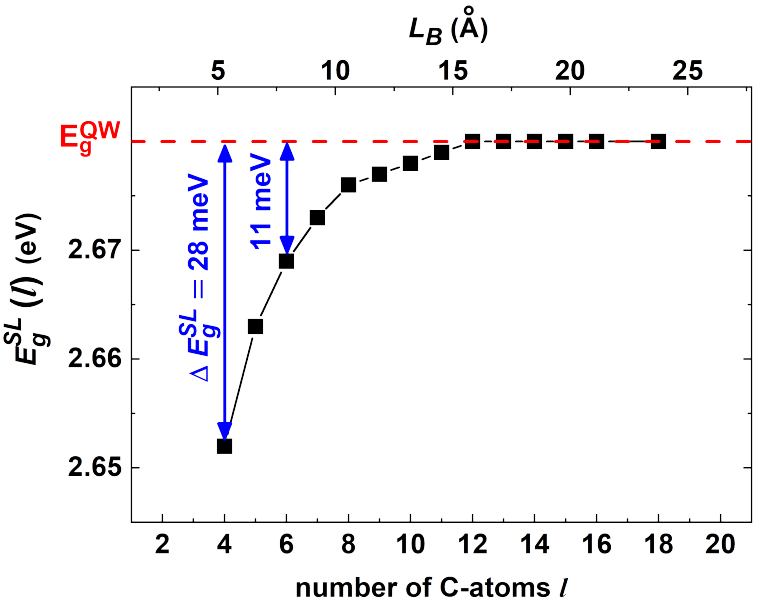

Figure 6.6.: The influence of superlattice effects on the bandgap energy $E_g^{SL}(l)$ depending on the ligand length l are calculated with a Kronig-Penney model. For $l \geq 12$ a constant energy is predicted, resembling to the case of an isolated quantum well. For $l = 4 - 11$ a miniband formation is predicted, leading to a relative decrease of $\Delta E(l) = E_g^{QW} - E_g^{SL}(l)$ of up to 28 meV for the shortest ligand ($l = 4$).

As already mentioned, the exciton binding energies in these confined 2D systems can reach values up to hundreds of meVs, far greater than in bulk crystals.[26,126,150] Experimentally, Hong et al.[7] determined the exciton binding energy of $C_{10}PbI_4$ to account for 320 meV, which is in the right order of magnitude to explain the discrepancy of the calculated $E_g^{SL}(l)$ and measured E_{PL}. The simulations of the miniband formation show that for ligands shorter than $l = 12$ the miniband formation plays an important role. In order to visualize the sole dependence of the tilting angle on PL emission energy, the calculated energy drop due to miniband formation $\Delta E(l)$ are added to the experimentally determined energies E_{PL}. The results are artificially decoupled PL energy values (figure 6.7). A linear fit proves a strong correlation between octahedral tilt and E_{PL}, where all data points align nicely on the fitted line. This suggests that the observed deviations for $l < 12$ from this linearity, as seen in figure 6.4, are due to miniband formation. Thus, the two effects together, octahedral tilt and electronic coupling, can explain the transition energies observed in layered hybrid perovskites very accurately.

One must note that Even et al.[163] suggest that the EMA approach might be invalid for ultrathin perovskite layers due to nonparabolicity of the Bloch function of the VB and CB. A parabolic function, however, is a fundamental requirement for the Kronig-Penney model. Accordingly, Even et al. proposed an alternative model based on concepts from

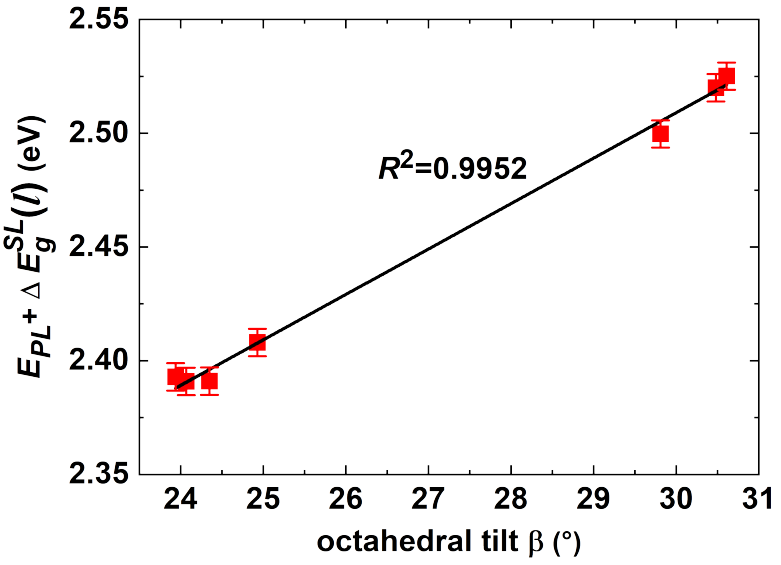

Figure 6.7.: Impact of octahedral tilt and miniband formation. In order to see the sole dependency of the tilting angle on the PL emission energy, the data points of the measured PL emission energy E_{PL} are artificially decoupled by adding the calculated energy drop due to miniband formation $\Delta E(l)$. The result exhibits a much stronger correlation with the octahedral tilt angle than the pure E_{PL} values with $R^2 = 0.9952$. This leads to the conclusion that combining the two effects, octahedral tilting and miniband formation, allows a very accurate explanation of the observed E_{PL} in layered hybrid perovskites.

composite materials and density functional theory calculations (DFT). However, in parallel to this work, Traore et al.[148] performed DFT simulations for C_lPbI_4 including SOC corrections. The results are depicted in the appendix figure A.11, together with the experimental results acquired in this thesis. As DFT is known to underestimate the bandgap[46], only the trend in bandgap predicted by Traore et al. is discussed here. Similar to observations in this thesis, the authors find a strong correlation between tilt angle and bandgap. Interestingly, when comparing the predicted bandgap and the measured emission wavelength, for the samples C_4PbI_4 and C_6PbI_4 there are stronger deviations and the predictions are too high. Therefore, the tilting angle does not seem sufficient to explain the observed shift in the PL emission data. Consequently, it is concluded here that the transition energies of monolayer perovskites are determined by two factors, the octahedral tilt angle and the degree of miniband formation resulting from electronic coupling between the quantum wells. Although only a small effect due to the high effective masses of the charge carriers, it is currently the only proposed model that can explain the deviations observed for the systems comprising the shortest alkyl chains.

6.4. Chapter summary

In this chapter, the influence of the ligand on the emission energy of layered hybrid perovskites based on C_lPbI_4 with $l = 4, ..., 18$ was investigated. By systematically increasing the length of the ligand l without altering the functional group, all samples were found in orthorhombic crystal structure with only the octahedral tilt angle and the interlayer spacing varying from sample to sample. PL and absorption spectroscopy displayed a jump of 110 meV in optical bandgap between the samples $C_{10}PbI_4$ and $C_{12}PbI_4$. Structure-function analysis revealed octahedral tilting as the dominant factor in this observed shift. For shorter ligands ($l < 12$) an additional effect reduces the bandgap. Here, electronic coupling between the multilayer structure occured, resulting in miniband formation, that further reduces the transition energy. The experimental findings were supported by Kronig-Penney model calculations, which predict a reduction in transition energy of up to 28 meV for the C_4PbI_4 sample. While electronic coupling was found to be only a minor effect, it is currently the only proposed model that can explain the deviations observed for the systems with an interlayer distance smaller than 1.5 nm. The two effects together, octahedral tilt and electronic coupling, can explain the transition energies observed in layered hybrid perovskites very accurately.

7. Conclusion and outlook

In this thesis two-dimensional (2D) lead halide nanostructures were investigated regarding thickness-dependent optical properties, charge carrier dynamics, the impact of structural distortions, and distance-dependent electronic coupling.

It was demonstrated that by controlling the ratio of the organic cations (octylammonium, OA and methylammonium, MA) used in the synthesis, colloidal perovskite nanoplatelets of varying thicknesses could be obtained. With increasing fraction of the large OA cation a thinning of the resulting nanoplatelets was observed down to structures with only one single unit cell in height. From optical spectroscopy measurements, the energetic bandgaps corresponding to perovskite nanoplatelets of 1 to 5 unit cells in thickness were determined. Due to quantum size effects the thinnest structures displayed a photoluminescence (PL) blue-shift of more than 90 nm with respect to the bulk counterpart. Kronig-Penney model calculations were performed allowing a quantitative analysis of the quantum size effects in this material for the first time. For the thinnest structures of 1 and 2 unit cells in height, the surrounding ligand and the stacking of the nanoplatelet were found to have an additional impact on the optical properties. For these samples the exciton binding energy becomes extremely large amounting to several hundreds of meV and partially counteracting the blue-shift occurring due to quantum size effects. Additionally, electronic coupling between platelets likely leads to a further reduction of the bandgap.

Time-resolved PL measurements were performed on films containing nanoplatelets of varying thicknesses. The PL lifetimes were found to decrease with thinner nanoplatelets accompanied by increasing exciton binding energies. For a more detailed understanding of the dependencies involved, the synthesis of substrates containing nanoplatelets monodispersed in size would be necessary.
Exciton-phonon interactions were investigated in $CsPbBr_3$ nanoplatelets with a thickness of 3 unit cells. To this end, temperature-dependent steady-state PL measurements were performed. A theoretical model considering acoustic and optical phonons as the main source for the scattering of the excitons was applied. It revealed that acoustic phonons dominate at temperatures below 90 K, whereas optical phonons dominate above this temperature. The Fröhlich coupling constant $\gamma_{LO} = (66.7 \pm 11.4)$ meV, the coupling constant with acoustic phonons $\gamma_{AC} = (34.2 \pm 8.6)$ µeV/K, and the LO phonon energy

$E_{LO} = (24.9 \pm 5.0)$ meV were determined for these nanoplatelets. There are no established reference values for these measurements as current literature for $CsPbBr_3$ nanocubes gives results of a wide range and there are no reported values for $CsPbBr_3$ nanoplatelets.[66,128] Therefore, no final conclusion can be drawn as to whether the decrease in dimensionality from nanocubes to nanoplatelets leads to an increase or decrease in these parameters. Additional temperature-dependent PL measurements indicated an antiquenching behavior of the luminescence at higher temperatures in these nanoplatelets. This result indicates that the role of the ligands is crucial especially in these structures, which are characterized by a high surface-to-volume ratio. Furthermore, temperature-dependent time-resolved PL measurements revealed contributions of bright and dark excitons to the decay curves below 60 K. In this temperature regime the fast decay of the bright exciton was observed to increase with temperature, while the long-lived decay of the dark exciton shortened. The two components were not distinguishable above 60 K. Up to 140 K the overall lifetime became shorter with temperature. Interestingly, between 140 K and 290 K the overall decay time increased again with temperature. A similar behavior is known from 'classical' semiconductor GaAs quantum wells.[138,139] In the perovskite nanoplatelets, however, this effect was observed at considerably higher temperatures. A likely reason lies in the considerably higher exciton binding energy exceeding 200 meV for the nanoplatelets in comparison to GaAs quantum wells.

To further study miniband formation and its dependence on the interlayer distance, layered hybrid perovskites were investigated. These structures are stacks of perovskite sheets of one single octahedral layer in thickness with organic moieties separating them. The interlayer distance was systematically varied between 7 Å and 25 Å through alkyl chain moieties of differing length. The interlayer distance was found to play a minor role in determining the excitonic PL energy of the layered structures. Instead, the basic structural parameter constituted by the degree of octahedral tilting in the perovskite layers was found to play an important role in determining the emission wavelength. The more the octahedra tilt, the higher the emission energy. Nevertheless, there are strong indications that an additional effect partially counteracts the impact of the octahedral tilting for relatively short interlayer distances. Based on Kronig-Penney model calculations, an energy correction accounting for miniband formation and hence reducing the emission energy was suggested. Interlayer distances up to 15 Å were found to allow miniband formations that led to a further red-shift of the transition energy up to a maximum of 28 meV for the distance of 7 Å.

In conclusion, quantum size effects in lead halide perovskite nanoplatelets were observed and described quantitatively. These thickness-dependent effects can be exploited to design nanocrystals of desired optical properties. For example, their emission wavelength can be

tuned for light-emitting applications through size effects instead of the commonly used ion exchange. In this rapidly developing field of research many perovskite nanocrystals of various compositions and dimensionalities were reported since initial reports in 2014. [25,126,130] However, future research activities have to improve the stability of these materials with regard to ion migration and environmental degradation. First successful encapsulations of nanocrystals in various inorganic matrixes enhancing the stability were reported. [16,167,168] The exciton binding energies and the charge carrier dynamics of perovskite nanoplatelets depend on the thickness of the material, as well. The increase of the exciton binding energy was observed especially for the thinnest nanoplatelets. The excitonic character of the nanoplatelets is ideal for light-emitting applications. Later reports demonstrated the successful implementation of nanocrystals into devices. [169,170,171] These structures possess a high surface-to-volume ratio. Therefore their surface condition and their ligands play a prominent role. The ligands can passivate or induce surface trap states. Thus the ligands affect the photoluminescence quantum yield. Temperature-induced phase transitions of the ligand and induced strain on the nanoplatelet surface can additionally influence the quantum yield as observed in this thesis. Further research activities could gain deeper insight into the role of the ligands regarding their impact on surface defects and nanoplatelet quality.

This thesis showed how the choice of the ligand enables a tuning of the optical bandgap of layered hybrid perovskites. It was described that the ligands influence the crystal structures of the perovskite sheets. That strongly affects the optical band gap of the material. This dependence can be exploited for the design of nanostructures with specifically tailored properties for optoelectronic applications. The material can be implemented together with 3D perovskites into solar cell devices. These 2D/3D devices showed improved stability towards environmental degradation and obtained considerable photovoltaic efficiencies of up to 14.6 %. [14,172]

The promising results of this PhD thesis have been communicated in scientific journals as listed in *Publications*. The interest of the research community in bulk perovskite and perovskite nanocrystals is unbroken as one can see from the high number of publications on the topic. There are already first start-ups for perovskite solar cell applications. [173] It is not possible to predict if lead halide perovskite will become a commonly used material for industrial products, though currently it seems a very promising material.

A. Appendix

A.1. Quantum yield of $MAPbBr_3$ nanoplatelets

Sample	PLQY Φ_{PL}
0 % OA	4.72 %
20 % OA	16.25 %
40 % OA	16.55 %
60 % OA	22.56 %
70 % OA	30.31 %
80 % OA	12.47 %
90 % OA	2.81 %
100 % OA	0.43 %

Table A.1.: Photoluminescence quantum yield (PLQY) of perovskite suspensions for various suspensions of $MAPbBr_3$ nanoplatelets with differing OA content.

A.2. XRD on $MAPbBr_3$: reflection multiplicity

For the cubic $Pm\bar{3}m$ symmetry group, the multiplicity of each peak is less or equal to 48. $hkl \equiv -hkl \equiv h-kl \equiv hk-l \equiv -h-k-l \equiv h-k-l \equiv -hk-l \equiv -h-kl \equiv klh \equiv -klh \equiv k-lh \equiv kl-h \equiv -k-l-h \equiv k-l-h \equiv -kl-h \equiv -k-lh \equiv lhk \equiv -lhk \equiv l-hk \equiv lh-k \equiv -l-h-k \equiv l-h-k \equiv -lh-k \equiv -l-hk \equiv khl \equiv -khl \equiv k-hl \equiv kh-l \equiv -k-h-l \equiv k-h-l \equiv -kh-l \equiv -k-hl \equiv lkh \equiv -lkh \equiv l-kh \equiv lk-h \equiv -l-k-h \equiv l-k-h \equiv -lk-h \equiv -l-kh \equiv hlk \equiv -hlk \equiv h-lk \equiv hl-k \equiv -h-l-k \equiv h-l-k \equiv -hl-k \equiv -h-lk$
The multiplicity of the (100), (111), (200), and (210) planes are shown in figure A.1. The fraction of planes giving reflections with out-of-plane contribution is indicated, as well.

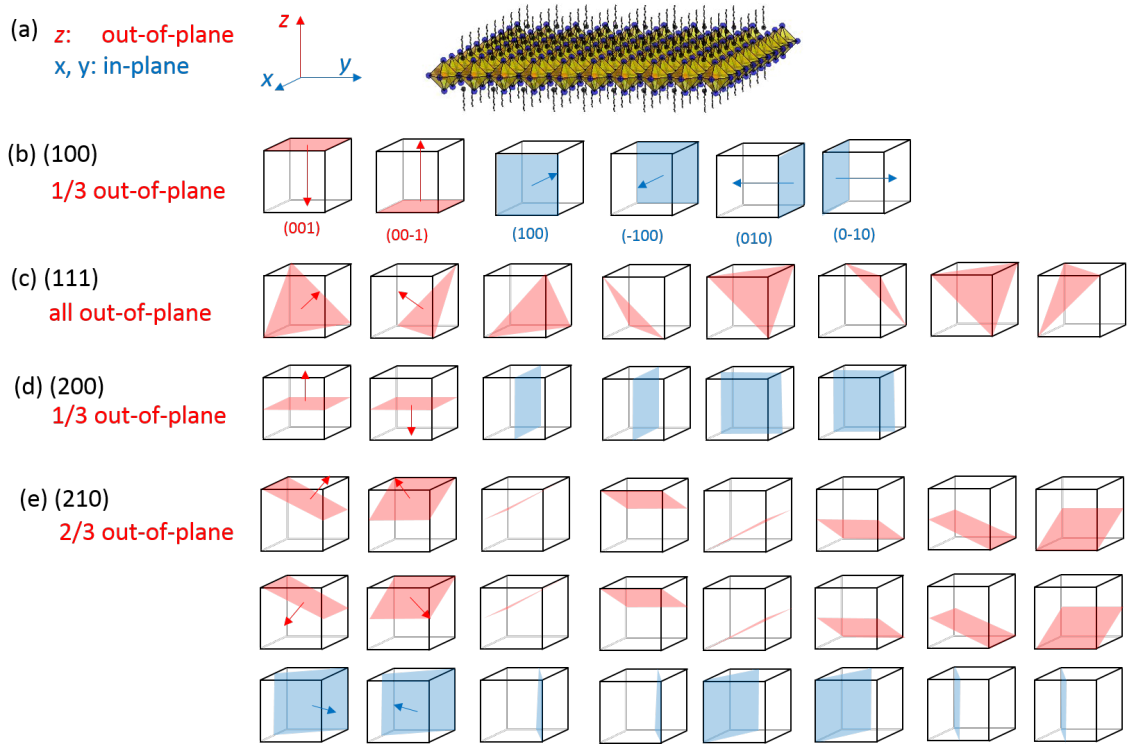

Figure A.1.: Multiplicity of diffraction peaks. (a) Sketch of a nanoplatelet and in respect to it in-plane directions (blue) and out-of-plane directions (red). (b) (100) has a multiplicity of 6. 4 planes (red) give reflections with out-of-plane contribution, that is a fraction of 1/3. (c) (111) has a multiplicity of 8. All of these planes (red) give reflections with out-of-plane contribution. (d) (200) has a multiplicity of 6. 2 planes (red) give reflections with out-of-plane contribution, that is a fraction of 1/3. (e) (210) has a multiplicity of 24. 16 planes (red) give reflections with out-of-plane contribution, that is a fraction of 2/3.

A.3. EDX of degraded $MAPbBr_3$ nanoplatelets

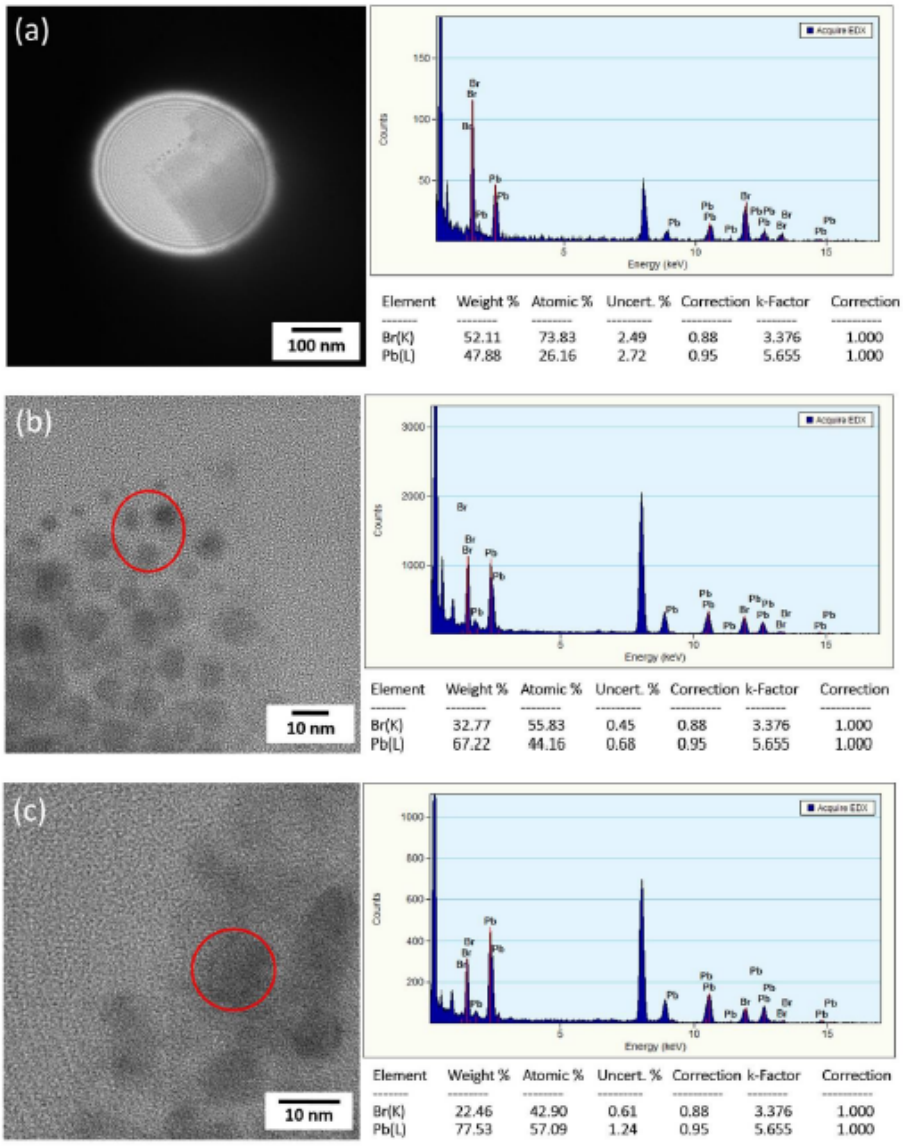

Figure A.2.: HRTEM images and corresponding EDX spectra for different observed nanostructures. Reprinted with permission from Sichert et al. [150]. Copyright 2015 American Chemical Society.

A.4. Calculation of the exciton Bohr radii of $MAPbBr_3$ and $MAPbI_3$

Using equation 2.17, the exciton Bohr radius in $MAPbBr_3$ and $MAPbI_3$ can be estimated with
$\mu = \left(\frac{1}{0.23\,m_0} + \frac{1}{0.29\,m_0}\right)^{-1} = 0.22\,m_0$ as:

$$a_B = \frac{\epsilon}{\epsilon_0}\frac{m_0}{\mu}a_H = \frac{3.29}{1}\cdot\frac{9.11\cdot10^{-31}\,\mathrm{kg}}{0.22\cdot9.11\cdot10^{-31}\,\mathrm{kg}}0.529177\cdot10^{-10}\,\mathrm{m} = 1.36\cdot10^{-9}\,\mathrm{m} \quad (1.1)$$

and

$$a_B = \frac{\epsilon}{\epsilon_0}\frac{m_0}{\mu}a_H = \frac{6.5}{1}\cdot\frac{9.11\cdot10^{-31}\,\mathrm{kg}}{0.12\cdot9.11\cdot10^{-31}\,\mathrm{kg}}0.529177\cdot10^{-10}\,\mathrm{m} = 2.87\cdot10^{-9}\,\mathrm{m}. \quad (1.2)$$

A.5. Kronig-Penney model calculations for $MAPbBr_3$ platelets

For the model calculations equations 2.8 to 2.11 are used. The used parameters are $E_g^{3D} = 2.38\,\mathrm{eV}$, $V_{VB} = 2.9\,\mathrm{eV}$, $V_{CB} = 0.9\,\mathrm{eV}$, $L_{QW} = n\cdot 6\,\text{Å}$, with n an integer, and $L_B = 10\,\text{Å}$.

layer thickness n	E_{PL} (nm) from experiment	E_{PL} (eV) from experiment	E_{PL} (eV) calculated with Kronig-Penney
1	427 nm	2.90 eV	3.52 eV
2	454 nm	2.73 eV	2.80 eV
3	469 nm	2.64 eV	2.63 eV
4	482 nm	2.57 eV	2.56 eV
5	490 nm	2.53 eV	2.53 eV
6	-	-	2.51 eV
7	-	-	2.49
8	-	-	2.48 eV
9	-	-	2.48 eV
10	-	-	2.48 eV
∞ (cubes)	520 nm	2.38 eV	2.38 eV

Table A.2.: Measured E_{PL} and modeled transition energy according to Kronig-Penney model. For $n > 10$ the curve is too flat and important parameters are not known accurately enough so that the emission of 2.45 meV observed in the 60 % OA with the streak camera (figure 5.1 b, c) cannot be assigned to a certain number of unit cells thickness. The discrepancy of E_{PL} and E_X for $n = 1, 2$ is attributed to an exciton binding energy accounting for about 600 meV and 170 meV, respectively, in these samples.

A.6. Quantum size effects in $MAPbI_3$ nanoplatelets

Quantum size effect in $MAPbI_3$ nanoplatelets with octylammonium ligand

Colloidal $MAPbI_3$ nanoplatelets were achieved with a synthesis similar to the synthesis of $MAPbI_3$ nanoplatelets presented in chapter 4. The observed PL peaks at 606 nm - 608 nm stem from trilayer ($n = 3$) nanoplatelets and the peak at 540 nm from monolayers ($n = 1$), respectively.[126,174] The washing cycles carried out during the synthesis lead to very polydisperse solutions. Better results were achieved without the washing cycles as described below.

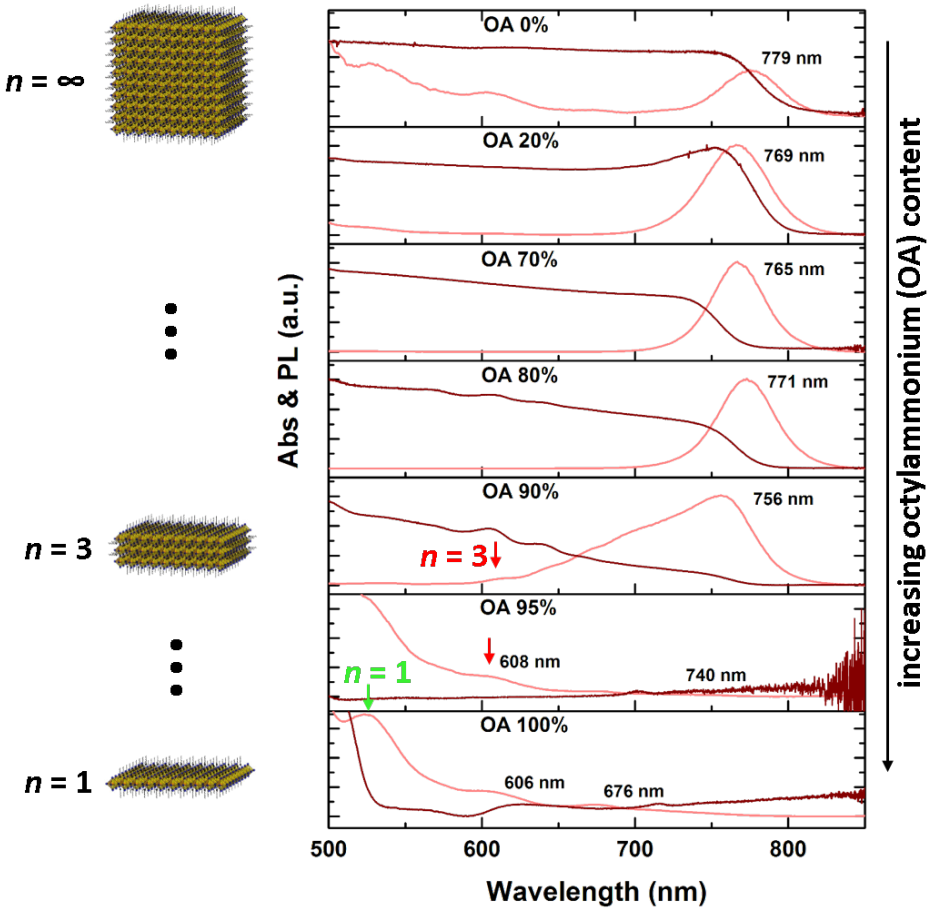

Figure A.3.: Quantum size effect in $MAPbI_3$ nanoplatelets. PL (rose) and absorption (red) spectra of $MAPbI_3$ nanoplatelets of varying OA concentration. PL peak located at 606 nm - 608 nm stem from trilayer ($n = 3$) nanoplatelets and the peaks at 540 nm from monolayers ($n = 1$).

Quantum size effect in $MAPbI_3$ nanoplatelets with oleylammonium ligand

As explained in detail in subsection 2.2.2, an exchange of the halide ion provides a simple way to tune the emission wavelength of halide perovskites. Here, iodide was used instead of bromide and oleylammonium instead of octylammonium (OL). In contrast to the syntheses of nanoplatelets described in subsection 3.1.1 and above, the washing cycles were not carried out here. The ratio of OL to MA was varied. Figure A.4 displays the PL and absorption spectra of two samples containing OL 90 % (green) and OL 85 % (yellow). As a result, the obtained product is less polydisperse than the sample of OA 90 % in figure A.3. According to calculations by Wu et al.[174] and Hintermayr et al.[126], these peaks stem from $MAPbI_3$ nanoplatelets of $n = 1$ and $n = 2$ layers of thickness. However, the broadness of the peak suggests that both suspensions contain also small fractions of nanoplatelets of thicker structures.

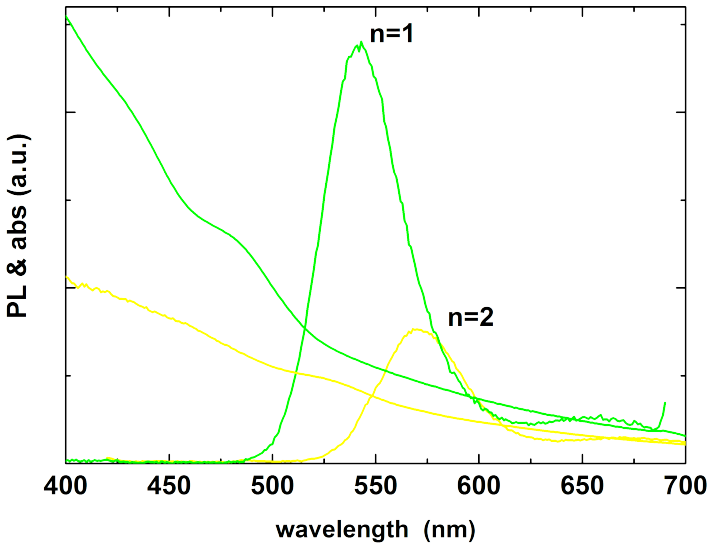

Figure A.4.: PL and absorption spectra of $MAPbI_3$ nanoplatelet suspensions with oleylamine ligands. Solution synthesis without centrifuging. Varying ratio solvent to antisolvent.

A.7. Thickness-dependent time-resolved PL spectroscopy of $MAPbI_3$ nanoplatelets

Figure A.5 a displays the streak image recorded on a perovskite suspension containing $MAPbI_3$ nanoplatelets that are polydisperse regarding their thicknesses. As discussed in the previous chapters and from references Wu et al.[174] and Hintermayr et al.[126], it is known that platelets of $n = 1, 2$, and 3 unit cells in thickness have their emission maxima at approximately 540 nm, 580 nm, and 610 nm, respectively. Hence, the PL counts around these wavelengths are attributed to charge carrier recombinations in platelets of $n = 1, 2$, and 3 layers in thickness.

To extract the decay curves of nanoplatelets of these thicknesses separately, the PL counts at these wavelengths are plotted versus time (Figure A.5 c). The lifetime was found to increase with temperature. The trend is in good agreement with observations made by Hintermayr et al.[126]

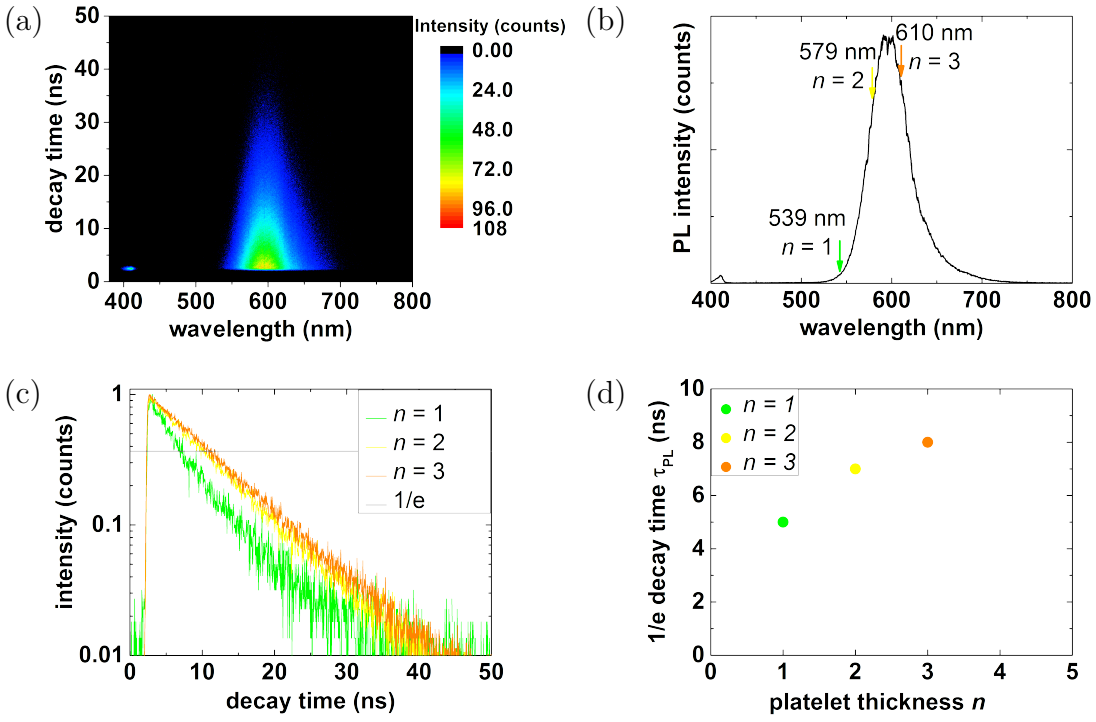

Figure A.5.: (a) Streak image taken of a polydisperse $MAPbI_3$ suspension containing nanoplatelets of various thicknesses. (b) PL spectrum with PL peak at 600 nm obtained by integrating the streak image over time from 0 ns to 50 ns. (c) Decay curves extracted from the streak image around 540 nm, 580 nm, and 610 nm, attributed to charge carrier recombination in platelets of $n = 1, 2$, and 3 unit cells of thickness, respectively. (d) 1/e decay constants τ_{PL} for nanoplatelets of $n = 1, 2$, and 3 unit cells thickness extracted from (c).

A.8. Lifetimes in $CsPbBr_3$ nanoplatelets

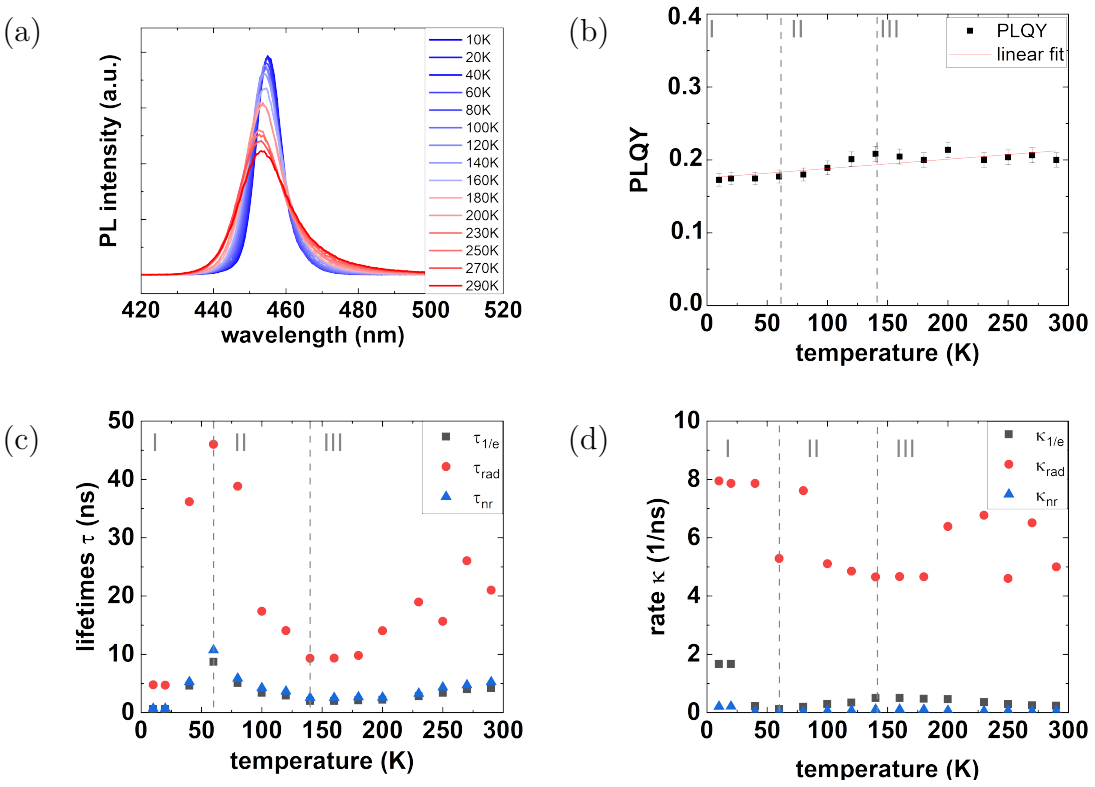

Figure A.6.: Further analyses of $CsPbBr_3$ nanoplatelets regarding PL and carrier recombination dynamics. (a) Original PL spectra recorded for different temperature over nm. (b) PLQY calculated from the integral of the PL spectra according to equation 5.6. (c) Radiative, non-radiative, and 1/e lifetimes extracted from figures 5.3 a to 5.3 c. (d) Radiative and non-radiative rates calculated from (c).

A.9. Exciton-phonon interactions and PL lifetimes in $CsPbX_3$ nanocubes

PL lifetimes in $CsPbX_3$ nanocubes at room temperature

The here investigated samples are colloidal $CsPbX_3$ nanocubes with three different halides, X=I, Br, Cl. The samples were prepared by Dr. Yu Tong. The observed trends in steady-state and time-resolved PL are similar to those observed by Saran et al.[66] and Diroll et al.[128] published in parallel to the work shown here.

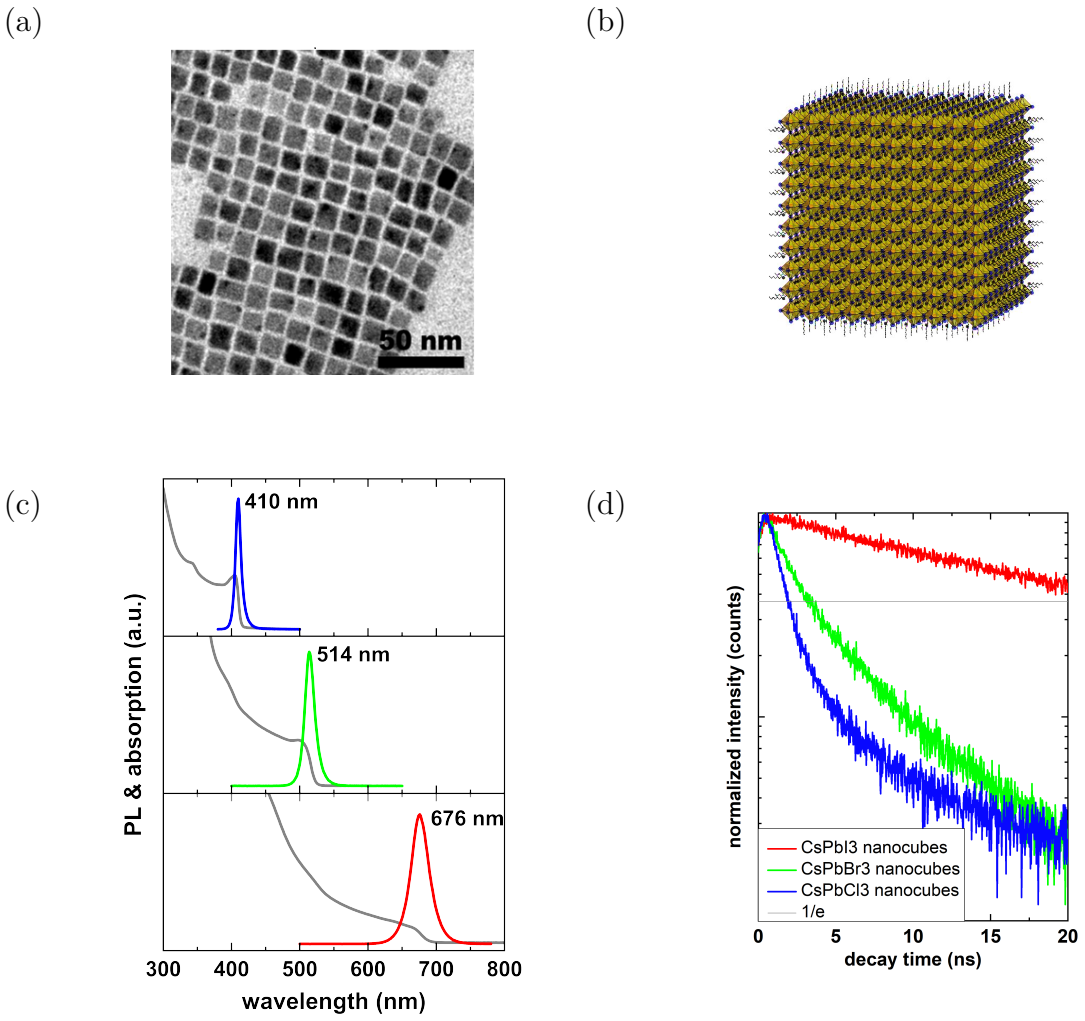

Figure A.7.: Structural and optical characterization of $CsPbX_3$ nanocubes. (a) TEM image of $CsPbBr_3$ nanocubes showing rectangular structures of 8-12 nm lateral size. (b) Sketch of a nanocube with octahedra of the unit cell and surrounding organic ligands. (c) Steady-state absorption and PL showing a blue-shift from I to Br to Cl. (d) Time-resolved photoluminescence showing a decrease in lifetime with smaller halide ion and higher exciton binding energy.

Sample	Crystal size	r_{Bohr} [110]	$PLQY_{colloidal}$	$PLQY_{substrate}$	PL peak	$\tau_{1/e}$
$CsPbI_3$	8-12 nm	5 nm	58 %	46 %	676 nm	22 ns
$CsPbBr_3$	8-12 nm	7 nm	42 %	37 %	514 nm	5 ns
$CsPbCl_3$	10-15 nm	12 nm	8 %	2 %	410 nm	3 ns

Table A.3.: Structural and optical parameters of $CsPbX_3$ nanocubes.

Temperature-dependent PL lifetimes of $CsPbX_3$ nanocubes

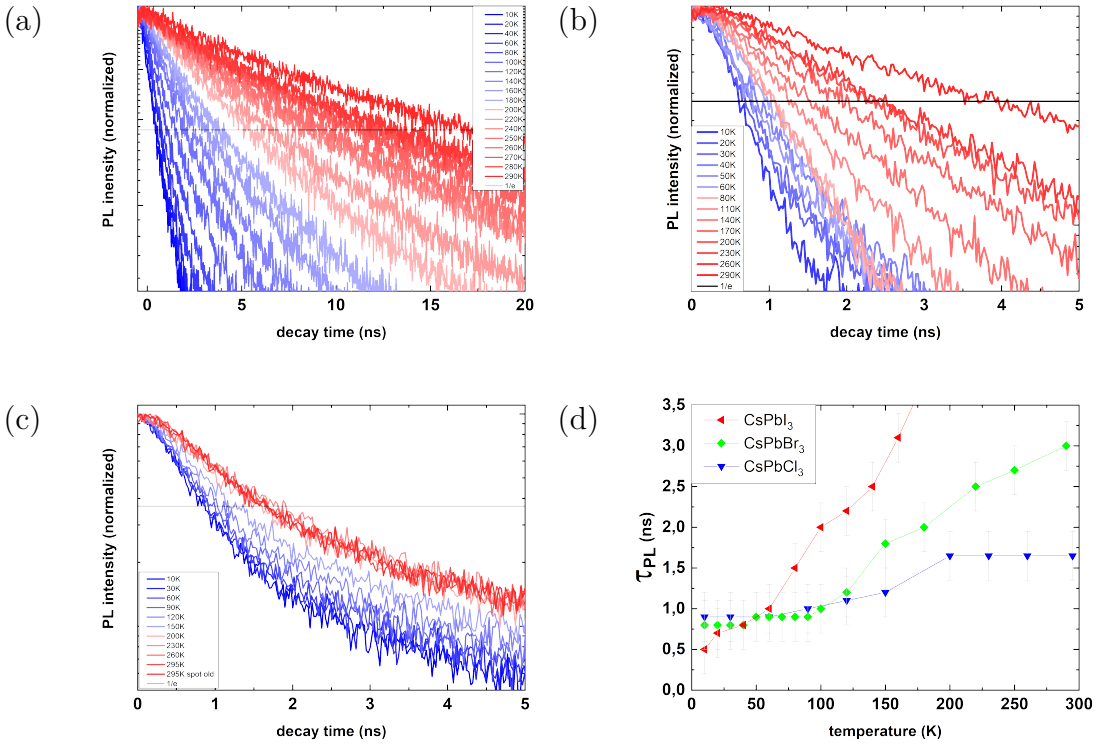

Figure A.8.: Time-resolved photoluminescence lifetimes of $CsPbX_3$ nanocubes at temperatures between 10 K and 290 K. (a) $CsPbI_3$ nanocubes. (b) $CsPbBr_3$ nanocubes. (c) $CsPbCl_3$ nanocubes. (d) Lifetimes $\tau_{PL} = \tau_{1/e}$ extracted from (a) to (c).

Sample	Γ_{inh} (meV)	γ_{AC} (µeV/K)	γ_{LO} (meV)	E_{LO} (meV)
$CsPbI_3$ cubes	22.2 ±1.4	96.7 ±25.9	129 ±50	42.4± 12.1
$CsPbBr_3$ cubes	22.0 ± 0.3	60.0 ± 4.2	284 ± 26	55.0± 3.2
$CsPbCl_3$ cubes	43.6 ± 0.6	31.2 ± 14.5	66.4 ± 13	32.7± 6.6
$CsPbI_3$ [128] cubes	52.12 ±0.71	24.17 ±21.96	46.13 ±11.10	26.25± 6.96
$CsPbBr_3$ [128] cubes	40.04 ± 0.45	33.05 ± 11.07	86.72 ± 31.40	44.35± 10.19
$CsPbCl_3$ [128] cubes	67.18 ± 0.27	43.14 ±5.50	87.22 ± 14.9	42.82± 4.45
$CsPbI_3$ [66] cubes	39	10	44	16
$CsPbBr_3$ [66] cubes	20	5	45 31.40	16
$CsPbCl_3$ [66] cubes	30	34	85	46
$MAPbI_3$ platelets [175]	22 ±1	-	95 ± 28	21 ± 3

Table A.4.: Tabular representation of fit results and literature values.

Exciton-phonon coupling in $CsPbX_3$ nanocubes

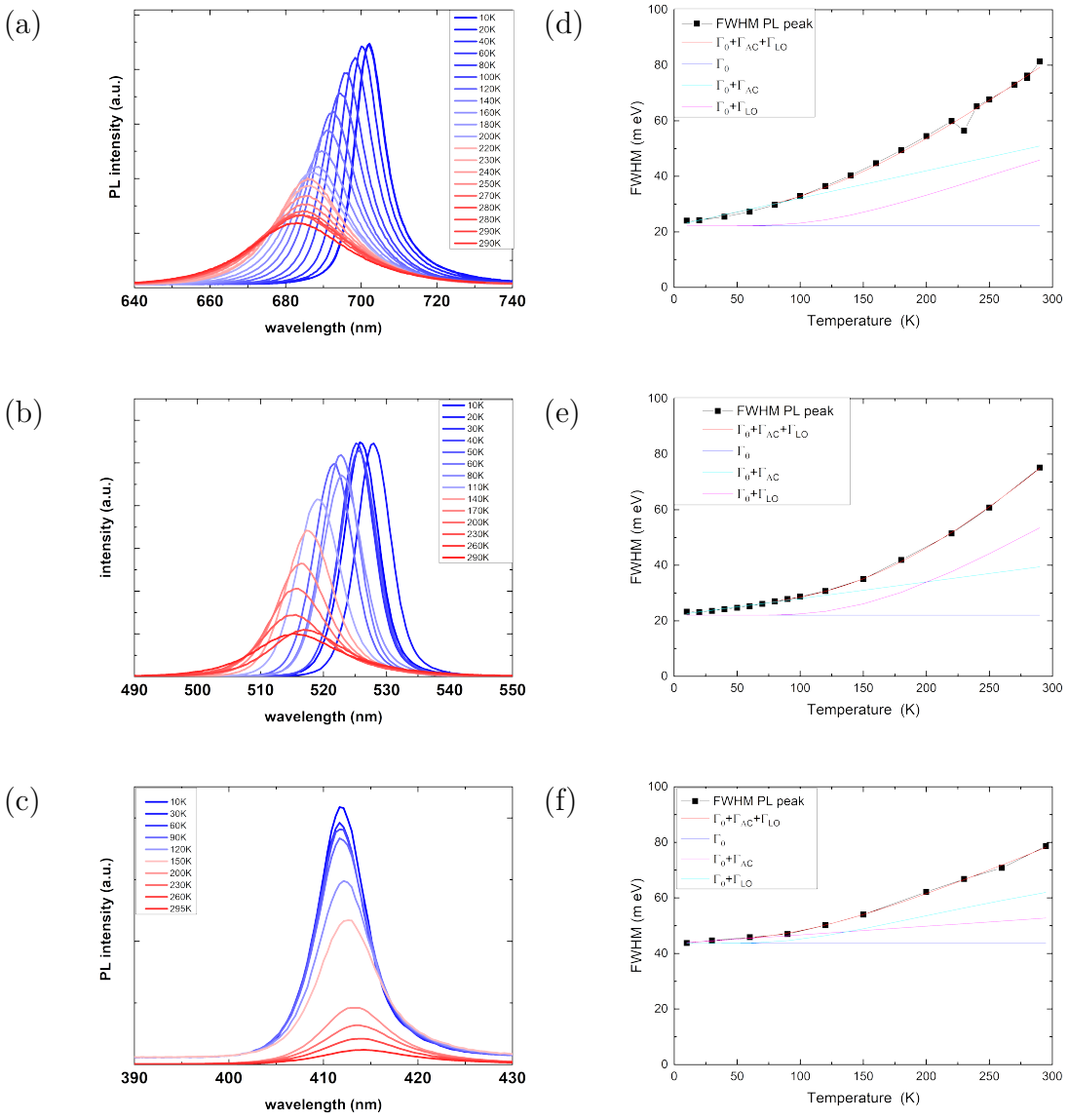

Figure A.9.: PL spectra and fits of FWHM at different temperatures. (a) to (c) show PL spectra of $CsPbI_3$, $CsPbBr_3$ and $CsPbCl_3$. I and Br red-shift with lower temperature whereas Cl slightly blue-shifts. (d) to (f) exhibit the corresponding FWHM of the spectra and fits according to formula 2.30 tackling exciton-phonon interactions in the samples.

A.10. Orthorhombic to monoclinic phase transition for $C_{12}PbI_4$

At room temperature, $_{12}PbI_4$ is in the orthorhombic phase whereas through heating also a contribution of the monoclinic phase becomes visible. The corresponding PL and XRD spectra are shown in figure A.10. For details see figure caption.

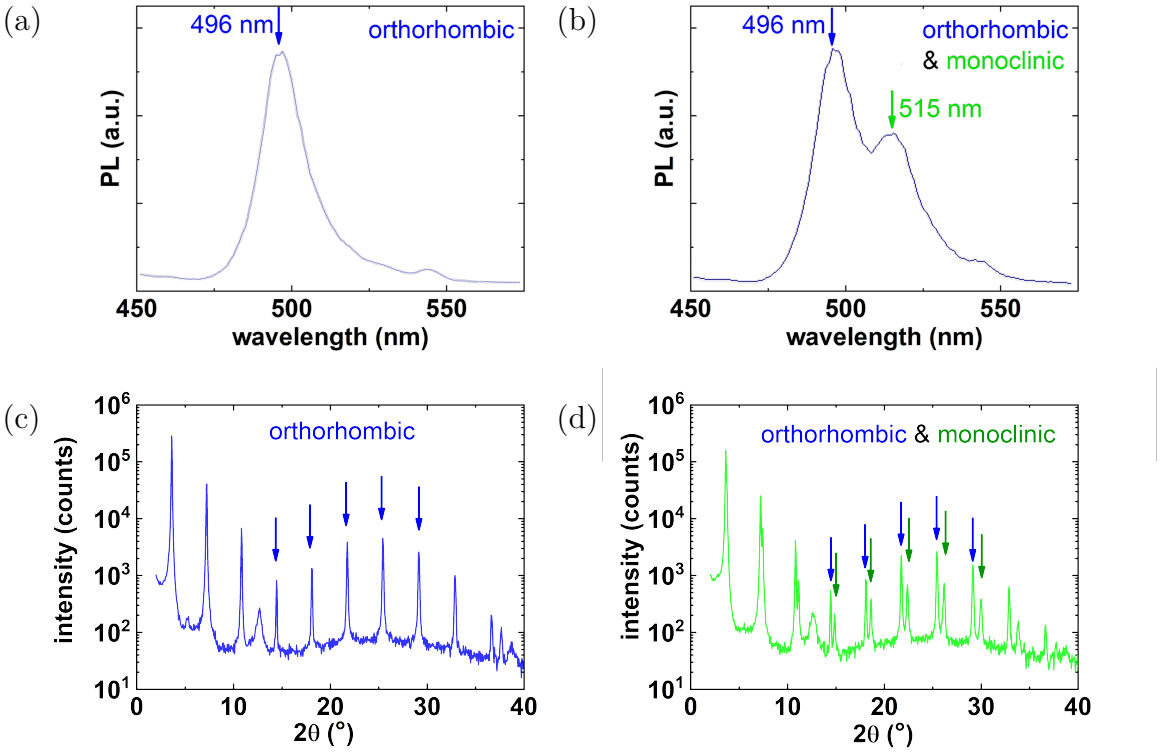

Figure A.10.: XRD and PL spectra for orthorhombic to monoclinic phase transition for $C_{12}PbI_4$. (a) XRD shows only orthorhombic peaks (corresponding to octahedral tilt angle β of 150.19° [86]). (b) XRD shows orthorhombic and monoclinic peaks (corresponding to octahedral tilt angle β of 150.19° [86] and 157.42°). The peak at 545 nm is an artifact, also observed on a blank sample. (c) PL spectrum corresponding to (a) shows single peak at 496 nm. (d) PL spectrum corresponding to (b) shows additional peak at 515 nm. Orthorhombic to monoclinic phase transition for $C_{12}PbI_4$ is accompanied by a shift in emission wavelength of 19 nm. [151]

A.11. Kronig-Penney and DFT for layered hybrid perovskites

For the model calculations equations 2.8 to 2.11 are used.

sample	$\Delta E\,(V_{VB} = 2.9\,\text{eV},\ V_{CB} = 0.9\,\text{eV},\ m_{QW} = 0.5\,m_e,\ m_B = m_e)$
C_4PbI_4	28 meV
C_5PbI_4	17 meV
C_6PbI_4	11 meV
C_7PbI_4	7 meV
C_8PbI_4	4 meV
C_9PbI_4	3 meV
$C_{10}PbI_4$	2 meV
$C_{11}PbI_4$	1 meV
$C_{12}PbI_4$	0 meV
$C_{16}PbI_4$	0 meV
$C_{18}PbI_4$	0 meV

Table A.5.: Summary of the results of the Kronig-Penney model calculations.

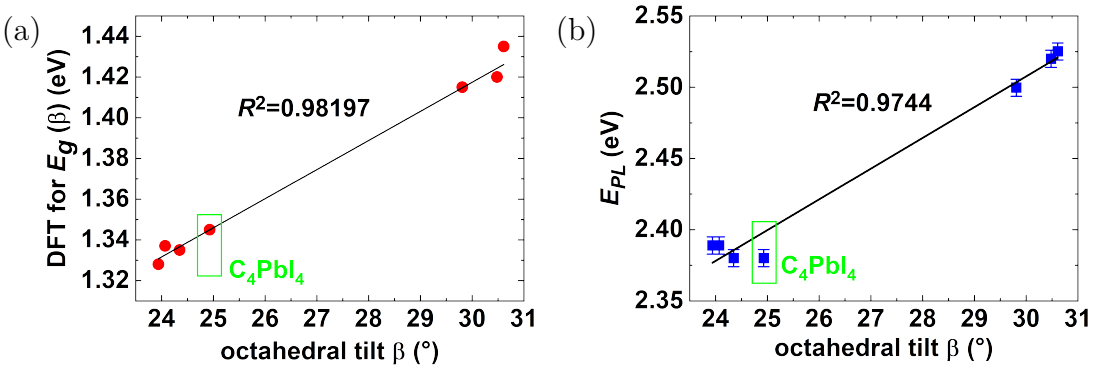

Figure A.11.: (a) Results on DFT including SOC for bandgaps extracted from results of Traore et al.[148] As well-known from DFT, all results underestimate the real bandgaps. The trend bandgap to tilt angle is similar to the experimentally observed one in this work, graphed in (b). However, there is a significant deviation for C_4PbI_4 (C4). This might be due to the fact that miniband formation was not considered in the DFT calculations.

Bibliography

[1] W. Hoffmann: *Perspektiven der Photovoltaik*, Physik Journal **13**, 21 (2014)

[2] www.bundesregierung.de: *Energiewende*, Fassung vom 21.06.2018, Presse- und Informationsamt der Bundesregierung, Berlin (21.06.2018)

[3] C. K. Møller: *Crystal structure and photoconductivity of cæsium plumbohalides*, Nature **182**, 1436 (1958)

[4] H. L. Wells: *Über die Cäsium- und Kalium-Bleihalogenide*, ZAAC **3**, 195 (1893)

[5] C. R. Kagan, D. B. Mitzi, C. D. Dimitrakopoulos: *Organic-inorganic hybrid materials as semiconducting channels in thin-film field-effect transistors*, Science **286**, 945 (1999)

[6] T. Hattori, T. Taira, M. Era, T. Tsutsui, S. Saito: *Highly efficient electroluminescence from a heterostructure device combined with emissive layered-perovskite and an electron-transporting organic compound*, Chem. Phys. Lett. **254**, 103 (1996)

[7] X. Hong, T. Ishihara, A. U. Nurmikko: *Dielectric confinement effect on excitons in PbI_4-based layered semiconductors*, Phys. Rev. B **45**, 6961 (1992)

[8] E. Hanamura, N. Nagaosa, M. Kumagai, T. Takagahara: *Quantum wells with enhanced exciton effects and optical non-linearity*, Mater. Sci. Eng. B **1**, 255 (1988)

[9] A. Kojima, K. Teshima, Y. Shirai, T. Miyasaka: *Organometal halide perovskites as visible-light sensitizers for photovoltaic cells*, J. Am. Chem. Soc. **131**, 6050 (2009)

[10] M. M. Lee, J. Teuscher, T. Miyasaka, T. N. Murakami, H. J. Snaith: *Efficient hybrid solar cells based on meso-superstructured organometal halide perovskites*, Science **338**, 643 (2012)

[11] http://www.nrel.gov/pv/: National Center for Photovoltaics (08.12.2018)

[12] F. Hao, C. C. Stoumpos, D. H. Cao, R. P. H. Chang, M. G. Kanatzidis: *Lead-free solid-state organic-inorganic halide perovskite solar cells*, Nat. Photonics **8**, 489 (2014)

[13] S. Shao, J. Liu, G. Portale, H.-H. Fang, G. R. Blake, G. H. ten Brink, L. J. A. Koster, M. A. Loi: *Highly reproducible Sn-based hybrid perovskite solar cells with 9 % efficiency*, Adv. Energy Mater. **8**, 1702019 (2018)

[14] G. Grancini, C. Roldan-Carmona, I. Zimmermann, E. Mosconi, X. Lee, D. Martineau, S. Narbey, F. Oswald, F. De Angelis, M. Grätzel, Mohammad Khaja Nazeeruddin: *One-Year stable perovskite solar cells by 2D/3D interface engineering*, Nat. Commun. **8**, 15684 (2017)

[15] Z. Wang, Q. Lin, F. P. Chmiel, N. Sakai, L. M. Herz, H. J. Snaith: *Efficient ambient-air-stable solar cells with 2D–3D heterostructured butylammonium-caesiumformamidinium lead halide perovskites*, Nat. Energy **2**, 17135 (2017)

[16] S. Demchyshyn, J. M. Roemer, H. Groiß, H. Heilbrunner, C. Ulbricht, D. Apaydin, A. Böhm, U. Rütt, F. Bertram, G. Hesser, M. C. Scharber, N. S. Sariciftci, B. Nickel, S. Bauer, E. D. Głowacki, M. Kaltenbrunner: *Confining metal-halide perovskites in nanoporous thin films*, Sci. Adv. **3**, e1700738 (2017)

[17] Z. K. Tan, R. S. Moghaddam, M. L. Lai, P. Docampo, R. Higler, F. Deschler, M. Price, A. Sadhanala, L. M. Pazos, D. Credgington, F. Hanusch, T. Bein, H. J. Snaith, R. H. Friend: *Bright light-emitting diodes based on organometal halide perovskite*, Nat. Nanotechnol. **9**, 687 (2014)

[18] L. S. Schmidt, A. Pertegas, S. Gonzalez-Carrero, O. Malinkiewicz, S. Agouram, G. M. Minguez Espallargas, H. J. Bolink, R. E. Galian, J. Pérez-Prieto: *Nontemplate synthesis of $CH_3NH_3PbBr_3$ perovskite nanoparticles*, J. Am. Chem. Soc. **136**, 850 (2014)

[19] C. Kittel, S. Hunklinger: *Einführung in die Festkörperphysik*, Oldenbourg, München, 15th edition (2013)

[20] A. P. Alivisatos: *Semiconductor clusters, nanocrystals, and quantum dots*, Science **271**, 933 (1996)

[21] D. Bimberg, M. Grundmann, N. N. Ledentsov: *Quantum dot heterostructures*, Wiley, Sussex, 1st edition (1999)

[22] V. N. Lutskii: *Quantum size effect - present state and perspectives of experimental investigations*, Phys. Status Solidi A **1**, 199 (1970)

[23] T. Ishihara, J. Takahashi, T. Goto: *Exciton state in two-dimensional perovskite semiconductor $(C_{10}H_{21}NH_3)_2PbI_4$*, Solid State Commun. **69**, 933 (1989)

[24] P. Avouris, T. F. Heinz, T. Low: *2D Materials*, Cambridge University Press, Cambridge, 1st edition (2017)

[25] H. Huang, L. Polavarapu, J. A. Sichert, A. S. Susha, A. S. Urban, A. L. Rogach: *Colloidal lead halide perovskite nanocrystals: synthesis, optical properties and applications*, NPG Asia Mater. **8**, 328 (2016)

[26] R. R. Guseinov: *Coulomb interaction and excitons in a superlattice*, Phys. Status Solidi B **125**, 237 (1984)

[27] D. J. Griffiths: *Introduction to quantum mechanics*, Pearson Prentice Hall, Upper Saddle River, 2nd edition (2005)

[28] D. B. Mitzi, K. Chondroudis, C. R. Kagan: *Organic-inorganic electronics*, IBM J. Res. Dev. **45**, 29 (2001)

[29] H. T. Grahn: *Semiconductor superlattices: growth and electronic properties*, World Scientific Publishing Company, Salem (1995)

[30] A. Chernikov, T. C. Berkelbach, H. M. Hill, A. Rigosi, Y. Li, O. Burak Aslan, D. R. Reichman, M. S. Hybertsen, T. F. Heinz: *Exciton binding energy and nonhydrogenic Rydberg series in monolayer WS_2*, PRL **113**, 076802 (2014)

[31] J. S. Manser, J. A. Christians, P. V. Kamat: *Intriguing optoelectronic properties of metal halide perovskites*, Chemical Reviews **116**, 12956 (2016)

[32] L. V. Keldysh: *Coulomb interaction in thin semiconductor and semimetal films*, JETP Lett. **29**, 658 (1979)

[33] E. Hanamura, N. Nagaosa, M. Kmagai, T. Takagahara: *Quantum wells with enhanced exciton effects and optical non-linearity*, Mater. Sci. Eng. B **1**, 255 (1988)

[34] I. B. Koutselas, L. Ducasse, G. C. Papavassiliou: *Electronic properties of three- and low-dimensional semiconducting materials with Pb halide and Sn units*, J. Phys. Condens. Matter **8**, 1217 (1996)

[35] P. Harrison: *Quantum wells, wires, and dots: theoretical and computational physics of semiconductor nanostructures*, Wiley, Hoboken, 2nd edition (2005)

[36] G. Rose: *De novis quibusdam fossilibus quae in Montibus Uraliis inveniuntur: De perowskite, fossili novo*, AG Schade, Berlin (1839)

[37] C. C. Stoumpos, M. G. Kanatzidis: *The renaissance of halide perovskites and their evolution as emerging semidonductors*, Acc. Chem. Res. **48**, 2791 (2015)

[38] V. M. Goldschmidt: *Die Gesetze der Krystallochemie*, Sci. Nat. **14**, 477 (1926)

[39] M. Shirayama, H. Kadowaki, T. Miyadera, T. Sugita, M. Tamakoshi, M. Kato, T. Fujiseki, D. Murata, S. Hara, T. N. Murakami, S. Fujimoto, M. Chikamatsu, H. Fujiwara: *Optical transitions in hybrid perovskite solar cells: ellipsometry, density functional theory, and quantum efficiency analyses for $CH_3NH_3PbI_3$*, Phys. Rev. Appl. **5**, 014012 (2016)

[40] D. Weber: *$CH_3NH_3PbX_3$, ein Pb(II)-System mit kubischer Perowskitstruktur*, Z. Naturforsch., B: J. Chem. Sci. **33b**, 1443 (1978)

[41] G. Giorgi, J.-I. Fujisawa, H. Segawa, K. Yamashita: *Small photocarrier effective masses featuring ambipolar transport in methylammonium lead iodide perovskite: a density functional analysis*, J. Phys. Chem. Lett. **4**, 4213 (2013)

[42] E. Mosconi, P. Umari, F. De Angelis: *Electronic and optical properties of $MAPbX_3$ perovskites (X= I, Br, Cl): a unified DFT and GW theoretical analysis*, Phys. Chem. Chem. Phys. **18**, 27158 (2016)

[43] M. R. Filip, G. E. Epero, H. J. Snaith, F. Giustino: *Steric engineering of metal-halide perovskites with tunable optical band gaps*, Nat. Commun. **5**, 5757 (2014)

[44] F. Brivio, A. B. Walker, A. Walsh: *Structural and electronic properties of hybrid perovskites for high-efficiency thin-film photovoltaics from first-principles*, APL Mater. **1**, 042111 (2013)

[45] J. Im, C. C. Stoumpos, H. Jin, A. J. Freeman, M. G. Kanatzidis: *Antagonism between spin-orbit coupling and steric effects causes anomalous band gap evolution in the perovskite photovoltaic materials $CH_3NH_3Sn_{1-x}Pb_xI_3$*, J. Phys. Chem. Lett. **6**, 3503 (2015)

[46] T. Umebayashi, K. Asai, T. Kondo, A. Nakao: *Electronic structures of lead iodide based low-dimensional crystals*, Phys. Rev. B **67**, 155405 (2003)

[47] M. D. Smith, E. J. Crace, A. Jaffe, H. I. Karunadasa: *The diversity of layered halide perovskites*, Annu. Rev. Mater. Res. **48**, 111 (2018)

[48] J.-H. Lee, N. C. Bristowe, J. H. Lee, S.-H. Lee, P. D. Bristowe, A. K. Cheetham, H. Myung Jang: *Resolving the physical origin of octahedral tilting in halide perovskites*, Chem. Mater. **28**, 4259 (2016)

[49] N. Onoda-Yamamuro, O. Yamamuro, T. Matsuo, H. Suga: *p-T phase relations of $CH_3NH_3PbX_3$ (X = Cl, Br, I) crystals*, J. Phys. Chem. Solids **53**, 277 (1992)

[50] Y. Lee, D. B. Mitzi, P. W. Barnes, T. Vogt: *Pressure-induced phase transitions and templating effect in three-dimensional organic-inorganic hybrid perovskites*, Phys. Rev. B **68**, 020103 (2003)

[51] I. P. Swainson, R. P. Hammond, C. Soullière, O. Knop, W. Massa: *Phase transitions in the perovskite methylammonium lead bromide, $CH_3ND_3PbBr_3$*, J. Solid State Chem. **176**, 97 (2003)

[52] P. S. Whitfield, N. Herron, W. E. Guise, K. Page, Y. Q. Cheng, I. Milas, M. K. Crawford: *Structures, phase transitions and tricritical behavior of the hybrid perovskite methyl ammonium lead iodide*, Sci. Rep. **6**, 35685 (2016)

[53] T. Baikie, Y. Fang, J. M. Kadro, M. Schreyer, F. Wei, S. G. Mhaisalkar, M. Grätzel, T. J. White: *Synthesis and crystal chemistry of the hybrid perovskite $(CH_3NH_3)PbI_3$ for solid-state sensitised solar cell applications*, J. Mater. Chem. A **1**, 5628 (2013)

[54] J. Even, L. Pedesseau, C. Katan, M. Kepenekian, J.-S. Lauret, D. Sapori, E. Deleporte: *Solid state physics perspective on hybrid perovskite semiconductors*, J. Phys. Chem. C **119**, 10161 (2015)

[55] L. Protesescu, S. Yakunin, M. I. Bodnarchuk, F. Krieg, R. Caputo, C. H. Hendon, R. X. Yang, A. Walsh, M. V. Kovalenko: *Nanocrystals of cesium lead halide perovskites ($CsPbX_3$, $X = Cl$, Br, and I): Novel optoelectronic materials showing bright emission with wide color gamut*, Nano Lett. **15**, 3692 (2015)

[56] A. Swarnkar, R. Chulliyil, V. K. Ravi, M. Irfanullah, A. Chowdhury, A. Nag: *Colloidal $CsPbBr_3$ perovskite nanocrystals: luminescence beyond traditional quantum dots*, Angew. Chemie **127**, 15644 (2015)

[57] S.-H. Wei, A. Zunger: *Predicted band-gap pressure coefficients of all diamond and zinc-blende semiconductors: Chemical trends*, Phys. Rev. B **60**, 5404 (1999)

[58] J. Bardeen, W. Shockley: *Deformation potentials and mobilities in non-polar crystals*, Phys. Rev. **80**, 72 (1950)

[59] J. M. Frost, K. T. Butler, F. Brivio, C. H. Hendon, M. van Schilfgaarde, A. Walsh: *Atomistic origins of high-performance in hybrid halide perovskite solar cells*, Nano Lett. **14**, 2584 (2014)

[60] C. D. Bailie, M. G. Christoforo, J. P. Mailoa, A. R. Bowring, E. L. Unger, W. H. Nguyen, J. Burschka, N. Pellet, J. Z. Lee, M. Grätzel: *Semi-transparent perovskite solar cells for tandems with silicon and CIGS*, Energy Environ. Sci. **8**, 956 (2015)

[61] Y.-S. Chen, J. S. Manser, P. V. Kamat: *All solution-processed lead halide perovskite-$BiVO_4$ tandem assembly for photolytic solar fuels production*, J. Am. Chem. Soc. **137**, 974 (2015)

[62] J. Luo, J.-H. Im, M. T. Mayer, M. Schreier, M. K. Nazeeruddin, N.-G. Park, S. D. Tilley, H. J. Fan, M. Grätzel: *Water photolysis at 12.3 % efficiency via perovskite photovoltaics and earth-abundant catalysts*, Science **345**, 1593 (2014)

[63] Gurudayal, D. Sabba, M. H. Kumar, L. H. Wong, J. Barber, M. Grätzel, N. Mathews: *Perovskite-hematite tandem cells for efficient overall solar driven water splitting*, Nano Lett. **15**, 3833 (2015)

[64] G. Maculan, A. D. Sheikh, A. L. Abdelhady, M. I. Saidaminov, M. A. Haque, B. Murali, E. Alarousu, O. F. Mohammed, T. Wu, O. M. Bakr: *$CH_3NH_3PbCl_3$ single crystals: inverse temperature crystallization and visible-blind UV-photodetector*, J. Phys. Chem. Lett. **6**, 3781 (2015)

[65] W. Demtröder: *Laserspektroskopie 1: Grundlagen*, Springer, Berlin/Heidelberg, 6th edition (2011)

[66] R. Saran, A. Heuer-Jungemann, A. G. Kanaras, R. J. Curry: *Giant bandgap renormalization and exciton–phonon scattering in perovskite nanocrystals*, Adv. Opt. Mater. **5**, 1700231 (2017)

[67] S. Rudin, T. L. Reinecke, B. Segall: *Temperature-dependent exciton linewidths in semiconductors*, Phys. Rev. B **42**, 11218 (1990)

[68] A. D. Wright, C. Verdi, R. L. Milot, G. E. Eperon, M. A. Pérez-Osorio, H. J. Snaith, F. Giustino, M. B. Johnston, L. M. Herz: *Electron–phonon coupling in hybrid lead halide perovskites*, Nat. Comm. **7**, 11755 (2016)

[69] F. Deschler, M. Price, S. Pathak, L. E. Klintberg, D. Jarausch, R. Higler, A. Hüttner, T. Leijtens, S. D. Stranks, H. J. Snaith: *High photoluminescence efficiency and optically pumped lasing in solution-processed mixed halide perovskite semiconductors*, J. Phys. Chem. Lett. **5**, 1421 (2014)

[70] V. D'Innocenzo, G. Grancini, M. J. P. Alcocer, A. R. S. Kandada, S. D. Stranks, M. M. Lee, G. Lanzani, H. J. Snaith, A. Petrozza: *Excitons versus free charges in organo-lead tri-halide perovskites*, Nat. Commun. **5**, 3586 (2014)

[71] M. Saba, M. Cadelano, D. Marongiu, F. Chen, V. Sarritzu, N. Sestu, C. Figus, M. Aresti, R. Piras, A. G. Lehmann: *Correlated electron-hole plasma in organometal perovskites*, Nat. Commun. **5**, 5049 (2014)

[72] J. S. Manser, P. V. Kamat: *Band filling with free charge carriers in organometal halide perovskites*, Nat. Photonics **8**, 737 (2014)

[73] A. M. Askar, K. Shankar: *Exciton binding energy in organic-inorganic tri-halide perovskites*, J. Nanosci. Nanotechnol. **16**, 5890 (2016)

[74] J. Tilchin, D. N. Dirin, G. I. Maikov, A. Sashchiuk, M. V. Kovalenko, E. Lifshitz: *Hydrogen-like Wannier-Mott excitons in single crystal of methylammonium lead bromide perovskite*, ACS Nano **10**, 6363 (2016)

[75] K. Galkowski, A. Mitioglu, A. Miyata, P. Plochocka, O. Portugall, G.E. Eperon, J. T.-W. Wang, T. Stergiopoulos, S. D. Stranks, H. J. Snaith: *Determination of the exciton binding energy and effective masses for methylammonium and formamidinium lead tri-halide perovskite semiconductors*, Energy Environ. Sci. **9**, 962 (2016)

[76] N. Sestu, M. Cadelano, V. Sarritzu, F. Chen, D. Marongiu, R. Piras, M. Mainas, F. Quochi, M. Saba, A. Mura: *Absorption f-sum rule for the exciton binding energy in methylammonium lead halide perovskites*, J. Phys. Chem. Lett. **6**, 4566 (2015)

[77] K. Tanaka, T. Takahashi, T. Ban, T. Kondo, K. Uchida, N. Miura: *Comparative study on the excitons in lead-halide-based perovskite-type crystals* $CH_3NH_3PbBr_3$ $CH_3NH_3PbI_3$, Solid State Commun. **127**, 619 (2013)

[78] M. Saba, F. Quochi, A. Mura, G. Bongiovanni: *Excited state properties of hybrid perovskites*, Acc. Chem. Res **49**, 166 (2016)

[79] X. Li, Y. Wu, S. Zhang, B. Cai, Y. Gu, J. Song, H. Zeng: $CsPbX_3$ *quantum dots for lighting and displays: Room-temperature synthesis, photoluminescence superiorities, underlying origins and white light-emitting diodes*, Adv. Funct. Mater. **26**, 2435 (2016)

[80] D. Fröhlich, K. Heidrich, H. Künzel, G. Trendel, J. Treusch: *Cesium-trihalogenplumbates a new class of ionic semiconductors*, J. Lumin. **18**, 385 (1979)

[81] L. M. Herz: *Charge-carrier dynamics in organic-inorganic metal halide perovskites*, Annu. Rev. Phys. Chem. **67**, 65 (2016)

[82] D. B. Mitzi, C. A. Feild, W. T. A. Harrison, A. M. Guloy: *Conducting tin halides with a layered organic-based perovskite structure*, Nature **369**, 467 (1994)

[83] D. B. Mitzi, S. Wang, C. A. Feild, C. A. Chess, A. M. Guloy: *Conducting layered organic-inorganic halides containing <110>-oriented perovskite sheets*, Science **267**, 1473 (1995)

[84] B. Saparov, D. B. Mitzi: *Organic-inorganic perovskites: structural versatility for functions materials design*, Chem. Rev. **116**, 4558 (2016)

[85] D. G. Billing, A. Lemmerer: *Synthesis, characterization and phase transitions in the inorganic-organic layered perovskite-type hybrids [$(C_nH_{2n+1}NH_3)PbI_4$], n = 4, 5 and 6*, Acta Crys. B **63**, 735 (2007)

[86] D. G. Billing, A. Lemmerer: *Synthesis, characterization and phase transitions of the inorganic-organic layered perovskite-type hybrids [$(C_nH_{2n+1}NH_3)PbI_4$] (n = 12, 14, 16 and 18)*, New J. Chem. **32**, 1736 (2008)

[87] A. Lemmerer, D. G. Billing: *Synthesis, characterization and phase transitions of the inorganic-organic layered perovskite-type hybrids [$(C_nH_{2n+1}NH_3)PbI_4$], n = 7,8,9 and 10*, Dalton Trans. **41**, 1146 (2012)

[88] E. Mosconi, A. Amat, M. K. Nazeeruddin, M. Grätzel, F. De Angelis: *First-principles modeling of mixed halide organometal perovskites for photovoltaic applications*, J. Phys. Chem. C **117**, 13902 (2013)

[89] J. Even, L. Pedesseau, M.-A. Dupertuis, J.-M. Jancu, C. Katan: *Electronic model for self-assembled hybrid organic/perovskite semiconductors: reverse band edge electronic states ordering and spin-orbit coupling*, Phys. Rev. B **86**, 205301 (2012)

[90] S. Sourisseau, N. Louvain, W. Bi, N. Mercier, D. Rondeau, F. Boucher, J.-Y. Buzare, C. Legein: *Reduced band gap hybrid perovskites resulting from combined hydrogen and halogen bonding at the organic-inorganic interface*, Chem. Mater. **19**, 600 (2007)

[91] E. A. Muljarov, S. G. Tikhodeev, N. A. Gippius, T. Ishihara: *Excitons in self-organized semiconductor-insulator superlattices - PbI based perovskite compounds*, Phys. Rev. B **51**, 14370 (1995)

[92] A. Kojima, M. Ikegami, K. Teshima, T. Miyasaka: *Highly luminescent lead bromide perovskite nanoparticles synthesized with porous alumina media*, Chem. Lett. **41**, 397 (2012)

[93] S. Gonzalez-Carrero, R. E. Galian, J. Pérez-Prieto: *Maximizing the emissive properties of $CH_3NH_3PbBr_3$ perovskite nanoparticles*, J. Mater. Chem. A **3**, 9187 (2015)

[94] W. Zinth, U. Zinth: *Optik*, Oldenbourg, München (2013)

[95] https://www.nobelprize.org: *The nobel prize in physics 1901*, Fassung vom 08.06.2018, M. Östlund, E. Bourghardt, R. Oxelström, Nobel Media AB, Stockholm (08.06.2018)

[96] https://www.nobelprize.org: *The nobel prize in physics 1914*, Fassung vom 08.06.2018, M. Östlund, E. Bourghardt, R. Oxelström, Nobel Media AB, Stockholm (08.06.2018)

[97] C. F. Macrae, I. J. Bruno, J. A. Chisholm, P. R. Edgington, P. McCabe, E. Pidcock, L. Rodriguez-Monge, R. Taylor, J. van de Streek, P. A. Wood: *Mercury CSD 2.0 - new features for the visualization and investigation of crystal structures*, J. of Appl. Cryst. **41**, 466 (2008)

[98] W. H. Bragg, W. L. Bragg: *The reflection of X-rays by crystals*, Proc. R. Soc. Lond. A **88**, 428 (1913)

[99] J. Ilasvsky: *Nika: software for two-dimensional data reduction*, J. Appl. Cryst. **45**, 324 (2012)

[100] B. E. Warren: *X-ray diffraction*, Dover Publications, New York, 1st edition (1990)

[101] D. Weber: *Das Perowskitsystem $CH_3NH_3[Pb_nSn_{1-n}X_3]$ (X = Cl, Br, I)*, Z. Naturforsch., B: J. Chem. Sci. **34b**, 939 (1978)

[102] R. E. Wasylishen, O. Knop, J. B. Macdonald: *Cation rotation in methylammonium lead halides*, Solid State Commun. **56**, 581 (1985)

[103] O. Knop, R. E. Wasylishen, M. A. White, T. S. Cameron, M. J. M. Van Oort: *Alkylammonium lead halides. Part 2. $CH_3NH_3PbX_3$ (X = Cl, Br, I) perovskites: cuboctahedral halide cages with isotropic cation reorientation*, Can. J. Chem. **68**, 412 (1990)

[104] G. Hodes: *Perovskite-based solar cells*, Science **342**, 317 (2013)

[105] R. F. Service: *Turning up the light*, Science **342**, 794 (2013)

[106] E. Hanamura: *Rapid radiative decay and enhanced optical nonlinearity of excitons in a quantum well*, Phys. Rev. B **38**, 1228 (1988)

[107] S. Ithurria, M. D. Tessier, B. Mahler, R. P. S. M. Lobo, B. Dubertret, A. L. Efros: *Colloidal nanoplatelets with two-dimensional electronic structure*, Nat. Mater. **10**, 936 (2011)

[108] F. Zhang, H. Zhong, C. Chen, X-g. Wu, X. Hu, H. Huang, J. Han, B. Zou, Y. Dong: *Brightly luminescent and color-tunable colloidal $CH_3NH_3PbX_3$ (X = Br, I, Cl) quantum dots: potential alternatives for display technology*, ACS Nano **9**, 4533 (2015)

[109] F. Zhu, L. Men, Y. Guo, Q. Zhu, U. Bhattacharjee, P. M. Goodwin, J. W. Petrich, E. Smith, J. Vela: *Shape evolution and single particle luminescence of organometal halide perovskite nanocrystals*, ACS Nano **9**, 2948 (2015)

[110] L. Protesescu, S. Yakunin, M. I. Bodnarchuk, F. Krieg, R. Caputo, C. H. Hendon, R. X. Yang, A. Walsh, M. V. Kovalenko: *Nanocrystals of cesium lead halide perovskites ($CsPbX_3$, X=Cl, Br, and I): novel optoelectronic materials showing bright emission with wide color gamut*, Nano Lett. **15**, 3692 (2015)

[111] S. Gonzalez-Carrero, R. E. Galian, J. Pérez-Prieto: *Organometal halide perovskites: bulk low-dimension materials and nanoparticles*, Part. Part. Syst. Charact. **32**, 709 (2015)

[112] P. Tyagi, S. M. Arveson, W. A. Tisdale: *Colloidal organohalide perovskite nanoplatelets exhibiting quantum confinement*, J. Phys. Chem. Lett. **6**, 1911 (2015)

[113] E. Edri, S. Kirmayer, D. Cahen, G. Hodes: *High open-circuit voltage solar cells based on organic–inorganic lead bromide perovskite*, J. Phys. Chem. Lett. **4**, 897 (2013)

[114] Y. Tabuchi, K. Asai, M. Rikukawa, K. Sanui, K. J. Ishigure: *Preparation and characterization of natural lower dimensional layered perovskite-type compounds*, Phys. Chem. Solids **61**, 837 (2000)

[115] H. Mashiyama, Y. Kurihara, T. Azetsu: *Disordered cubic perovskite structure of $CH_3NH_3PbX_3$ (X= Cl, Br, I)*, J. Korean Phys. Soc. **32**, 156 (1998)

[116] M. I. Saidaminov, A. L. Abdelhady, B. Murali, E. Alarousu, V. M. Burlakov, W. Peng, I. Dursun, L. Wang, Y. He, G. Maculan, A. Goriely, T. Wu, O. F. Mohammed, O. M. Bakr: *High-quality bulk hybrid perovskite single crystals within minutes by inverse temperature crystallization*, Nat. Commun. **6**, 7586 (2015)

[117] G. A. Elbaz, D. B. Straus, O. E. Semonin, T. D. Hull, D. W. Paley, P. Kim, J. S. Owen, C. R. Kagan, X. Roy: *Unbalanced hole and electron diffusion in lead bromide perovskites*, Nano Lett. **17**, 1727 (2017)

[118] A. Poglitsch, D. Weber: *Dynamic disorder in methylammoniumtrihalogenoplumbates (II) observed by millimeter-wave spectroscopy*, J. Chem. Phys. **87**, 6373 (1987)

[119] J. Calabrese, N. L. Jones, R. L. Harlow, N. Herron, D. L. Thorn, Y. Wang: *Preparation and characterization of layered lead halide compounds*, J. Am. Chem. Soc. **113**, 2328 (1991)

[120] G. C. Papavassiliou, A. P. Patsis, D. J. Lagouvardos, I. B. Koutselas, *Spectroscopic studies of $(C_{10}H_{21}NH_3)_2PbI_4$,$(CH_3NH_3)(C_{10}H_{21}NH_3)_2Pb_2I_7$,$(CH_3NH_3)PbI_3$, and similar compounds*, Synth. Met. **57**, 3889, (1993)

[121] H. Mathieu, P. Lefebvre, P. Christol: *Simple analytical method for calculating exciton binding energies in semiconductor quantum wells*, Phys. Rev. B **46**, 4092 (1992)

[122] K. Tanaka, T. Kondo: *Bandgap and exciton binding energies in lead-iodide-based natural quantum-well crystals*, Sci. Technol. Adv. Mater. **4**, 599 (2003)

[123] P. Umari, E. Mosconi, F. De Angelis: *Relativistic GW calculations on $CH_3NH_3PbI_3$ and $CH_3NH_3SnI_3$ perovskites for solar cell applications*, Sci. Rep. **4**, 4464 (2014)

[124] B. J. Bohn, Y. Tong, M. Gramlich, M. Ling Lai, M. Döblinger, K. Wang, R. L. Z. Hoye, P. Müller-Buschbaum, S. D. Stranks, A. S. Urban, L. Polavarapu, J. Feldmann: *Boosting tunable blue luminescence of halide perovskite nanoplatelets through postsynthetic surface trap repair*, Nano Lett. **18**, 5231 (2018)

[125] J. Feldmann, G. Peter, E. O. Göbel, P. Dawson, K. Moore, C. Foxon, R. J. Elliott: *Linewidth dependence of radiative exciton lifetimes in quantum wells*, Phys. Rev. Lett. **59**, 2337 (1987)

[126] V. A. Hintermayr, A. F. Richter, F. Ehrat, M. Döblinger, W. Vanderlinden, J. A. Sichert, Y. Tong, L. Polavarapu, J. Feldmann, A. S. Urban: *Tuning the optical properties of perovskite nanoplatelets through composition and thickness by ligand-assisted exfoliation*, Adv. Mater. **28**, 9478 (2016)

[127] Y. Tong, F. Ehrat, W. Vanderlinden, C. Cardenas-Daw, J. K. Stolarczyk, L. Polavarapu, A. S. Urban: *Dilution-induced formation of hybrid perovskite nanoplatelets*, ACS Nano **10**, 10936 (2016)

[128] B. T. Diroll, H. Zhou, R. D. Schaller: *Low-temperature absorption, photoluminescence, and lifetime of $CsPbX_3$ (X = Cl, Br, I) nanocrystals*, Adv. Funct. Mater. **28**, 1800945 (2018)

[129] J. Mooney, P. Kambhampati: *Get the basics right: Jacobian conversion of wavelength and energy scales for quantitative analysis of emission spectra*, J. Phys. Chem. Lett. **4**, 3316 (2013)

[130] Y. Tong, E. Bladt, M. F. Aygüler, A. Manzi, K. Z. Milowska, V. A. Hintermayr, P. Docampo, S. Bals, A. S. Urban, L. Polavarapu, J. Feldmann: *Highly luminescent cesium lead halide perovskite nanocrystals with tunable composition and thickness by ultrasonication*, Angew. Chem. Int. Ed. **55**, 13887 (2016)

[131] F. Bertalotti, L Protesescu, M. V. Kovalenko, S. Yakunin, A. Cervellino, S. J. L. Billinge, M. W. Terban, J. S. Pedersen, N. Masciocchi, A. Guagliardi: *Coherent nanotwins and dynamic disorder in cesium lead halide perovskite nanocrystals*, ACS Nano **11**, 3819 (2017)

[132] M C. Brennan, M. Kuno, S. Rouvimov: *Crystal Structure of Individual $CsPbBr_3$ Perovskite Nanocubes*, Inorg. Chem. **58**, 1555 (2019)

[133] www.sigmaaldrich.com: *Oleylamine*, Fassung vom 28.09.2018, Merck KGaA, Darmstadt (28.09.2018)

[134] S. F. Wuister, A. van Houselt, C. de Mello Doneg, D. Vanmaekelbergh, A. Meijerin: *Temperature antiquenching of the luminescence from capped CdSe quantum dots*, Angew. Chem. Int. Ed. **43**, 3029 (2004)

[135] S. F. Wuister, C. de Mello Donega, A. Meijerink: *Luminescence temperature antiquenching of water-soluble CdTe quantum dots: role of the solvent*, J. Am. Chem. Soc. **126**, 10397 (2004)

[136] L. Chen, B. Li, C. Zhang, X. Huang, X. Wang, M. Xiao: *Composition-dependent energy splitting between bright and dark excitons in lead halide perovskite nanocrystals*, Nano Lett. **18**, 2074 (2018)

[137] L. Biadala, B. Siebers, Y. Beyazit, M. D. Tessier, D. Dupont, Z. Hens, D. R. Yakovlev, M. Bayer: *Band-edge exciton fine structure and recombination dynamics in InP/ZnS colloidal nanocrystals*, ACS nano **10**, 3356 (2016)

[138] J. Feldmann, G. Peter, E. O. Göbel: *Linewidth dependence of radiative exciton lifetimes in quantum wells*, PRL **59**, 20 (1987)

[139] D. S. Citrin: *Homogeneous-linewidth effects on radiative lifetimes of excitons in quantum wells*, Solid State Commun. **84**, 281 (1992)

[140] J. Lee, E. S. Koteles, M. O. Vassell: *Luminescence linewidths of excitons in GaAs quantum wells below 150 K*, Phys. Rev. B **33**, 5512 (1986)

[141] W. Stolz, J. C. Maan, M. Altarelli, L. Tapfer, K. Ploog: *Absorption spectroscopy on $Ga_{0.47}Im_{0.53}As/Al_{0.48}In_{0.52}As$ multi-quantum-well heterostructures. I. Excitonic transitions*, Phys. Rev. B **8**, 4301 (1987)

[142] M. A. Becker, R. Vaxenburg, G. Nedelcu, P. C. Serce, A. Shabaev, M. J. Mehl, J. G. Michopoulos, S. G. Lambrakos, N. Bernstein, J. L. Lyons, T. Stöferle, R. F. Mahrt, M. V. Kovalenko, D. J. Norris, G. Rainò1, A. L. Efros: *Bright triplet excitons in caesium lead halide perovskites*, Nature **553**, 289 (2018)

[143] C. W. Myung, S. Javaid, K. S. Kim, G. Lee: *Rashba-Dresselhaus effect in inorganic/organic lead iodide perovskite interfaces*, ACS Energy Lett. **3**, 1294 (2018)

[144] J. Ramada, L. M. Andriambariarijaona, V. Steinmetz, N. Goubet, L. Legrand, T. Barisien, F. Bernardot, C. Testelin, E. Lhuillier, A. Bramatib, M. Chamarroa: *Fine structure of excitons and electron–hole exchange energy in polymorphic $CsPbBr_3$ single nanocrystals*, Nanoscale **10**, 6393 (2018)

[145] J. Yin, P. Maity, L. Xu, A. M. El-Zohry, H. Li, O. M. Bakr, J.-L. Brédas, O. F. Mohammed: *Layer-dependent Rashba band splitting in 2D hybrid perovskites*, Chem. Mater. **30**, 8538 (2018)

[146] M. Grundmann, R. Heitz, D. Bimberg, J. H. H. Sandmann, J. Feldmann: *Carrier dynamics in quantum dots: modeling with master equations for the transitions between micro-states*, phys. stat. sol. (b) **203**, 121 (1997)

[147] T. Ishihara, J. Takahashi, T. Goto: *Optical properties due to electronic transitions in two-dimensional semiconductors $(C_nH_{2n+1}NH_3)PbI_4$*, Phys. Rev. B **42**, 11099 (1990)

[148] B. Traore, L. Pedesseau, L. Assam, X. Che, J.-C. Blancon, H. Tsai, W. Nie, C. C. Stoumpos, M. G. Kanatzidis, S. Tretiak, A. D. Mohite, J. Even, M. Kepenekian, C. Katan: *Composite nature of layered hybrid perovskites: assessment on quantum and dielectric confinements and band alignment*, ACS Nano **12**, 3321 (2018)

[149] K. Pradeesh, K. Nageswara Rao, G. Vijaya Prakash: *Synthesis, structural, thermal and optical studies of inorganic-organic hybrid semiconductors, R-PbI_4*, J. Appl. Phys. **113**, 083523 (2013)

[150] J. A. Sichert, Y. Tong, N. Mutz, M. Vollmer, S. Fischer, K. Z. Milowska, R. García Cortadella, B. Nickel, C. Cardenas-Daw, J. K. Stolarczyk, A. S. Urban, J. Feldmann: *Quantum size effect in organometal halide perovskite nanoplatelets*, Nano Lett. **15**, 6521 (2015)

[151] K. Pradeesh, J. J. Baumberg, G. Vijaya Prakash: *Exciton switching and Peierls transitions in hybrid inorganic-organic self-assembled quantum wells*, Appl. Phys. Lett. **95**, 173305 (2009)

[152] J. L. Knutson, J. D. Martin, D. B. Mitzi: *Tuning the band gap in hybrid tin iodide perovskite semiconductors using structural templating*, Inorg. Chem. **44**, 4699 (2005)

[153] K.-Z. Du, Q. Tu, X. Zhang, Q. Han, J. Liu, S. Zauscher, D. B. Mitzi: *Two-dimensional lead(II) halide-based hybrid perovskites templated by acene alkylamines: crystal structures, optical properties, and piezoelectricity*, Inorg. Chem. **56**, 9291 (2017)

[154] L. Mao, H. Tsai, W. Nie, L. Ma, J. Im, C. C. Stoumpos, C. D. Malliakas, F. Hao, M. R. Wasielewski, A. D. Mohite, M. G. Kanatzidis: *Role of organic counterion in lead- and tin-based two-dimensional semiconducting iodide perovskites and application in planar solar cells*, Chem. Mater. **28**, 7781 (2016)

[155] L. Dou, A. B. Wong, Y. Yu, M. Lai, N. Kornienko, S. W. Eaton, A. Fu, C. G. Bischak, J. Ma, T. Ding, N. S. Ginsberg, L.-W. Wang, A. P. Alivisatos, P. Yang: *Atomically thin two-dimensional organic-inorganic hybrid perovskites* Science **349**, 1518 (2015)

[156] M. Hirasawa, T. Ishihara, T. Goto, K. Uchida, N. Miura: *Magnetoabsorption of the lowest exciton in perovskite-type compound $CH_3NH_3PbI_3$*, Physica B **201**, 427 (1994)

[157] T. Ishihara: *Optical properties of PbI-based perovskite structures*, J. Lumin. **60**, 269 (1994)

[158] H. T. Grahn: *Semiconductor superlattices: growth and electronic properties*, World Scientific, Singapore, 1st edition (1995)

[159] R. Dingle, A. Gossard, W. Wiegmann: *Direct observation of superlattice formation in a semiconductor heterostructure*, Phys. Rev. Lett. **34**, 1327 (1975)

[160] T. Ando, A. B. Fowler, F. Stern: *Electronic properties of two-dimensional systems*, Rev. Mod. Phys. **54**, 437 (1982)

[161] D. Sapori, M. Kepenekian, L. Pedesseau, C. Katan, J. Even: *Quantum confinement and dielectric profiles of colloidal nanoplatelets of halide inorganic and hybrid organic–inorganic perovskites*, Nanoscale **8**, 6369 (2016)

[162] P. Yuh, K. L. Wang: *Formalism of the Kronig-Penney model for superlattices of variable basis*, Phys. Rev. B **38**, 18 (1988)

[163] J. Even, L. Pedesseau, C. Katan: *Understanding quantum confinement of charge carriers in layered 2D hybrid perovskites*, ChemPhysChem **15**, 3733 (2014)

[164] L. M. Herz: *Charge-carrier mobilities in metal halide perovskites: Fundamental mechanisms and limits*, ACS Energy Lett. **2**, 1539 (2017)

[165] R. Benchamekh: *Tight-binding calculations of image-charge effects in colloidal nanoscale platelets of CdSe*, Physical Review B **89**, 3 (2014)

[166] S. Ahmad, J. J. Baumberg, G. V. Prakash: *Structural tunability and switchable exciton emission in inorganic-organic hybrids with mixed halides*, J. Appl. Phys. **114**, 233511 (2013)

[167] M. He, Y. Cheng, R. Yuan, L. Zhou, J. Jiang, T. Xu, W. Chen, Z. Liu, W. Xiang, X. Liang: *Mn-Doped cesium lead halide perovskite nanocrystals with dual-color emission for WLED*, Dyes Pigm. **152**, 146 (2018)

[168] Z.-J. Li, E. Hofman, J. Li, A. H. Davis, C.-H. Tung, L.-Z. Wu, W. Zheng: *Photoelectrochemically active and environmentally stable CsPbBr3/TiO_2 Core/Shell nanocrystals*, Adv. Funct. Mater. **28**, 1704288 (2018)

[169] J. Song, J. Li, X. Li, L. Xu, Y. Dong, H. Zeng: *Quantum dot light-emitting diodes based on inorganic perovskite cesium lead halides ($CsPbX_3$)*, Adv. Mater. **27**, 7162 (2015)

[170] E.-P. Yao, Z. Yang, L. Meng, P. Sun, S. Dong, Y. Yang, Y. Yang: *High-brightness blue and white LEDs based on inorganic perovskite nanocrystals and their composites*, Adv. Mater. **29**, 1606859 (2017)

[171] S. Kumar, J. Jagielski, S. Yakunin, P. Rice, Y.-C. Chiu, M. Wang, G. Nedelcu, Y. Kim, S. Lin, E. J. G. Santos: *Efficient blue electroluminescence using quantum-confined two-dimensional perovskites*, ACS Nano **10**, 9720 (2016)

[172] H. Tsai, W. Nie, J.-C. Blancon, C. C. Stoumpos, R. Asadpour, B. Harutyunyan, A. J. Neukirch, R. Verduzco, J. J. Crochet, S. Tretiak, L. Pedesseau, J. Even, M. A. Alam, G. Gupta, J. Lou, P. M. Ajayan, M. J. Bedzyk, M. G. Kanatzidis, A. D. Mohite: *High-efficiency two-dimensional Ruddlesden-Popper perovskite solar cells*, Nature **536**, 312 (2016)

[173] A. Kane: *'Game-changing' perovskite solar tech could be cheaper and more efficient*, The Guardian, Guardian News & Media Ltd., London (2015)

[174] X. Wu, M. Tuan Trinh, D. Niesner, H. Zhu, Z. Norman, J. S. Owen, O. Yaffe, B. J. Kudisch, X.-Y. Zhu: *Trap states in lead iodide perovskites*, J. Am. Chem. Soc. **137**, 2089 (2015)

[175] B. J. Bohn, T. Simon, M. Gramlich, A. F. Richter, L. Polavarapu, A. S. Urban, J. Feldmann: *Dephasing and quantum beating of excitons in methylammonium lead iodide perovskite nanoplatelets*, ACS Photonics **5**, 648 (2018)

Acknowledgments

It was a great opportunity for me to conduct my research for this thesis at the Chair of Photonics and Optoelectronics of Prof. Dr. Jochen Feldmann at the Ludwig-Maximilians-Universität München. I enjoyed working in this international group and I have learned a lot. Many people were directly or indirectly involved in the work for this thesis and I would like to thank the people who supported me the most in completing my thesis.

First, I would like to express my thanks to my doctoral thesis supervisor Prof. Dr. Jochen Feldmann for the possibility to conduct my research at his chair. I have greatly benefited from highly productive discussions we had and the support he provided. I profited from the great and diverse scientific environment at his chair and I am thankful for the chance to conduct my research in the very well equipped laboratories of his chair. I am grateful for the opportunities to present my work at many different conferences and for the research visit at the Lawrence Berkeley National Laboratories.

Many thanks to my advisor Prof. Dr. Alexander Urban for very fruitful discussions. It has been great that he always had time whenever needed to discuss my research projects and helped me with manuscripts and conference contributions. Thanks for sharing your knowledge and the excellent support.

I am thankful to Dr. Carlos Cardenas-Daw for very helpful discussions. Thanks for sharing your knowledge, for all your help in the chemistry lab whenever needed, and the great support.

I want to thank Prof. Dr. Weber-Bargioni and his group that made my research visit at the Lawrence Berkeley National Laboratories very successful and pleasant. In this respect I am also grateful for financial support for my research visit in Berkeley provided by the Nano Initiative Munich.

Many thanks to PD Dr. Bert Nickel, Dr. Stefan Fischer, and Janina Roemer for XRD measurements and very fruitful discussions.

I would like to thank Prof. Dr. Thomas Bein and Prof. Dr. Joachim Rädler for providing the XRD, HRTEM, and TEM, as well as Dr. Markus Döblinger, Dr. Andreas Wisnet, and Meltem Aygüler for HRTEM and help with XRD measurements.

I am very grateful to Dr. Yu Tong and Dr. Lakshminarayana Polavarapu for sample preparation and excellent collaboration work.

Many thanks to Florian Ehrat for introducing me to the Streak setup, as well as to him and Alexander Richter for introducing me to the TCSPC setup. Thanks to Christoph Maier and Patrick Urban for help regarding IT-issues. In particular thanks to Alexander Richter, Aurora Manzi, Bernhard Bohn, Carola Lampe, Moritz Gramlich, and Stefanie Pritzl for helpful suggestions on this thesis.

I enjoyed working with the bachelor and master students Anna Weiß and Annick Hemmerling. I want to thank them both for their excellent work on our research projects.

Many thanks Gerlinde Adam for her support and her help regarding administrative work. Thanks to Stefan Niedermaier, Christian Holopirek, Katja Lyons, Martin Vogel, and Talee Barghouti for technical support in the laboratories.

My special thanks go to all my colleagues at the Chair of Photonics and Optoelectronics, there are too many to name all of them here. I appreciate the support, the fruitful discussions, and the great working atmosphere. In particular thanks to my office mates Dr. Anastasia Babynina, Christoph Maier, Dr. Miao Li, Dr. Yu Tong, Carola Lampe, Moritz Gramlich, Florian Ehrat, Dr. Carlos Cardenas-Daw, Dr. Jaekwon Do, Verena Baumann, Dr. Thomas Simon, Alexander Richter, and Ludwig Hüttenkofer, for the nice atmosphere in the third floor.

Finally, I want to thank my friends and family, especially Bernhard, Christina, Heinz, Tobias, Andreas, and Fabian for their friendship, their help and their support.